MHD STABILITY ANALYSES of a TOKAMAK PLASMA

by TIME-DEPENDENT CODES

(時間依存コードによるトカマク・プラズマのMHD安定性解析)

GEN-ICHI KURITA

ABSTRACT

The MHD properties of a tokamak plasma are investigated by using time evolutional codes. As for the ideal MHD modes we have analyzed the external modes including the positional instability. Linear and nonlinear ideal MHD codes have been developed. Effects of the toroidicity and conducting shell on the external kink mode are studied minutely by the linear code. A new rezoning algorithm is devised and it is successfully applied to express numerically the axisymmetric plasma perturbation in a cylindrical geometry. As for the resistive MHD modes we have developed nonlinear codes on the basis of the reduced set of the resistive MHD equations. By using the codes we have studied the major disruption processes and properties of the low n resistive modes. We have found that the effects of toroidicity and finite poloidal beta are very important. Considering the above conclusion we propose a new scenario of the initiation of the major disruption.

CONTENTS

Chapter I

Introduction

The tokamak is considered as the most promising magnetic fusion device for achieving controlled nuclear fusion. If successful, the present generation large tokamaks are situated very close to the milestone of attaining the ignition plasma condition. There are, however, various kinds of problems to be solved before achieving the plasma condition for an economical tokamak fusion reactor. Even if we restrict ourselves only to the theoretical researches of a reactor plasma, there are many problems concerning: (1) determination of a limiting beta value, (2) analyses of disruptive instabilities, (3) transport processes and scaling laws of the plasma confinement, (4) methods to reduce impurities, (5) new efficient heating methods, (6) methods to sustain a plasma current continuously, (7) problems in a DT burning plasma and so on. Among them, the items (1), (2), and (3) are the problems concerning the most basic confinement property of the tokamak plasma. Though these have been studied by many authors since the biginning of the nuclear fusion research, sufficiently clear solutions to the problems have not been obtained yet. Especially, the first and second probelms are closely related to the necessary external magnetic field strength in the device and determined of technological safety factor of the fusion reactor, respectively, and the solutions to them give an important information directly concerning the economical feasibility of the tokamak fusion reactor. Therefore, these problems should be most urgently solved in the field of the tokamak research.

As for the preceding works on the problems, theoretical studies of the fusion plasma on the basis of the MHD model have been intensively carried out since the initial stage of the nuclear fusion research in 1950's. And by the recent successful results of the tokamak plasma confinement the significance and necessity of the theoretical MHD analyses become clearer and many authors are engaged in the solution of these problems. This is due to the fact that the tokamak plasma is confined for sufficiently long duration and the MHD equilibrium is virtually established in the tokamak. Brief summary of the preceding work is given in each corresponding Chapter.

Investigations described in this paper have been carried out as a part of the project TRITON[1,2] which aims at solving, mainly, the above two problems comprehensively from the various viewpoints. These two problems are rewritten in more concrete manner as

(1) To obtain theoretically a stable equilibrium within a framework of the ideal MHD model, and to determine the stability condition, controlling methods and limiting beta value.
(2) To clarify the mechanism of the disruptive instabilities in the tokamak within a framework of the resistive MHD model, and to obtain informations on the stability conditions and controlling methods.

Here, we assume that the most basic parts of the informations could be obtained by the analyses based on the MHD model.

The purpose of the investigations in this paper is to obtain some of the above informations by solving numerically the time dependent MHD equations and simulating phenomena which relate the above problems. Especially, the following two points are the main concerns of this paper,

(1) Analyses of the external modes of the ideal MHD instabilities including the positional instability.
(2) Studies of theoretical models of the disruptive instabilities of the tokamak.

The former is dangerous in the current rising stage of a tokamak plasma, and the latter is considered to limit the plasma current and is unfavorable to economic operation of a tokamak reactor. Since enormous computations on a parameter survey are necessary to establish the scaling law of the limiting beta value MHD spectral codes such as ERATO[3~6] and PEST[7~10] are more favorable for this purpose. The spectral codes give the stationary eigenvalues and the eigenmodes, and usually only the most unstable mode is calculated. The higher eigenmodes are sometimes difficult to obtain because of the large size of matrices. The effect of these higher modes on the plasma confinement is very important when they are less localized than the most unstable mode. The time evolutional solution, however, includes all components of the spectra and we can see the behaviour of the higher modes as well

as most unstable one. In addition, the time evolutional code based on the linear ideal MHD theory is directly extended to the nonlinear resistive code. In this paper, we make only brief mention of the analyses by the spectral code for the purpose of comparison of the results between the time evolutional and spectral methods.

In Chapter II, we describe the time evolutional code based on the linear ideal MHD equations where we make the check of accuracy of the code by comparing the results with those by the spectral code and analytical ones, and we clarify the effects of the toroidicity and conducting shell. Chapter III is related to the nonlinear ideal MHD model. In order to develop a nonlinear positional stability code on the basis of the above model, we devise a new algorithm for the rezoning of the two dimensional meshes and we confirm that the code works well and the new algorithm is useful in this kind of analyses. Chapter IV and V are devoted to the problems concerning the disruptive instabilities. In Chapter IV, we develop a nonlinear MHD code based on the reduced set of resistive MHD equations and simulate an example of the major disruption[11~14]. We have traced the major disruption scenario proposed by the ORNL group and successfully reproduced the disruption. However, we have shown it improbable that the major disruption is initiated by the flattening of the current profile due to the internal disruption. In Chapter V, we mention the significance of the effect of toroidicity and finite poloidal beta to understand the resistive instabilities. In relation to it we propose a new scenario on the major disruption. Conclusions and discussion of the paper are presented in Chapter VI.

References

1) M. Azumi, G. Kurita, T. Matsuura, T. Takeda, Y. Tanaka and T. Tsunematsu, in Computing Method in Applied Science and Engineering, (Proc. 4th Int. Symp. Versailles, 1979) North-Holland (1980) P.335.
2) T. Tsunematsu, T. Takeda, T. Matsuura, G. Kurita and M. Azumi, Comput. Phys. Commun. 19, (1980) 179.
3) R. Gruber, F. Troyon, D. Berger, L.C. Bernard, S. Rousset, R. Schreiber, W. Kerner, W. Schneider and K.V. Roberts, Comput. Phys. Commun. 21, (1981) 323.
4) L.A. Charlton, R.A. Dory, Y.-K.M. Peng, D.J. Stricker, S.J. Lynch, D.K. Lee, R. Gruber and F. Troyon, Phys. Rev. Lett. 19, (1979) 1395.
5) W. Kerner, R. Gruber and F. Troyon, Phys. Rev. Lett. 25, (1980) 536.
6) T. Tsunematsu, T. Takeda, G. Kurita, M. Azumi, T. Matsuura, R. Gruber and F. Troyon, "Beta-Limit of Large Tokamak with a Circular Cross-Section", Japan Atomic Energy Research Institute Report JAERI-M 9890 (1982).
7) R.C. Grimm, J.M. Greene and J.L. Johnson, Methods in Computational Physics, (Academic Press, New York, 1976) Vol.16 P.253.
8) R.L. Dewar, R.C. Grimm, J.L. Johnson, E.A. Frieman, J.M. Greene and P.H. Rutherford, Phys. Fluids 17, (1974) 930.
9) A.M.M. Todd, J. Manickam, M. Okabayashi, M.S. Chance, R.C. Grimm, J.M. Greene and J.L. Johnson, Nucl. Fusion 19, (1979) 743.
10) A.M.M. Todd, M.S. Chance, J.M. Greene, R.C. Grimm, J.L. Johnson and J. Manickam, Phys. Rev. Lett. 11, (1977) 826.
11) B.V. Waddell, B. Carreras, H.R. Hicks, J.A. Holmes and D.K. Lee, Phys. Rev. Lett. 41, (1978) 1368.
12) B.V. Waddell, B. Carreras, H.R. Hicks and J.A. Holmes, Phys. Fluids 22, (1979) 896.
13) B. Carreras, H.R. Hicks, J.A. Holmes and B.V. Waddell, Phys. Fluids 23, (1980) 1181.
14) B. Carreras, H.R. Hicks and D.K. Lee, Phys. Fluids 24, (1981) 66.

Chapter II

Linear Stability Analysis of Toroidal Plasma

In order to study the linearized ideal MHD instabilities of a toroidal plasma a time evolutional code ZEPHYrus is developed and the code is checked by calculating the instability growth rate for model equilibria.

The effects of toroidicity and conducting shell on the free boundary kink mode are investigated by using the code ZEPHYrus . The results are as follows. When a conducting shell is far away from the plasma surface, the growth rate of the external kink mode can be decreased only in tokamaks with small aspect ratio, $A < 10$. On the other hand, when the shell is close to the plasma surface, the unstable external modes are stabilized by the effects of toroidicity and conducting shell.

2.1 Introduction

For interpretation of experimental data and design of future large fusion devices it is very important to analyze the linear MHD stability in detail. Because of complexities of the physics processes in actual fusion devices extensive computational studies are required for the above purpose. In order to analyze the linear MHD stability two methods are usually taken, i.e., the matrix method and computer simulation. The former method is based on the variational principle[1]. The Lagrangian of the system is first, represented as a quadratic form of the plasma displacements by using the finite element method and, then, it is extremized with respect to the displacement[2]. By the procedure the usual matrix eigenvalue problem is derived. The latter method is composed of solution of an initial-value problem of a time-dependent MHD equations. General MHD spectral codes applicable to an axisymmetric toroidal plasma are successfully developed by Lausanne (ERATO code)[3] and Princeton (PEST code)[4] groups on the basis of the above variational approach. Various kinds of linear stability analyses by using the ERATO and PEST codes are reported[5~7]. As for the time dependent solution of the linearized MHD system several works[8~10] are reported in the initial stage of the computational studies of the fusion plasma, but recently most efforts concerning solution of the initial value problems are directed to analyses of nonlinear behavior of a resistive plasma as will be described in chapters 4 and 5.

The above two methods are equivalent in principle but technical details make them rather different each other. The results of both the methods should be subject to critical comparison but it has not been carried out sufficiently. In this Chapter we develop a new initial-value code ZEPHYrus and make comparison between the results by the spectral code and initial value code. After that we investigate the effects of the shell and toroidicity on the linear MHD stability.

In Section 2.2 the equilibrium equation for an axisymmetric toroidal plasma is expanded in powers of the inverse aspect ratio and analytical representation of the equilibrium solution is obtained. The basic equations for the linear ideal MHD stability and boundary conditions are given in Sections 2.3 and 2.4, respectively. Section 2.5 describes the numerical procedures adopted for the analyses. Results of the calculations given in Sections 2.6 to 2.8. Comparisons of the results with the analytical and numerical ones are presented in Section 2.6. Effects of toroidicity and conducting shell are investigated in Sections 2.7 and 2.8 for the internal and external modes. Section 2.9 is devoted for conclusions and discussion.

2.2 Equilibrium

In this Section, equilibrium solutions for a tokamak plasma subject to stability analyses in the following Sections are given.
The MHD equilibrium equations are

$$\begin{aligned} \vec{\nabla} P_0 &= \vec{j}_0 \times \vec{B}_0 \quad , \\ \vec{j}_0 &= \vec{\nabla} \times \vec{B}_0 \quad . \end{aligned} \tag{2.1}$$

First, we define a curvilinear coordinate system (r,θ,ϕ) as shown in Fig. 2.1, where surfaces of constant r correspond to magnetic surfaces.[11,12] The transformation from the (r,θ,ϕ) coordinate system to the cylindrical (X,Φ,Z) system is written formally as

$$\begin{aligned} X &= X(r,\theta) \quad , \\ Z &= Z(r,\theta) \quad , \\ \Phi &= \phi \quad . \end{aligned} \tag{2.2}$$

The metric tensor of (r,θ,ϕ) system is defined as follows;

$$g_{rr} = \left(\frac{\partial X}{\partial r}\right)^2 + \left(\frac{\partial Z}{\partial r}\right)^2 \quad ,$$

$$g_{r\theta} = \frac{\partial X}{\partial r}\frac{\partial X}{\partial \theta} + \frac{\partial Z}{\partial r}\frac{\partial Z}{\partial \theta} \quad ,$$

$$g_{\theta\theta} = \left(\frac{\partial X}{\partial \theta}\right)^2 + \left(\frac{\partial Z}{\partial \theta}\right)^2 \quad ,$$

$$g_{\phi\phi} = X^2 \quad ,$$

$$\sqrt{g} = X\left(\frac{\partial X}{\partial \theta}\frac{\partial Z}{\partial r} - \frac{\partial X}{\partial r}\frac{\partial Z}{\partial \theta}\right) \quad , \tag{2.3}$$

$$g^{rr} = \frac{g_{\theta\theta}g_{\phi\phi}}{g} \quad ,$$

$$g^{r\theta} = -\frac{g_{r\theta}g_{\phi\phi}}{g} \quad ,$$

$$g^{\theta\theta} = \frac{g_{rr}\,g_{\phi\phi}}{g} \quad ,$$

$$g^{\phi\phi} = \frac{1}{X^2} \quad .$$

In this coordinate system the equilibrium magnetic field is expressed as,

$$\vec{B}_0 = R_0B_0\left(f(r)\vec{\nabla}\phi \times \vec{\nabla}r + h(r)\vec{\nabla}\phi\right) \quad , \tag{2.4}$$

where B_0 is constant magnetic field magnitude introduced to make $f(r)$ and $h(r)$ dimensionless. The first term of Eq.(2.4) represents the poloidal magnetic field and the second is the toroidal field.

Then, the equilibrium equation (2.1) can be written in (r,θ,ϕ) system as follows,

$$\frac{P_0'(r)}{R_0B_0^2} + \frac{h(r)h'(r)}{g_{\phi\phi}} + \frac{f(r)}{\sqrt{g}}\left\{\left(\frac{f(r)}{\sqrt{g}}\,g_{\theta\theta}\right)' - \frac{\partial}{\partial\theta}\left(\frac{f(r)}{\sqrt{g}}\,g_{r\theta}\right)\right\} = 0, \tag{2.5}$$

where prime denotes derivative with respect to r. For given distributions of pressure $P_0(r)$ and poloidal magnetic field R_0B_0f, an equilibrium solution (h,X,Z) is obtained by solving Eq. (2.5). In the following we consider a toroidal plasma with a large aspect ratio A ($=R_0/a \gg 1$; R_0 and a are the major and minor radii, respectively), and solve the equilibrium equation by expanding it with respect to the inverse aspect ratio.

The function forms of $X(r,\theta)$ and $Z(r,\theta)$ in Eqs.(2.2) are assumed as;

$$X(r,\theta) = R_0 - \varepsilon r\cos\theta - \varepsilon^2\Delta(r) + \varepsilon^3 E(r)\cos\theta \quad ,$$

$$Z(r,\theta) = \varepsilon r\sin\theta + \varepsilon^3 E(r)\sin\theta \quad , \tag{2.6}$$

where ε indicates the order of magnitude of the term is $\sim r/R_0$ and $\Delta(r)$ is the displacement of the magnetic surface from the magnetic axis, and $E(r)$ represents elliptic deformation of magnetic surface from a circle. Substituting Eq.(2.6) into Eq.(2.5), the following equations are obtained,

$$P_0' + hh' + \frac{f}{r}(rf)' = \frac{P_0'}{R_0}(2\Delta + 3r\Delta' - \frac{r^2}{2R_0}) + \frac{3f(rf)'}{2r}\Delta'^2 - f^2(\frac{\Delta'^2}{r} + \frac{\Delta}{R_0} + \frac{r}{2R_0^2}) \quad ,$$

$$\Delta'' + \{\frac{2(rf)'}{rf} - \frac{1}{r}\}\Delta' + \frac{2rP_0'}{R_0 f^2} - \frac{1}{R_0} = 0 \quad , \tag{2.7}$$

$$E'' + \{\frac{2(rf)'}{rf} - \frac{1}{r}\}E' - \frac{3}{r^2}E = -\frac{r^2P_0'}{2R_0^2f^2} + \frac{3}{2}\frac{(rf)'}{rf}\Delta'^2 - \frac{r}{2R_0^2} - \frac{\Delta'}{R_0} + \frac{3rP_0'}{R_0 f^2}\Delta' \quad .$$

We solve the above equation for a constant current density and parabolic pressure distribution in the plasma region, that is,

$$f(r) = rf_a \quad ,$$

$$P_0(r) = f_a^2\,\beta_p(1-r^2) \quad , \tag{2.8}$$

where $f_a = f(a)$ and β_p is poloidal beta. From Eqs.(2.7), we obtain

$$\Delta(r) = \frac{(1+4\beta_p)r^2}{8R_0} \quad ,$$

$$E(r) = E_a r - \frac{(3+16\beta_p^2)r(r^2-1)}{64\,R_0^2} \quad , \tag{2.9}$$

$$h(r) = \sqrt{1-2f_a^2(1-\beta_p)(r^2-1) - \frac{f_a^2(48\beta_p^2+1)(\beta_p+5)}{16\,R_0^2}(r^4-1)} \quad ,$$

where E_a is elliptic deformation at the plasma surface (r=a).

2.3 Basic Equations

In this Section, the basic equations for the ideal MHD stability are described and rewritten in the form convenient to the numerical calculation. We adopt the linearized ideal MHD equations of the following form,

$$\rho_0 \frac{\partial^2 \vec{\xi}}{\partial t^2} = -\vec{\nabla}P + \vec{j}_0 \times \vec{Q} + \vec{j} \times \vec{B}_0 \quad ,$$

$$\vec{j} = \vec{\nabla} \times \vec{Q} \quad , \tag{2.10}$$

$$\vec{Q} = \vec{\nabla} \times (\vec{\xi} \times \vec{B}_0) \quad ,$$

$$P = -\gamma P_0 \vec{\nabla}\cdot\vec{\xi} - (\vec{\xi}\cdot\vec{\nabla})P_0 \quad ,$$

where the quantities with subscript 0 are the equilibrium ones, γ is the specific heat ratio, and $\vec{j}$, $\vec{Q}$ and P are perturbed current density, magnetic field magnitude and plasma pressure, respectively.

For the sake of convenience of calculation the usual current densities multiplied by Jacobian are used as new current densities as

$$\sqrt{g}j \rightarrow j \quad . \tag{2.11}$$

For the same reason, we introduce new variables for components of the equilibrium and perturbed vectors and metric tensor as follows,

$$\tilde{j}_0^{\theta} = \frac{j_0^{\theta}}{R_0}, \quad \tilde{j}_0^{\phi} = \frac{j_0^{\phi}}{r}, \quad \tilde{B}_0^{\theta} = rB_0^{\theta}, \quad \tilde{B}_0^{\phi} = R_0 B_0^{\phi} \quad ,$$

$$\tilde{\xi}^{\theta} = r\xi^{\theta}, \quad \tilde{\xi}^{\phi} = R_0\xi^{\phi}, \quad \tilde{\xi}_{\theta} = \frac{\xi_{\theta}}{r}, \quad \tilde{\xi}_{\phi} = \frac{\xi_{\phi}}{R_0} \quad ,$$

$$\tilde{Q}^{\theta} = rQ^{\theta}, \quad \tilde{Q}^{\phi} = R_0 Q^{\phi}, \quad \tilde{Q}_{\theta} = \frac{Q_{\theta}}{r}, \quad \tilde{Q}_{\phi} = \frac{Q_{\phi}}{R_0} \quad , \tag{2.12}$$

$$\tilde{j}^{r} = \frac{j^{r}}{rR_0}, \quad \tilde{j}^{\theta} = \frac{j^{\theta}}{R_0}, \quad \tilde{j}^{\phi} = \frac{j^{\phi}}{r},$$

$$\tilde{\sqrt{g}} = \frac{\sqrt{g}}{rR_0}, \quad \tilde{g}_{r\theta} = \frac{g_{r\theta}}{r}, \quad \tilde{g}_{\theta\theta} = \frac{g_{\theta\theta}}{r^2}, \quad \tilde{g}_{\phi\phi} = \frac{g_{\phi\phi}}{R_0^2} \quad ,$$

where the quantities with superscript and subscript, r, θ and ϕ, mean the contravarient and covarient components of the vectors, respectively, and R_0 is the radius of the magnetic axis.

By the transformations shown in Eqs.(2.12), the magnitude of all metric tensor components of order ε^0, where ε is the inverse aspect ratio, becomes order one, and the MHD stability calculations in toroidal geometry by the expansion of the inverse aspect ratio can be done consistently. The symbol ~ for the new variables is dropped again in the following. Since each perturbed quantity has different phase in the ϕ direction, they must be divided into even and odd parts with respect to θ and are expressed as,

$$\begin{aligned} a(r,\theta,\phi) &= a^o(r,\theta)\cos(n\phi) - a^e(r,\theta)\sin(n\phi) \quad , \\ b(r,\theta,\phi) &= b^e(r,\theta)\cos(n\phi) + b^o(r,\theta)\sin(n\phi) \quad , \end{aligned} \tag{2.13}$$

where a is representation of $\xi^r, Q^\theta, Q^\phi, J^\theta, J^\phi$ and p and b is that of the other variables, n is the mode number in the ϕ direction and superscripts e and o denote even and odd functions with respect to θ, respectively. After the transformations shown in Eqs.(2.11) and (2.12), we substitute Eqs.(2.13) into Eqs.(2.10) and obtain the system of equations for each vector component in the following form,

$$\rho_0 \frac{\partial^2 \xi_r^o}{\partial t^2} = - \frac{\partial P^o}{\partial r} + (j^{\theta o} B^\phi - j^{\phi o} B^\theta) + (j_0^\theta Q^{\phi o} - j_0^\phi Q^{\theta o}) \quad ,$$

$$\rho_0 \frac{\partial^2 \xi_r^e}{\partial t^2} = - \frac{\partial P^e}{\partial r} + (j^{\theta e} B^\phi - j^{\phi e} B^\theta) + (j_0^\theta Q^{\phi e} - j_0^\phi Q^{\theta e}) \quad ,$$

$$\rho_0 \frac{\partial^2 \xi_\theta^e}{\partial t^2} = - \frac{1}{r} \frac{\partial P^o}{\partial \theta} + j_0^\phi Q^{re} - j^{re} B^\phi \quad ,$$

$$\rho_0 \frac{\partial^2 \xi_\theta^o}{\partial t^2} = \frac{1}{r} \frac{\partial P^e}{\partial \theta} + j_0^\phi Q^{ro} - j^{ro} B^\phi \quad ,$$

$$\rho_0 \frac{\partial^2 \xi_\phi^e}{\partial t^2} = k_z P^e + j^{re} B^\theta - j_0^\theta Q^{re} \quad ,$$

$$\rho_0 \frac{\partial^2 \xi_\phi^o}{\partial t^2} = k_z P^o + j^{ro} B^\theta - j_0^\theta Q^{ro} \quad ,$$

$$Q^{re} = \frac{B^\theta}{r} \frac{\partial \xi^{ro}}{\partial \theta} - k_z B^\phi \xi^{re} \quad , \quad Q^{ro} = - \frac{B^\theta}{r} \frac{\partial \xi^{re}}{\partial \theta} - k_z B^\phi \xi^{ro} \quad ,$$

$$Q^{\theta o} = k_z (B^\phi \xi^{\theta o} - B^\theta \xi^{\phi o}) - \frac{1}{\sqrt{g}} \frac{\partial}{\partial r} (\sqrt{g} B^\vartheta \xi^{ro}) \quad ,$$

$$Q^{\theta e} = k_z(B^{\phi}\xi^{\theta e} - B^{\theta}\xi^{\phi e}) - \frac{1}{\sqrt{g}}\frac{\partial}{\partial r}(\sqrt{g}B^{\theta}\xi^{re}) \quad , \tag{2.14}$$

$$Q^{\phi o} = \frac{B^{\theta}}{r}\frac{\partial \xi^{\phi e}}{\partial \theta} - \frac{1}{r\sqrt{g}}\{\frac{\partial}{\partial r}(\sqrt{g}B^{\phi}r\xi^{ro}) + \frac{\partial}{\partial \theta}(\sqrt{g}B^{\phi}\xi^{\theta e})\} \quad ,$$

$$Q^{\phi e} = -\frac{B^{\theta}}{r}\frac{\partial \xi^{\phi o}}{\partial \theta} - \frac{1}{r\sqrt{g}}\{\frac{\partial}{\partial r}(\sqrt{g}B^{\phi}r\xi^{re}) - \frac{\partial}{\partial \theta}(\sqrt{g}B^{\phi}\xi^{\theta o})\} \quad ,$$

$$j^{re} = \frac{1}{r}\frac{\partial Q_{\phi}^{o}}{\partial \theta} + k_z Q_{\theta}^{e}, \quad j^{ro} = -\frac{1}{r}\frac{\partial Q_{\phi}^{e}}{\partial \theta} + k_z Q_{\theta}^{o} \quad ,$$

$$j^{\theta o} = k_z Q_r^{o} - \frac{\partial Q_{\phi}^{o}}{\partial r} \quad , \quad j^{\theta e} = k_z Q_r^{e} - \frac{\partial Q_{\phi}^{e}}{\partial r} \quad ,$$

$$j^{\phi o} = \frac{1}{r}\{\frac{\partial}{\partial r}(rQ_{\theta}^{o}) - \frac{\partial Q_r^{e}}{\partial \theta}\} \quad , \quad j^{\phi e} = \frac{1}{r}\{\frac{\partial}{\partial r}(rQ_{\theta}^{e}) + \frac{\partial Q_r^{o}}{\partial \theta}\} \quad ,$$

$$P^{o} = -\xi^{ro}\frac{\partial P_0}{\partial r} - \frac{\gamma P_0}{r\sqrt{g}}\{\frac{\partial}{\partial r}(\sqrt{g}\,r\,\xi^{ro}) + \frac{\partial}{\partial \theta}(\sqrt{g}\xi^{\theta e})\} - \gamma P_0 k_z \xi^{\phi o} \quad ,$$

$$P^{e} = -\xi^{re}\frac{\partial P_0}{\partial r} - \frac{\gamma P_0}{r\sqrt{g}}\{\frac{\partial}{\partial r}(\sqrt{g}\,r\,\xi^{re}) - \frac{\partial}{\partial \theta}(\sqrt{g}\xi^{\theta o})\} - \gamma P_0 k_z \xi^{\phi e} \quad ,$$

where k_z denotes n/R_0 and the covarient components of vectors are related to contravarient components through the metric tensor shown in Eqs.(2.3).

2.4 Boundary Conditions

In this Section, we consider the boundary conditions to Eqs.(2.14) for internal and external kink modes. In order to impose same boundary conditions at the magnetic axis (r=0) to the m=1 (m is mode number in the θ direction) and other modes, we transform ξ^r and Q^r as follows;

$$r\xi^r \longrightarrow \xi^r \quad ,$$
$$rQ^r \longrightarrow Q^r \quad . \tag{2.15}$$

Then the boundary conditions at r=0 become

$$\xi^r = 0 \quad ,$$
$$Q^r = 0 \quad , \tag{2.16}$$

for both the modes.

In the case of the internal mode analysis we should solve a fixed boundary problem and the boundary condition at the plasma surface is represented by the same condition as Eq.(2.16).

On the other hand, the analysis of the external kink mode is a free boundary problem, and in this case we should calculate the perturbed magnetic field in the vacuum region in order to continue the solution at the plasma surface. For the purpose of the stability analyses in this Chapter, we obtain the magnetic field analytically in the torodial coordinate system (μ,η,ϕ) using the toroidal ring function (Fig.2.2).

The toroidal coordinates (μ,η,ϕ) are related to the cylindrical coordinates (X,Φ,Z) through the following relations,

$$\mu = \frac{1}{2}\,\ell n\,\frac{(X+R)^2+Z^2}{(X-R)^2+Z^2} \quad ,$$

$$\eta = \tan^{-1}\frac{2RZ}{X^2+Z^2-R^2} \quad . \tag{2.17}$$

The metric coefficients are written as

$$g_\mu = g_\eta = \frac{R}{\cosh\mu - \cos\eta} \quad ,$$

$$g_\phi = \frac{R\sinh\mu}{\cosh\mu - \cos\eta} \quad . \tag{2.18}$$

The general solution Ψ_e of the Laplace's equation in the toroidal coordinate system can be written as follows;

$$\Psi_e = \sqrt{x-\cos\eta}\sum_{k,n}\,[\{A_k P^n_{k-1/2}(x) + B_k Q^n_{k-1/2}(x)\}\cos(k\eta)\cos(n\phi)$$

$$+ \{C_k P^n_{k-1/2}(x) + D_k Q^n_{k-1/2}(x)\}\sin(k\eta)\sin(n\phi)] \quad , \tag{2.19}$$

where $x=\cosh\mu$, $P^n_{k-1/2}(x)$ and $Q^n_{k-1/2}(x)$ are the toroidal ring functions and the terms of $\cos(k\eta)\sin(n\phi)$ and $\sin(k\eta)\cos(n\phi)$ are omitted by considering the form of the internal solutions (2.13). Since $\vec{Q}_{ex} = \vec{\nabla}\Psi_e$, the perturbed magnetic field in the vacuum region can be written as follows;

$$Q_\mu = \sum_{k,n}\,[(XA\cdot A_k + XB\cdot B_k)\cos(n\phi) + (XC\cdot C_k + XD\cdot D_k)\sin(n\phi)] \quad ,$$

$$Q_\eta = \sum_{k,n}\,[(YA\cdot A_k + YB\cdot B_k)\cos(n\phi) + (YC\cdot C_k + YD\cdot D_k)\sin(n\phi)] \quad , \tag{2.20}$$

$$Q_\phi = \sum_{k,n} [(ZC\cdot C_k + ZD\cdot D_k)\cos(n\phi) + (ZA\cdot A_k + ZB\cdot B_k)\sin(n\phi)] \quad .$$

Here A_k, B_k, C_k, and D_k are constants to be determined from the boundary condition and XA, XB, XC, XD, etc. are defined as

$$XA = \frac{\sinh\mu}{g_\mu\sqrt{y}}\left\{\frac{P^n_{k-1/2}(x)}{2} + yP^{n'}_{k-1/2}(x)\right\}\cos(k\eta) \quad ,$$

$$XB = \frac{\sinh\mu}{g_\mu\sqrt{y}}\left\{\frac{Q^n_{k-1/2}(x)}{2} + yQ^{n'}_{k-1/2}(x)\right\}\cos(k\eta) \quad ,$$

$$XC = \frac{\sinh\mu}{g_\mu\sqrt{y}}\left\{\frac{P^n_{k-1/2}(x)}{2} + yP^{n'}_{k-1/2}(x)\right\}\sin(k\eta) \quad ,$$

$$XD = \frac{\sinh\mu}{g_\mu\sqrt{y}}\left\{\frac{Q^n_{k-1/2}(x)}{2} + yQ^{n'}_{k-1/2}(x)\right\}\sin(k\eta) \quad , \qquad (2.21)$$

$$YA = \frac{P^n_{k-1/2}(x)}{g_\eta\sqrt{y}}\left\{\frac{\sin\eta\cos(k\eta)}{2} - ky\sin(k\eta)\right\} \quad ,$$

$$YB = \frac{Q^n_{k-1/2}(x)}{g_\eta\sqrt{y}}\left\{\frac{\sin\eta\cos(k\eta)}{2} - ky\sin(k\eta)\right\} \quad ,$$

$$YC = \frac{P^n_{k-1/2}(x)}{g_\eta\sqrt{y}}\left\{\frac{\sin\eta\sin(k\eta)}{2} + ky\cos(k\eta)\right\} \quad ,$$

$$YD = \frac{Q^n_{k-1/2}(x)}{g_\eta\sqrt{y}}\left\{\frac{\sin\eta\sin(k\eta)}{2} + ky\cos(k\eta)\right\} \quad ,$$

$$ZA = -\frac{R_0^2 k_z\sqrt{y}}{g_\phi^2} P^n_{k-1/2}(x)\cos(k\eta) \quad , \quad ZB = -\frac{R_0^2 k_z\sqrt{y}}{g_\phi^2} Q^n_{k-1/2}(x)\cos(k\eta) \quad ,$$

$$ZC = \frac{R_0^2 k_z\sqrt{y}}{g_\phi^2} P^n_{k-1/2}(x)\sin(k\eta) \quad , \quad ZD = \frac{R_0^2 k_z\sqrt{y}}{g_\phi^2} Q^n_{k-1/2}(x)\sin(k\eta) \quad ,$$

where $x=\cosh\mu$, $y = x - \cos\eta$ and the prime denotes the derivative with respect to x.

Using the perturbed magnetic field obtained above, the boundary conditions for the free boundary problem are expressed as follows;

A) The normal component of the magnetic field vanishes at the perfectly conducting shell (r=b), that is

$$\vec{Q}_{ex}\cdot\vec{e}^r = 0 \quad . \qquad (2.22)$$

B) The continuity of the normal component of the perturbed magnetic

field at plasma surface (r=a),

$$\vec{Q}_{ex}\cdot\vec{e}^{r} = Q^{r}_{in} \quad . \tag{2.23}$$

C) The pressure balance equation at the plasma surface (r=a)[13],

$$-\gamma P_0\vec{\nabla}\cdot\vec{\xi} + \vec{B}_{in}\cdot\vec{Q}_{in} = \vec{B}_{ex}\cdot\vec{Q}_{ex} + \frac{\xi^r}{2}\left(\frac{dB^2_{ex}}{dr} - \frac{dB^2_{in}}{dr}\right) \quad , \tag{2.24}$$

where

$$\vec{Q}_{ex} = Q_\mu\vec{u}_\mu + Q_\eta\vec{u}_\eta + Q_\phi\vec{u}_\phi \quad . \tag{2.25}$$

Here $\vec{u}_\mu$, $\vec{u}_\eta$ and $\vec{u}_\phi$ are the unit vectors in the toroidal coordinate (μ,η,ϕ) respectively.

2.5 Remarks on the Code ZEPHYrus

In the code ZEPHYrus all variables are normalized by the following characteristic quantities;

1) minor radius of a plasma ring: a,
2) toroidal magnetic field at r=a: B_0,
3) plasma density averaged over minor cross section: $\langle\rho\rangle$,
4) Alfven velocity measured by B_0: $v_f=B_0/\sqrt{\langle\rho\rangle}$

and other associated normalization factors are toroidal Alfven transit time; $\tau_{ta}= a/v_f$, pressure; $B_0^2/2$ and growth rate; $\gamma_{ta}=1/\tau_{ta}$.

In order to avoid complexity of the program we adopt a simple explicit scheme for time-integration of the equations. To accelerate growth of instabilities at the marginal stability condition we introduce an artifitial shift of the growth rate α[8,9], by which the computation is carried out within a reasonable CPU time.

As for the computational grids in the r direction, we use half integral meshes for ξ^θ, ξ^ϕ, Q^θ, Q^ϕ, J^r and P and integral meshes for the other variables. On the other hand, only integral meshes are used in the θ direction. Considering the symmetry with respect to the median plane we calculate the solution only in upper half plane (Fig.2.3).

2.6 Check of Accuracy of the Code

To check accuracy of the code, we calculate the growth rate of the free boundary MHD instability (the kink mode) in a cylindrical plasma with uniform current distribution and fixed boundary MHD instability in a toroidal plasma expressed by a Solov'ev equilibrium[18]. The former growth rate is given analytically and the latter is calculated numerically by using the spectral code ERATO.
The equilibrium of the cylindrical plasma is given by specifying f(r), and h(r) as

$$\begin{aligned} f(r) &= rf_a \quad , \\ P_0(r) &= \beta_p f_a^2(1-r^2) \quad , \\ h(r) &= \sqrt{1 - 2f_a^2(1-\beta_p)(r^2-1)} \quad , \end{aligned} \tag{2.26}$$

where $f_a = f(a)$ and β_p is poloidal beta. The boundary condition is the same as toroidal one in the previous Section except that the perturbed magnetic field in the vacuum region is expressed by the modified Bessel functions.

In Fig.2.4, we show the growth rates of the kink mode in a cylindrical plasma computed by the code ZEPHYrus with the one computed by the analytical formula[14],

$$\gamma^2_{anal} = \frac{B_a^2}{a^2}\left[2(m-nq_a) - \frac{2(m-nq_a)^2}{1-(a/b)^{2m}}\right] \quad , \tag{2.27}$$

where B_a, q_a, and b are the poloidal magnetic field, safety factor at the plasma surface, and the radius of the conducting shell, respectively, m and n are the poloidal and toroidal mode number, respectively. For the calculation of Fig.2.4 a uniform current equilibrium with the shell position b=2a is considered. The curves in Fig.2.4 correspond to the numerical calculations with azimuthal mesh number J_{max}=19 (black circles), J_{max}=35 (open circles), and analytical calculation (broken lines).
The computed curves are shifted to the left when the azimuthal mesh numbers are not large enough. The quantities of the shift $\Delta(nq_a)$ at nq_a=3 are 0.17 and 0.04 for J_{max}=19 and 35, respectively, which is in good agreement with the analytical formula[15] of the shift, $\Delta(nq_a) = -\pi^2 m^3/6(J_{max}-3)^2$. Thus the shift of the marginal point is explained by the discretization in the azimuthal direction.

The Solov'ev equilibrium is obtained by solving the following equation with respect to the flux function Ψ.

$$\frac{\partial^2\Psi}{\partial X^2} - \frac{1}{X}\frac{\partial\Psi}{\partial X} + \frac{\partial^2\Psi}{\partial Z^2} = -X^2\frac{dP}{d\Psi} - \frac{1}{2}\frac{dI^2}{d\Psi} \quad , \tag{2.28}$$

where P and I are the function of Ψ only and we set

$$P = P_1(\Psi_s - \Psi) \quad ,$$

$$I^2 = I_0^2 + I_1\Psi \quad , \tag{2.29}$$

where

$$P_1 = \frac{a^2(1+E^2)}{q_0 R_0^2 E\sqrt{1-\delta}} \quad ,$$

$$I_1 = \frac{2a^2 R_0 \delta}{q_0 R_0 E\sqrt{1-\delta}} \quad . \tag{2.30}$$

Then the following solution for the Solov'ev equilibrium is obtained.

$$\Psi = \Psi_0\left[\frac{(X^2-\delta R_0^2)}{E^2}Z^2 + \frac{(X^2-R_0^2)^2}{4}\right] \quad , \tag{2.31}$$

where

$$\Psi_0 = \frac{Ea^2}{2q_0 R_0^2\sqrt{1-\delta}} \quad . \tag{2.32}$$

In the above equations (2.29)-(2.32), E represents vertical elongation of plasma cross section, q_0 is the value of safety factor on the magnetic axis, δ means the diamagnetic effect and Ψ_s is the value of Ψ at plasma surface respectively. In this case, instead of expansion with respect to the inverse aspect ratio we assume the relation between the cylindrical coordinate (X,ϕ,Z) and the curvilinear coordinate (r,θ,ϕ) as follows,[16]

$$X(r,\theta) = R_0\sqrt{1-\frac{2r}{R_0}\cos\theta} \quad , \tag{2.33}$$

$$Z(r,\theta) = \frac{Er\sin\theta}{\sqrt{1-\delta-(2r/R_0)\cos\theta}} \quad .$$

Then the equation

$$\Psi = \Psi_0 R_0^2 r^2 \quad , \tag{2.34}$$

holds and r=const. surfaces correspond to magnetic surfaces.
The functions f and h are in the following form,

$$f(r) = 2\Psi_0 R_0 r \quad ,$$

$$h(r) = \sqrt{1+I_1\Psi_0 r^2} \quad .$$

The other equilibrium quatities such as metric tensor are obtained in the same way as in Section 2.2. Growth rates of fixed boundary modes are calculated for the above Solov'ev equilibrium by using the codes ZEPHYrus and ERATO (Fig.2.5). The growth rate curve by the code ZEPHYrus shifts a little to left along the q_0 axis in comparison with the curve by ERATO and the growth rate by ERATO is a little larger. The shift of curve is attributable to the finite size of the computational mesh, which is corrected in the code ERATO, and the difference of magnitude of growth rates is attributed to the fact that the code ERATO is written on the basis of the finite hybrid element method[3]. Both the results agree well with each other on the whole.

2.7 Eigenfunction of Internal Mode

To analyze an internal mode of a toroidal plasma an equilibrium is prepared according to the prescription in Section 2.2. The current distribution with the order of ε^0 is assumed to be

$$j^{\phi}(r) \equiv R_0(P_0' + \frac{hh'}{R_0^2}) = j_0^{\phi}(1 - r^2)^3 \quad , \tag{2.36}$$

where j_0^{ϕ} is the current density at the magnetic axis. In the code ZEPHYrus j_0^{ϕ} is determined from the safety factor at the plasma surface, which is given as an input parameter. As an initial condition random numbers are assigned to the nodal values of ξ^r, and ξ^{ϕ}'s are set zero. The values of ξ^{θ} are determined by using the incompressibility condition $\vec{\nabla}\cdot\vec{\xi} = 0$.

The results of the calculation are summarized in Figs.2.6 and 2.7. Figure 2.6 shows time evolutions of the radial structure of Fourier decomposed displacement $\xi^r(r,\theta)$ for the cylindrical and toroidal plasmas. The last figure of each series of calculations shows almost the finally settled eigenfunction of the mode. In the cylindrical case (Fig.2.6 a) the internal mode with mode mumbers of m and n ((m,n) mode) grows at the corresponding resonant magnetic surface, i.e., the surface with $q = \frac{m}{n}$ (m/n resonant surface). In the toroidal cases (Fig.2.6 b,c), however, the (m,n) mode is localized not only at the m/n resonant surface but also at the m'/n resonant surface with $m' \neq m$, due to the toroidal coupling. Figure 2.7 shows the flow pattern of the displacement in the toroidal case. The pattern of T=295 is almost that of

the eigenfunction. It is seen that at inner region of the plasma column m=1 mode and at outer region m=2 mode grow, respectively.

2.8 Free Boundary Kink Mode

The effects of toroidicity and shell on the free boundary (external) kink mode are investigated for a uniform current plasma with $\beta_p=1$. The computational mesh number in the azimuthal direction (J_{max}) is chosen to be 19 throughont the series of calculations.

First, to study the toroidal effect we compute the growth rate and eigenfunction for plasma with various aspect ratio by fixing the shell radius b=2a, where a is the plasma minor radius. Figure 2.8 shows the growth rates of the $\varepsilon n=0.2$ kink mode versus nq_a. The growth rates of the mode for $\varepsilon^{-1}=15$ and 10 cases are almost the same as that for the cylindrical plasma ($\varepsilon^{-1}=\infty$). It seems reasonable since the toroidal effect is insignificant in these cases. In the case of $\varepsilon^{-1}=5$ the maximum growth rate of the mode becomes smaller in comparison with the cylindrical result. At the marginal stability region near $nq_a=2$, however, the mode for this case becomes more unstable and the narrow stability window observed in the analytically obtained cylindrical result disappears. The destabilization of the mode near the marginal stability region is mainly attributable to the toroidal coupling. The effect of the toroidal coupling is seen in the eigenfunctions of the m=2 external kink mode in Figs.2.9-2.11, where the eigenfunction becomes more distorted as the toroidicity becomes larger.

Next to study the shell effect on the stabilization of the external kink mode, we calculate the growth rate by locating the conducting shell near the plasma surface (b=1.2a). The results of the calculations are summarized in Fig.2.12 with the analytical results for a cylindrical plasma ($\varepsilon^{-1}=\infty$, broken line). The stabilizing effect of the shell is clearly seen by comparing the figure with Fig.2.8, where the shell radius b is twice the plasma minor radius. In the b=1.2a case the toroidal effect is more remarkable in comparison with the b=2a case, which is in good agreement with the previous analytical work by Frieman et al.[17]. Figure 2.12 shows that the toroidicity affects the mode even in a slender plasma with $\varepsilon^{-1}=15$, and stabilizes it considerably when the aspect ratio is as small as 7. Moreover, the destabilization of the

mode near the region of minimum growth rate is not observed when the shell is located very close to the plasma surface as b=1.2a. The residual instability with small growth rate is observed near the region of nq_a=2.0 for the cases of ε^{-1}=10 and 15 (Fig.2.12). This is attributed to the internal mode instability. In Fig.2.12 the growth rate the m=2 internal mode instability of a cylindrical plasma ($\varepsilon^{-1}=\infty$) is shown by a broken line near the region of nq_a=2.0. Figure 2.13 shows how the initial perturbation of the m=3 external kink type evolves to the eigenfunction of the m=2 internal mode when the safety factor at the surface is 2.0. The importance of the toroidal coupling is more clearly seen in the time evolution of Fourier decomposed displacement $\xi^r(r,\theta)$ (Fig.2.13). In this calculation the eigenfunction of the m=2 external kink mode of a cylindrical plasma is chosen as an initial perturbation.

2.9 Conclusions and Discussion

To study a linearized ideal MHD mode a time evolutional code ZEPHYrus is developed and the accuracy of the code is checked by comparing the computed growth rate with analytical one and numerical one by the spectral code ERATO. The results is almost satisfactory except that the curve of the growth rate vs. safety factor shifts a little due to the finite size of computational meshes.

It is shown that when the shell is placed far from the plasma surface (b=2a), the toroidicity scarcely affects the external kink modes for a slender tokamak, but it reduces the growth rate for a fat tokamak. When the shell is placed close to the plasma surface (b=1.2a), the toroidal effect is notable in comparison with the case of b=2a, and m=2 external kink mode is considerably stabilized in a fat tokamak. The code ZEPHYrus is accurate for a low m mode, but for a higher m mode the above mentioned numerical shift prevents accurate calculation of the growth rate. In order to avoid the numerical error Fourier expansion of the perturbed variables and equilibrium quantities seem to be effective.

References

1) I.B. Bernstein, E.A. Frieman, M.D. Kruskal and R.M. Kulsrud, Proc. Roy. Soc. A244 (1958) 17.
2) T. Takeda, Y. Shimomura, M. Ohta, and M. Yoshikawa, Phys. Fluids 15, (1972) 2193.
3) R. Gruber, F. Troyon, D. Berger, L.C. Bernard, S. Rousset, R. Schreiber, W. Kerner, W. Schneider and K.V. Roberts, Comput. Phys. Commun. 21, (1981) 323.
4) R.C. Grimm, J.M. Greene and J.L. Johnson, Methods in Computational Physics, (Academic Press, New York, 1976) Vol.16 P.253.
5) A.M.M. Todd, M.S. Chance, J.M. Greene, R.C. Grimm, J.L. Johnson and J. Manickam, Phys. Rev. Lett. 11,(1977) 826.
6) W. Kerner, R. Gruber and F. Troyon, Phys. Rev. Lett. 25,(1980) 536.
7) T. Tsunematsu, T. Takeda, G. Kurita, M. Azumi, T. Matsuura, R. Gruber and F. Troyon, "Beta-Limit of a Large Tokamak with a Circular Cross-Section", Japan Atomic Energy Research Institute Report JAERI-M 9890 (1982).
8) J.A. Wesson and A. Sykes, in Plasma Physics and Controlled Nuclear Fusion Research (Proc. 5th Int. Conf. Tokyo, 1974) CN-33/A12-3.
9) A. Sykes and J.A. Wesson, Nucl. Fusion 14, (1974) 645.
10) G. Bateman, W. Schneider and W. Grossmann, Nucl. Fusion 14, (1974) 669.
11) J.M. Greene, J.L. Johnson and K.E. Weimer, Phys. Fluids 14, (1971) 671.
12) M. Okamoto, M. Wakatani and T. Amano, Nucl. Fusion 15, (1975) 225.
13) B.B. Kadomtsev, Reviews of Plasma Physics, (Consultants Bureau, New York 1966) Vol.2 P.153.
14) V.D. Shafranov, Sov. Phys., Tech. Phys. 15, (1970) 175.
15) T. Takizuka, S. Tokuda, M. Azumi and T. Takeda, Comput. Phys. Commun. 23, (1981) 19.
16) W. Kerner, Nucl. Fusion 16, (1976) 643.
17) E.A. Frieman, J.M. Greene, J.L. Johnson and K.E. Weimer, Phys. Fluids 16, (1973) 1108.
18) L.S. Solov'ev, Sov. Phys. JETP 26, (1968) 400.

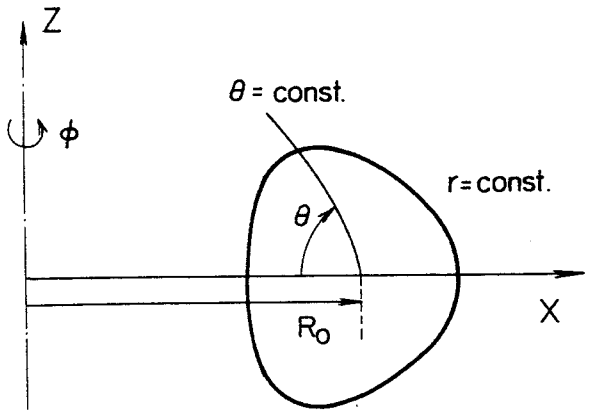

Fig.2.1 Curvilinear coordinate system (r,θ,ϕ). The closed curve (r=const.) is the intersection of a magnetic surface.

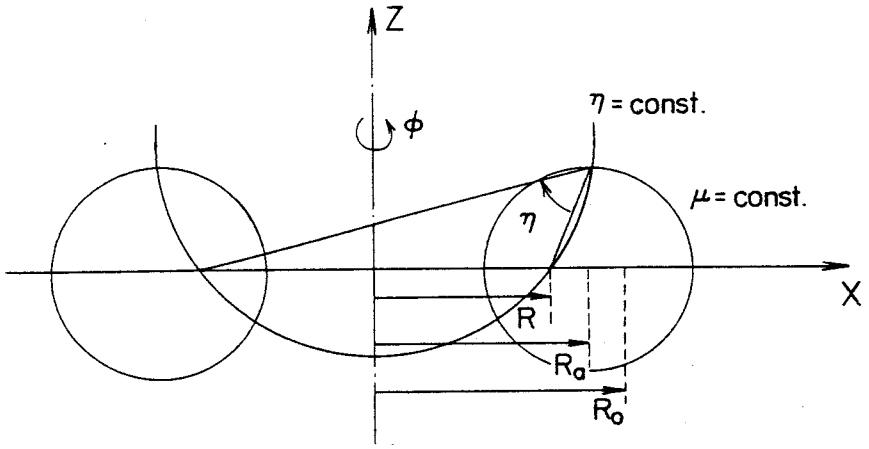

Fig.2.2 Toroidal coordinate system (μ,η,ϕ) used for the calculation of vacuum magnetic field. R_a is the radius of the center of circular plasma surface and R, the singular point of toroidal coordinate, $R=\sqrt{R_a^2-a^2}$.

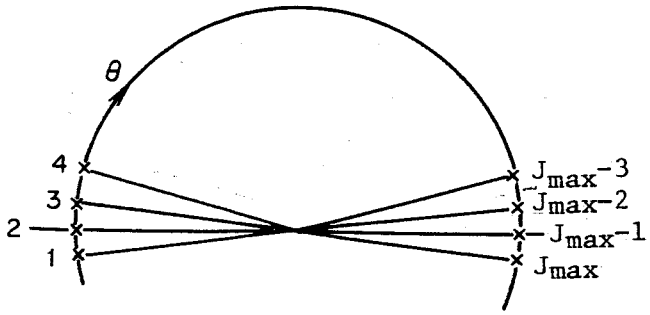

Fig.2.3 Grid points in the θ direction. The grid points of J=2 and $J=J_{max}-1$ represent θ=0 and θ=π, respectively.

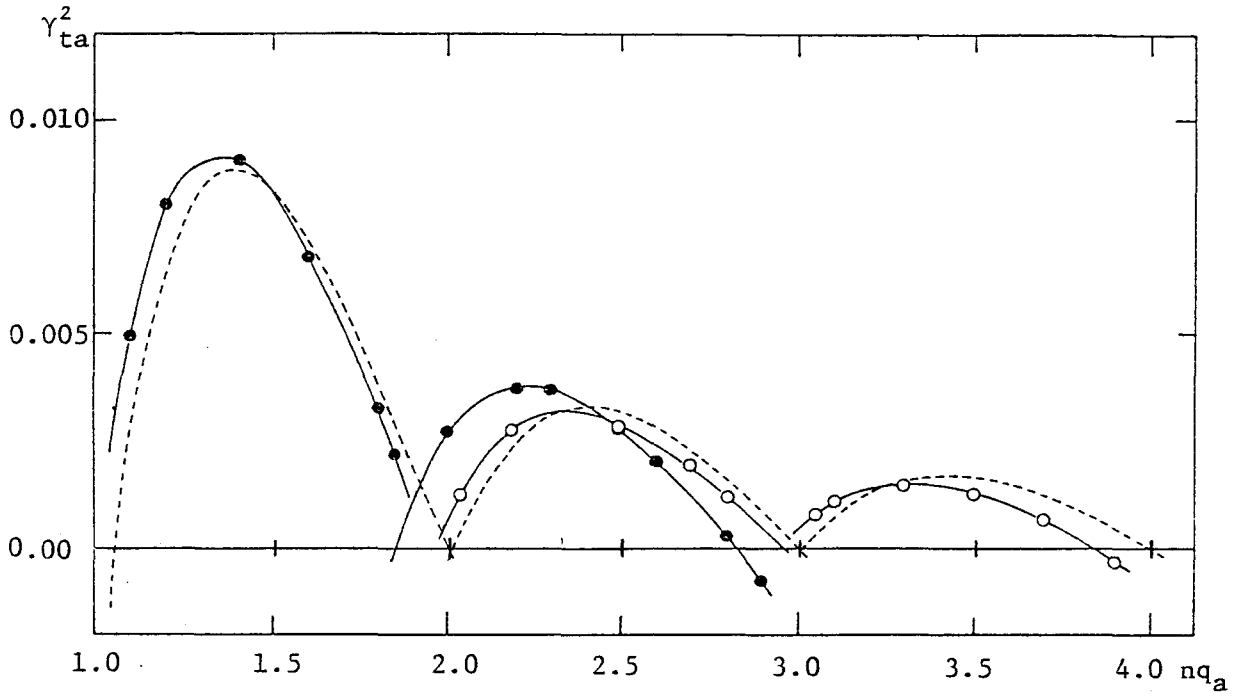

Fig.2.4 Growth rate as a function of safety factor at plasma surface r=a multiplied by the toroidal mode number n. Black and open circles denote the computed growth rate with the azimuthal mesh number J_{max}=19 and J_{max}=35, respectively. The broken lines are analytical growth rate obtained by Eq.(2.27).

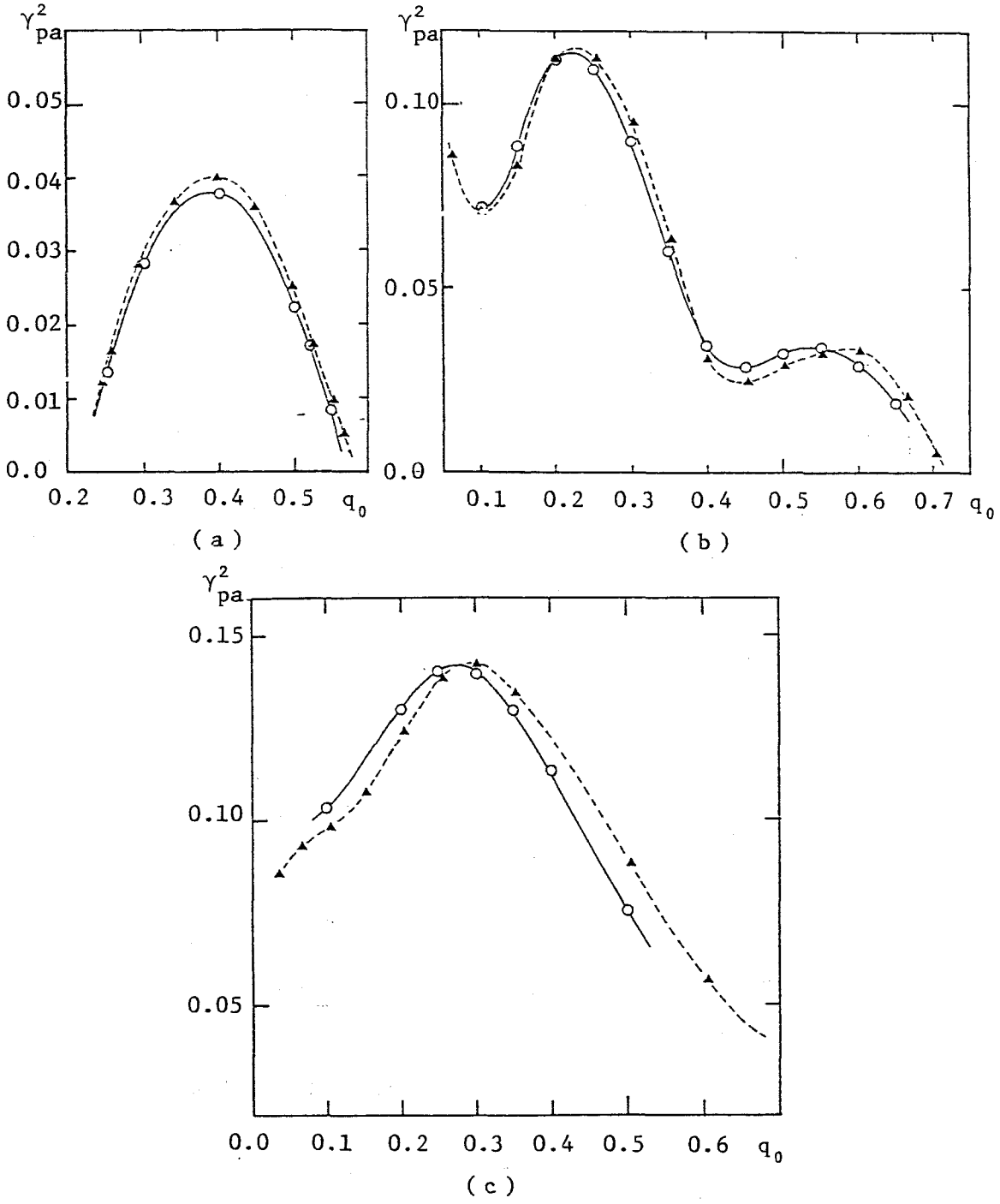

Fig.2.5 Comparison of growth rate by two codes vs. safety factor at magnetic axis. The solid and broken lines show the growth rates obtained by ZEPHYrus and ERATO codes, respectively. The parameters in this calculation are: (a) E=1, n=2, (b) E=1, n=3 and (c) E=2, n=2. The aspect ratio ε^{-1}=3 for all cases. The growth rates are normalized to the poloidal Alfven transit time.

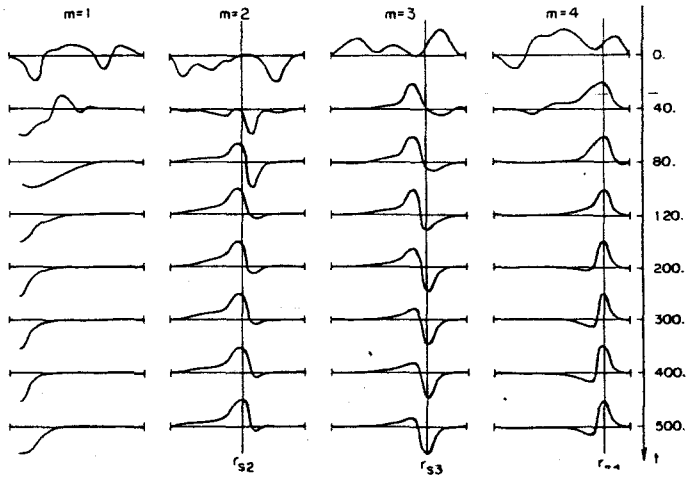

(a) Cylindrical case, $(q_0, q_a) = (1.0, 6.0)$, n=1.

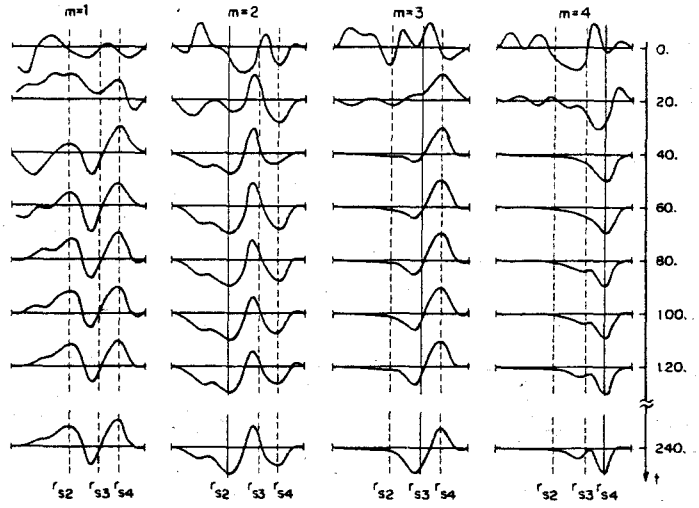

(b) Toroidal case, $(q_0, q_a) = (1.5, 6.54)$, n=1.

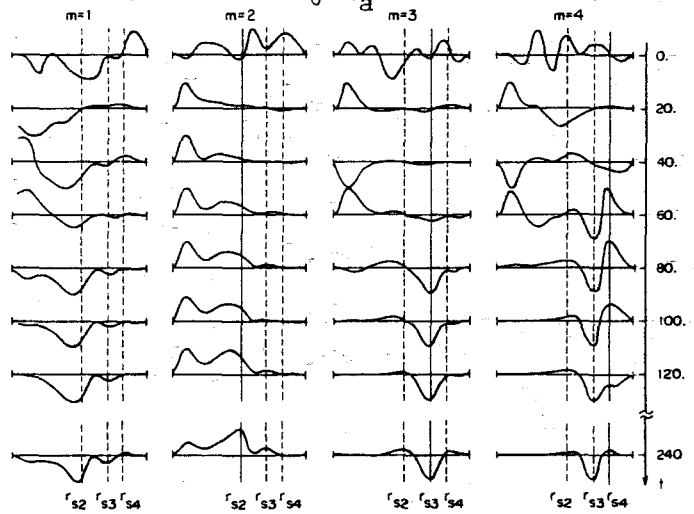

(c) Toroidal case, $(q_0, q_a) = (0.46, 1.96)$, n=3.

Fig.2.6 Time development of the Fourier component of $\xi^r(r,\theta)$ expanded in θ direction. q_0 and q_a are the values of safety factor at magnetic axis and plasma surface, respectively. Ordinate denotes time normalized to toroidal Alfven transite time and, in each subfigure, abscissa represents a minor radius of a plasma column and r_{sm} denotes the position of singular surface of m-mode.

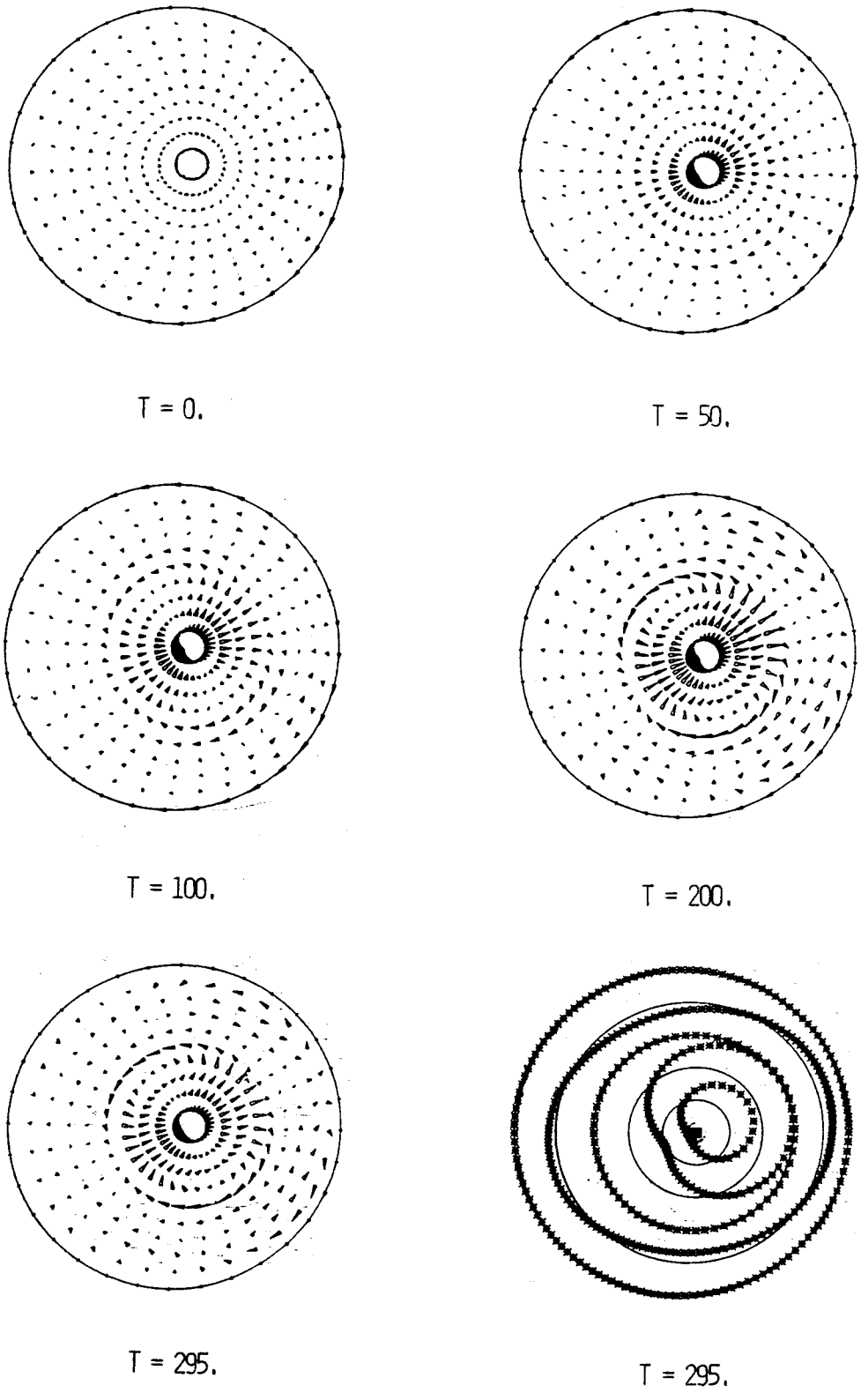

Fig.2.7 Flow pattern of cross-sectional displacement of internal mode for $\varepsilon^{-1}=5$, $\beta_p=1$, n=1 and $(q_0,q_a)=(0.76,3.19)$. Last subfigure shows displacement of the plasma with respect to the equilibrium magnetic surfaces (solid curves).

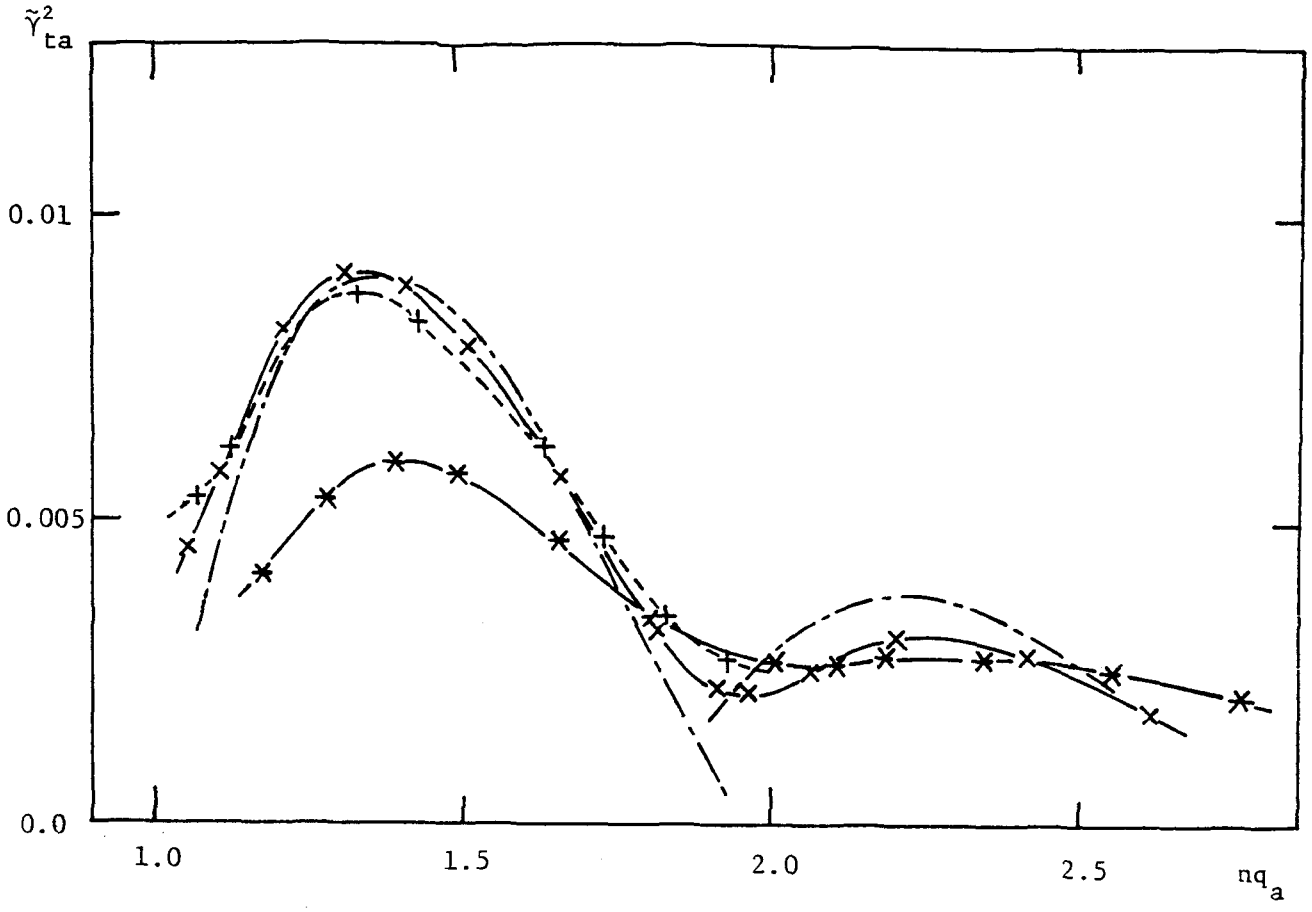

Fig.2.8 Growth rate vs. nq_a, for $\varepsilon n=0.2$. Dotted solid curve is the growth rate in cylindrical case and other curves are toroidal cases in which the solid line with the mark ×, broken line with the mark + and solid line with the mark * denote the cases of $\varepsilon^{-1}=15$, $\varepsilon^{-1}=10$ and $\varepsilon^{-1}=5$, respectively, for $\beta_p=1$, $b=2a$ and uniform current distribution.

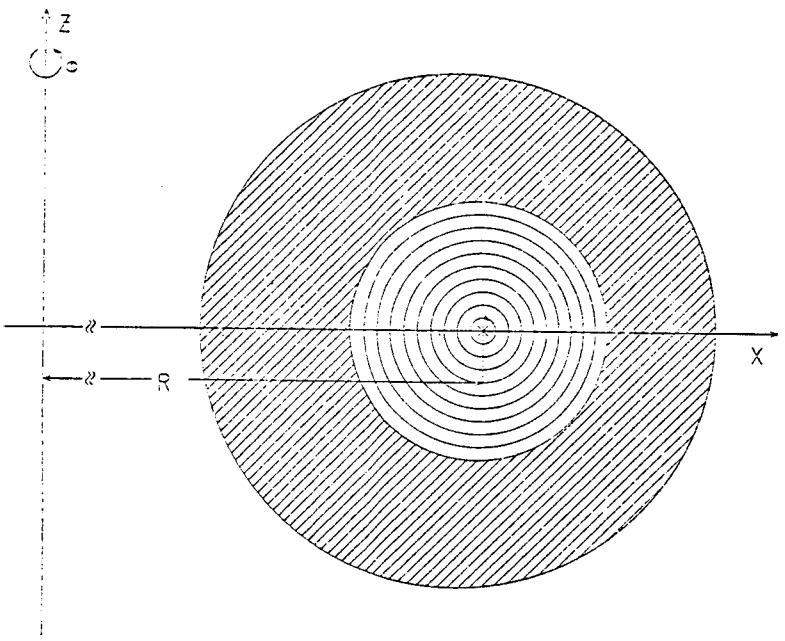

Fig.2.9

a) Equilibrium of a uniform current plasma with $\varepsilon^{-1}=15$, $\beta_p=1$, b=2a. Shaded region is vacuum and the conducting shell is placed at the outer boundary of the region.

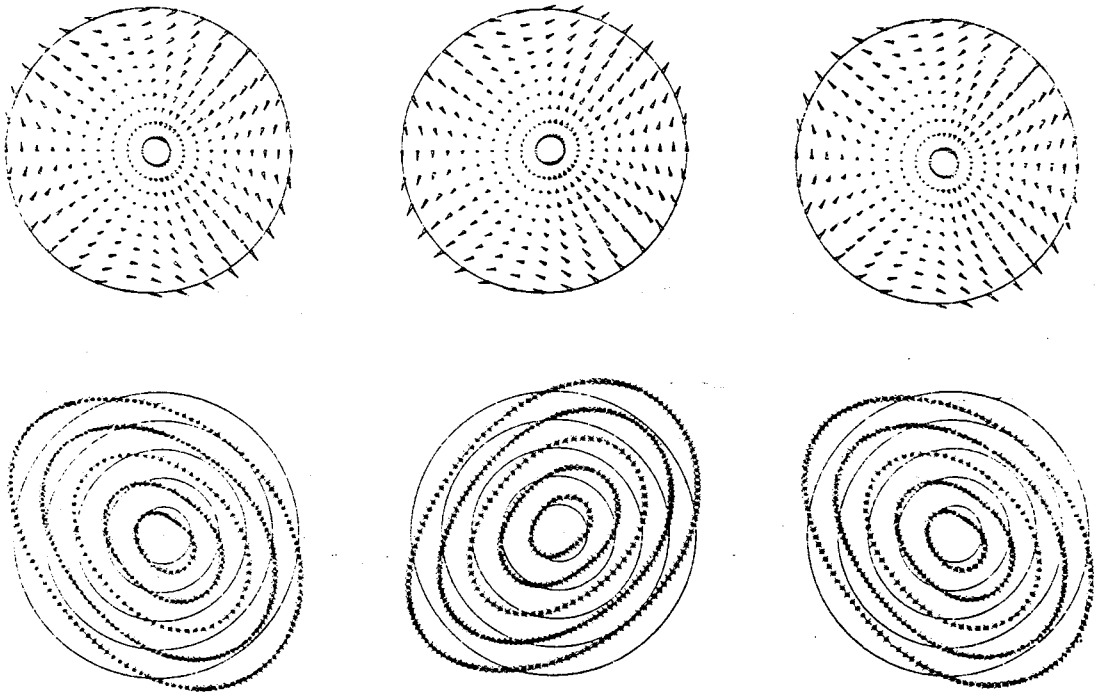

b) Eigenfunctions of the m=2 external mode for $q_0 = 1.2$ and $n = 3$ at three different toroidal locations.

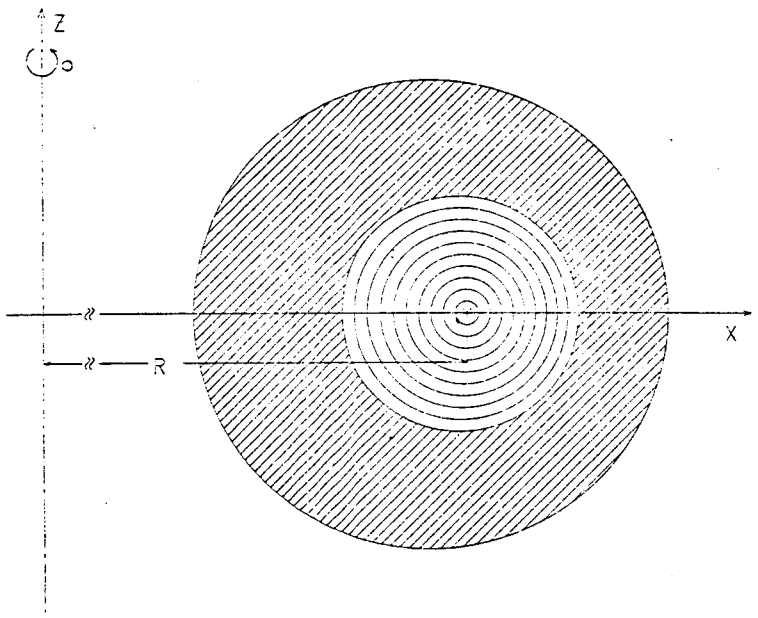

Fig.2.10

a) Equilibrium magnetic of a uniform current plasma with $\varepsilon^{-1}=10$, $\beta_p=1$, b=2a.

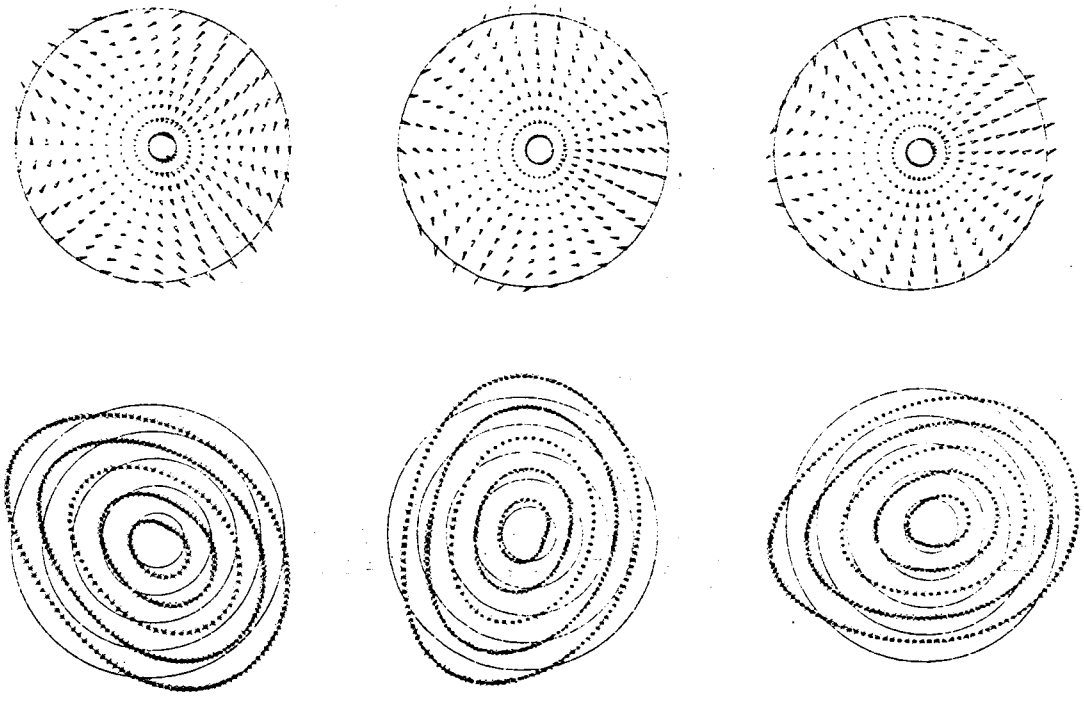

b) Eigenfunctions of the m=2 external mode for $q_0=1.2$ and n=2 at three different toroidal locations.

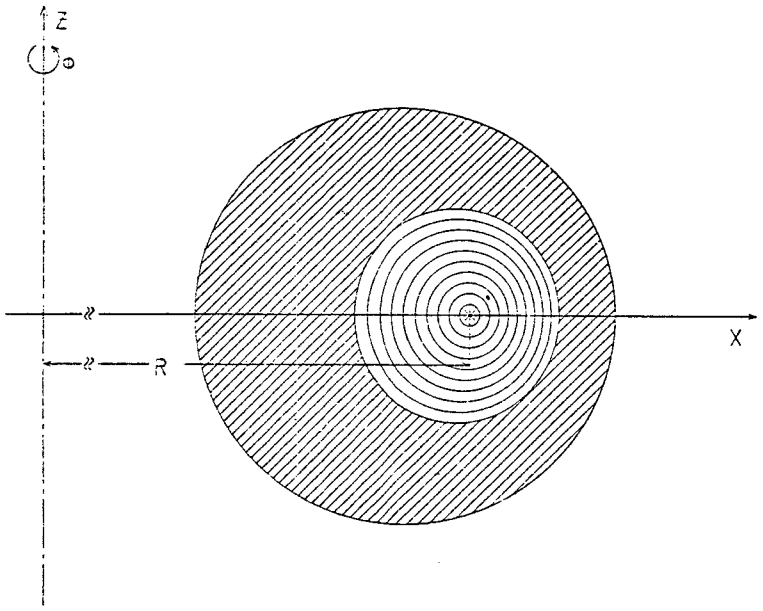

Fig.2.11

a) Equilibrium magnetic of a uniform current plasma with $\varepsilon^{-1}=5$, $\beta_p=1$, b=2a.

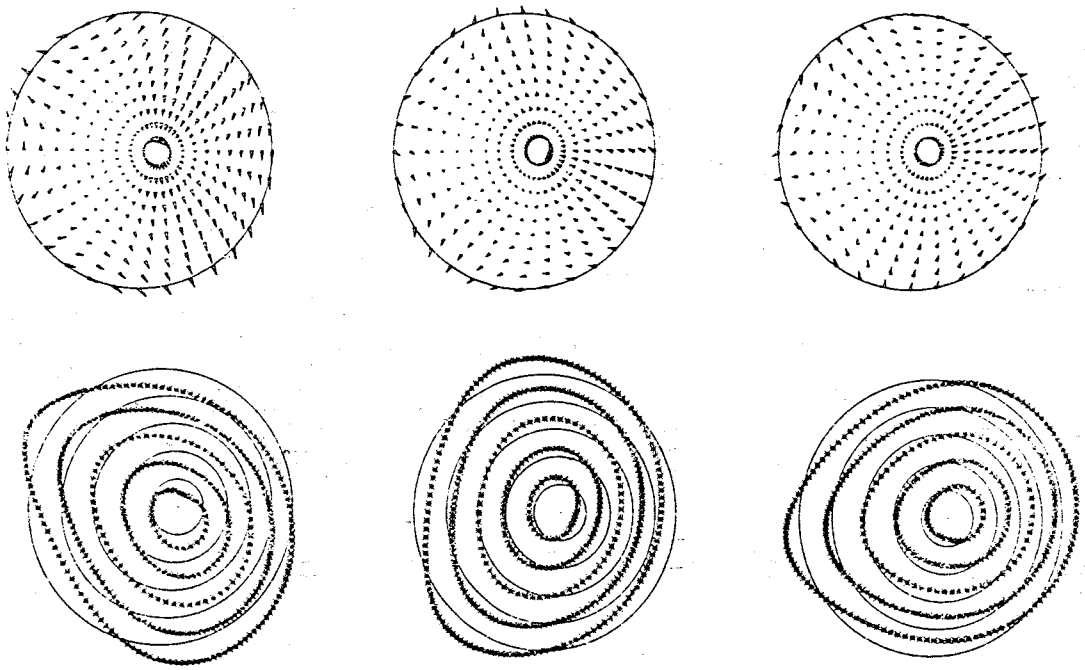

b) Eigenfunctions of the m=2 external mode for $q_0=1.2$ and n=1 at three different toroidal locations.

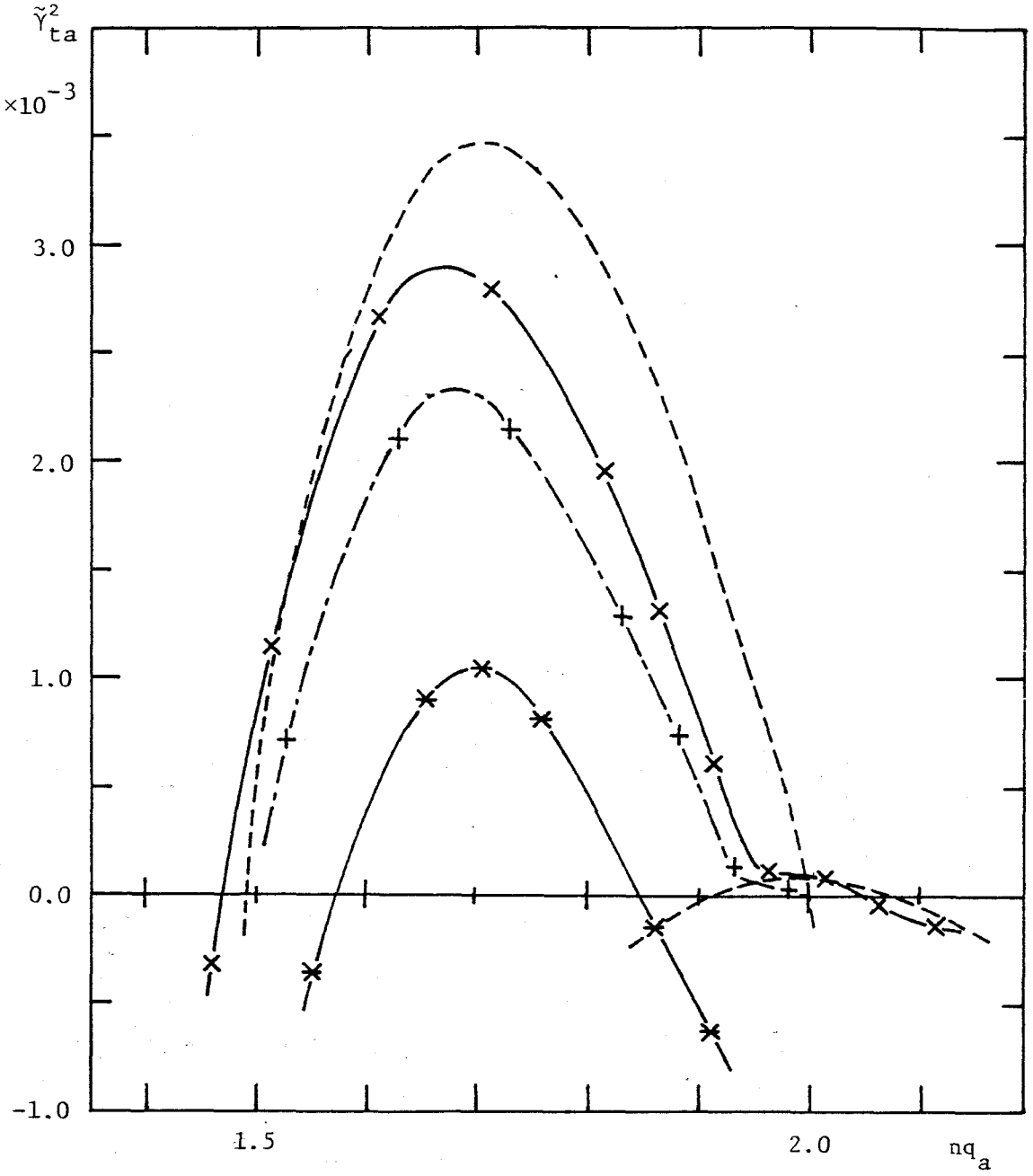

Fig.2.12 Growth rate vs. nq_a for $\varepsilon n=0.2$. Broken lines show cylindrical growth rate and other lines show toroidal ones, in which solid line with the mark ×, dotted solid line with the mark + and solid line with the mark ⋆ denote the cases of $\varepsilon^{-1}=15$, $\varepsilon^{-1}=10$ and $\varepsilon^{-1}=7$, respectively, for $\beta_p=1$, $b=1.2a$ and uniform current distribution.

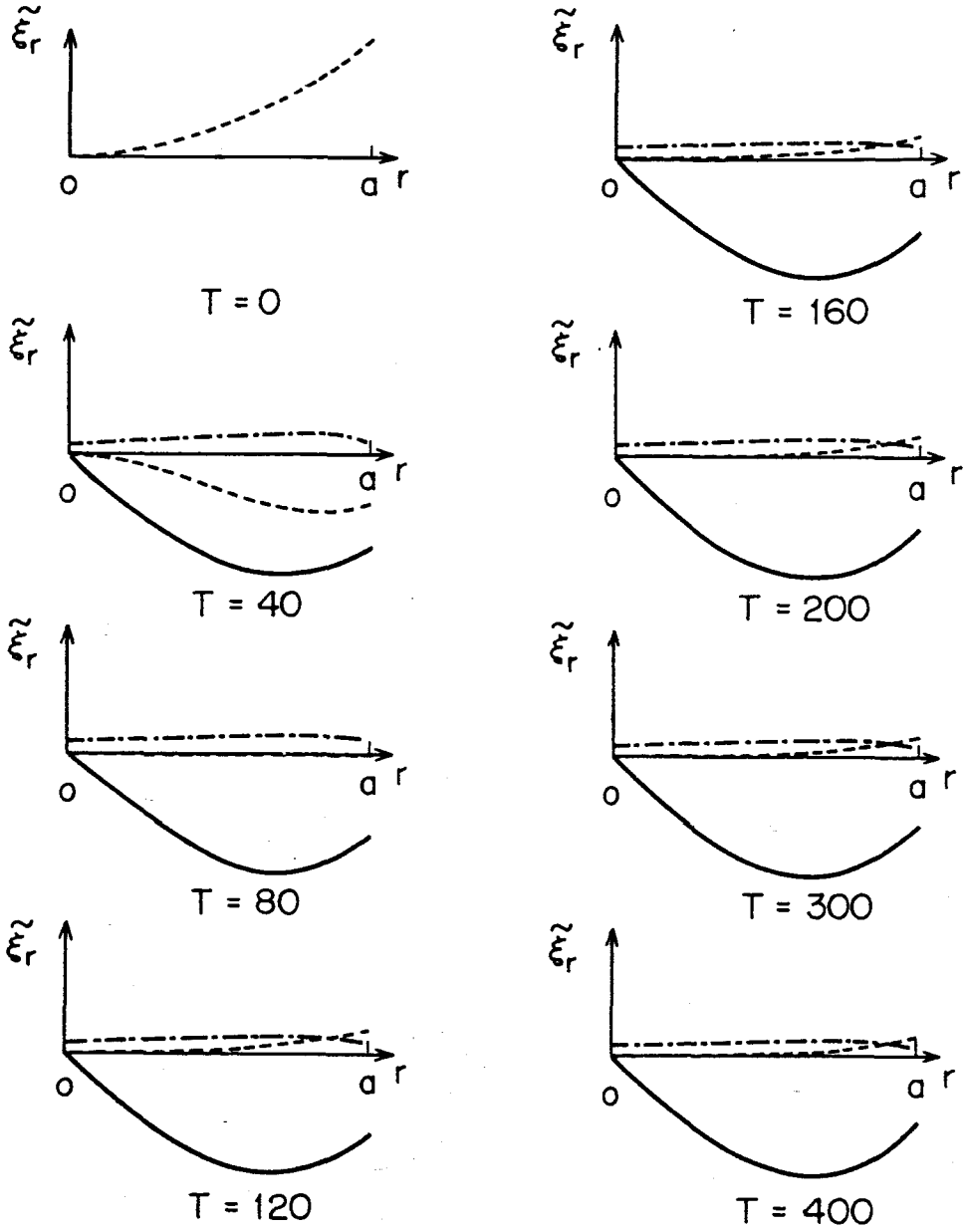

Fig.2.13 Time development of the Fourier component of $\xi^r(r,\theta)$ expanded in θ direction for $\varepsilon^{-1}=15$, $q_a=2.0$ and uniform current distribution. Solid, broken and dotted solid lines denote m=2, m=3 and m=1 modes, respectively. They are normalized to its maximum value in each subfigure.

Chapter III

Development of Nonlinear Code for Analysis of Positional Instability

A free boundary nonlinear MHD code, AEOLUS-P is developed to investigate a positional instability in a tokamak. A new rezoning algorithm in combination with the dynamical grid method is adopted. The results for a cylindrical plasma model are in good agreement with those by a one-dimensional spectral code THALIA and it is concluded that the new method is useful for this kind of the problems.

3.1 Introduction

The positional instability in a tokamak is a very violent one and the tokamak should be operated under the condition absolutely without the instability. This instability is an axisymmetric (n=0) ideal MHD mode and it imposes severer restriction on the plasma confinement in a noncircular cross-sectional tokamak device which will be more popular among future devices.

The linear positional instability in a shell-less tokamak has been investigated by many authors for the case that all currents except the plasma current are constant[1~3], or the case that the plasma current is kept constant[4]. By considering a simple equivalent circuit for the shell-less tokamak Seki et al.[5] obtained the general stability condition including both the cases mentioned above. This work is extended to include an effect of a resistive shell[6].

There is a difficulty in the numerical calculation of the nonlinear behavior of the instability as the mode is an essentially external one and the evolution of a free boundary plasma should be computed. In order to analyze the positional instability in the PDX tokamak Jardin has developed a nonlinear positional code and has made some numerical analyses on this problem[7,8]. Up to now the series of the works by Jardin is almost the only works on the nonlinear positional instability and this problem has not been solved thoroughly.

Fortunately it is shown by the MHD spectral code[9] and nonlinear MHD code[8] that a passive coil system has a stabilizing effect on this

mode and, at least, the time scale of the mode can be made long enough by the passive coil system. It will be, consequently, possible that the mode could be made harmless by the combination of the passive coil and feedback stabilizations[10,11]. Theoretical investigations, especially, nonlinear analyses of the positional instability are, therefore, very important to design a future toroidal device so that the positional instability is not destructive in the devise.

In this Chapter, we describe the two-dimensional nonlinear MHD code, AEOLUS-P developed to investigate a numerical method for analyses of the nonlinear positional instability in a tokamak device, especially, with an external coil system for a divertor or magnetic limiter such as equipped in the JT-60 tokamak (Fig. 3.1). In Section 3.2, the basic equations of ideal MHD equations are transformed to an integral form. The numerical procedure is presented in Section 3.3. In Section 3.4 results for a cylindrical model are shown. We give a summary in Section 3.5.

3.2 Formulation

The following set of the ideal MHD equations is used as basic equations in the nonlinear MHD code AEOLUS-P,

$$\frac{\partial}{\partial t}\rho + \vec{\nabla}\cdot(\rho\vec{v}) = 0 \quad ,$$

$$\frac{\partial}{\partial t}(\rho\vec{v}) + \vec{\nabla}\cdot(\rho\vec{v}\vec{v}) = -\vec{\nabla}P^{*} + \vec{\nabla}\cdot(\vec{B}\vec{B}) \quad , \tag{3.1}$$

$$\frac{\partial}{\partial t}P^{1/\gamma} + \vec{\nabla}\cdot(P^{1/\gamma}\vec{v}) = 0 \quad ,$$

$$\frac{\partial}{\partial t}\vec{B} + \vec{\nabla}\cdot(\vec{B}\vec{v}) - \vec{\nabla}\cdot(\vec{v}\vec{B}) = 0 \quad ,$$

where $P^{*} \equiv P + \frac{1}{2}B^{2}$ is the total pressure. Since the aim of the code is to compute nonlinear free boundary problems, we adopt the dynamical grid method proposed by Jardin et al.,[7] which seems more appropriate to the problem rather than Eulerian or Lagrangian method. In the dynamical grid method, the total velocity $\vec{v}$ is divided into the Euler velocity

$\vec{v}_E$ and grid velocity $\vec{v}_G$; $\vec{v} = \vec{v}_E + \vec{v}_G$, and the total time derivative of a quantity f integrated in the region Γ_k can be written in the form

$$\frac{D}{Dt}\int^{\Gamma_k} f d\tau = \int^{\Gamma_k}\left[\frac{\partial f}{\partial t} + \vec{\nabla}\cdot(f\vec{v}_G)\right]d\tau \quad . \tag{3.2}$$

Instead of the finite difference method adopted by Jardin we use the finite element approach based on the following integral forms of euqations of the complete conservative form in the Cartesian coordinates[12],

$$\begin{aligned}
&\frac{D}{Dt}\int^{\Gamma_k}\rho d\tau = -\int^{\Gamma_k}\rho\vec{v}_E\cdot d\vec{S} \quad ,\\
&\frac{D}{Dt}\int^{\Gamma_k}\rho v_i d\tau = -\int^{\Gamma_k}[\rho v_i\vec{v}_E + p^*\vec{e}_i - B_i\vec{B}]\cdot d\vec{S} \quad ,\\
&\frac{D}{Dt}\int^{\Gamma_k} p^{1/\gamma} d\tau = -\int^{\Gamma_k} p^{1/\gamma}\vec{v}_E\cdot d\vec{S} \quad ,\\
&\frac{D}{Dt}\int^{\Gamma_k} B_i d\tau = -\int^{\Gamma_k} [B_i\vec{v}_E - v_i\vec{B}]\cdot d\vec{S} \quad ,
\end{aligned} \tag{3.3}$$

where $\vec{e}_i$ is the unit vector and subscript i represents the i-th component of a vector. Since the code AEOLUS-P analyzes axisymmetric modes, these equations in the three dimensional space are reduced to those in the two dimensional space. At first, we consider a straight system for simplicity where all variables have no z dependence, i.e. $\partial/\partial z = 0$, and employ the grid configuration in the x-y plane as shown in Fig. 3.2. The volume integral $\int f d\tau$ is transformed to a surface integral and approximately given as $f_0\Omega$ (f_0 is the value of f at the grid point 0 in Fig. 3.2 and Ω is the area of the hatched region). The surface integral $\int ds$ in the r.h.s. of the equations is also transformed to a line integral and approximately given as $\frac{1}{2}[(f_1+f_2)s_{12} + (f_2+f_3)s_{23} + (f_3+f_4)s_{34} + (f_4+f_5)s_{45} + (f_5+f_6)s_{56} + (f_6+f_1)s_{61}]$ (s_{12} is the length between the grid points 1 and 2). For the case of the axisymmetric torodial calculation, some terms due to the toroidal curvature should be added to the r.h.s. of the above set of integrated equations. Details are described in the Appendix.

3.3 Numerical Method

The MHD equations described in the former Section are solved under the fixed boundary condition

$$\vec{v}\cdot\vec{n} = 0 \quad (\vec{n} : \text{normal vector of the plasma surface}), \tag{3.4}$$

or the free boundary condition

$$P^*\big|_{plasma} = \frac{1}{2} B^2\big|_{vacuum} \quad , \tag{3.5}$$

at the plasma-vacuum boundary. The vacuum field is obtained by introducing the poloidal flux function ψ and the vacuum toroidal field constant g_v,

$$\vec{B} = B_0(\vec{\nabla}\phi \times \vec{\nabla}\psi + g_v\vec{\nabla}\phi) \quad . \tag{3.6}$$

The normal derivative of ψ at $\vec{x} = \vec{x}_i = (x_i, y_i)$ on the plasma-vacuum is derived from the set of equations

$$\frac{1}{2\pi}\oint \frac{ds}{x_i'} G_{ii'} \frac{d\psi}{dn}\Big|_{x_i'} = \psi_b - \psi_{shell} - \sum_m j_m G_{im} \quad , \tag{3.7}$$

where x_i is the distance from the toroidal axis, ψ_b and ψ_{shell} are constant in time, and j_m is the poloidal coil current at $\vec{x} = \vec{x}_m$ (Fig. 3.3). Green's function $G_{ii'}$ of the equation

$$\Delta^* G_{ii'} = x\delta(\vec{x} - \vec{x}_{i'}) \quad , \tag{3.8}$$

is easily obtained analytically when the shell has a circular cross-section. The toroidal field constant g_v is computed by using the condition of the toroidal flux conservation in the vacuum region as

$$\frac{1}{2\pi}\int_{vacuum} \vec{\nabla}\phi\cdot\vec{B}d\tau = \text{constant}. \tag{3.9}$$

In the dynamical grid method the grid velocities are free parameters and they are given arbitrarily under the condition that the center grid is always on the magnetic axis and the boundary grids are always on

the plasma boundary. The center grid is, therefore, a purely Lagrangian grid and the grid velocity equals the total plasma velocity, that is,

$$\vec{v}_{G,a} = \vec{v}_a \quad . \tag{3.10}$$

It is not adequate to choose the boundary grids as purely Lagrangian grids because the two-dimensional Lagrangian meshes usually distort considerably during the simulation. Some rezoning process should be included for the time integration. Development of an efficient rezoning algorithm is, therefore one of the most important purposes of this work. In the following we describe the numerical method composed of the dynamical grid method and rezoning algorithm. In this Chapter, "rezoning algorithm" means not the "smoothing algorithm"[12] but how to determine the grid velocity $\vec{v}_G$. In our rezoning algorithm, shown below, the grids never intersect each other and the strong distortion of grids never occurs.

The new position of the center grid $\vec{x}_a^n$ and new position of boundary grid $\vec{x}_b^n$ are represented by the grid velocity $\vec{v}_G$ as follows,

$$\begin{aligned} \vec{x}_a^n &= \vec{x}_a + \delta t\, \vec{v}_{G,a} \quad , \\ \vec{x}_b^n &= \vec{x}_b + \delta t\, \vec{v}_{G,b} \quad . \end{aligned} \tag{3.11}$$

Next, we determine the positions of new boundary grids so that the areas of the triangles made of two adjacent boundary grids, $(\vec{x}_j^n, \vec{x}_{j+1}^n)$, and center grid, $\vec{x}_a^n$, are the same each other. This condition can be written as follows,

$$\begin{aligned} (\vec{v}_{G,j+1} - \vec{v}_{G,a}) \times (\vec{x}_j - \vec{x}_a) = (\vec{v}_{G,j} - \vec{v}_{G,a}) \times (\vec{x}_{j+1} - \vec{x}_a) \\ - \sum^{N_\theta} \vec{v}_j \times (\vec{x}_{j+1} - \vec{x}_{j-1})/N_\theta \quad , \end{aligned} \tag{3.12}$$

where subscript j means the grid position at the plasma surface and N_θ is the azimuthal mesh number. The boundary grid velocity also satisfy the following condition,

$$\vec{v}_{G,b} \cdot \vec{n} = \vec{v}_b \cdot \vec{n} \quad , \tag{3.13}$$

or

$$\vec{v}_{G,b}\times(\vec{x}_{j+1}-\vec{x}_{j-1}) = \vec{v}_b\times(\vec{x}_{j+1}-\vec{x}_{j-1}) \quad , \tag{3.14}$$

where $\vec{n}$ is the unit vector normal to the plasma surface. From Eqs.(3.12) and (3.14), we obtain the boundary grid velocity $\vec{v}_{G,b}$. The new positions of the boundary grid are determined by substituting the boundary velocity thus obtained into Eq.(3.11). Lastly other grids are moved onto a straight line between the center grid and a boundary grid so that grids are distributed with the equal interval in a squared length scale from the axis.

In a new grid system all meshes have equal area and the grid velocity is represented as

$$\vec{v}_G = (\vec{x}^n - \vec{x})/\delta t \tag{3.15}$$

The values of physical quantities ρ, $\vec{v}$, P and $\vec{B}$ at the time $t = t+\delta t$ are computed by using the predictor corrector time integration scheme.

3.4 Results for a Cylindrical Model

In this Section, we show the results for the n=0 mode in a cylindrical plasma model with uniform mass and uniform current distributions. The equilibrium poloidal magnetic field at the plasma surface B_s is chosen as $B_s/B_0 = 1.0$ and 0.2. As an initial condition of the calculation we choose the analytically obtained eigenfunction with the poloidal mode number m and amplitude $|\vec{\xi}/a| \sim 10^{-2}$.

First, we simulate several n=0 modes in a fixed boundary plasma with a cylindrical model. The results of calculations are shown in Figs. 3.5-3.7, where the radial and azimuthal mesh numbers N_r and N_θ are chosen to be 20 and 40, respectively. Figures 3.5 and 3.6 are the cases for $B_s/B_0 = 1.0$ and Fig. 3.7 is the case for $B_s/B_0 = 0.2$. The m=0 compressional mode is shown in Fig. 3.5 and the m=2 modes are shown in Figs. 3.6 and 3.7, where subfigures (a) and (b) correspond to the Alfven and compressional modes, in the respective order. The spectra of the system are computed by the one-dimensional spectral code THALIA[13] (Fig. 3.8) and the results of the simulation are compared with them (TABLE 3.1). Though there are slight differences between the results, the agreement between them are satisfactory. The above results for

the m=2 fixed boundary modes are the same as those of the Eulerian calculation, because the center grid is not moved. On the other hand, the center grid is moved in the case of the m=1 mode. The m=1 Alfven mode computed by (1) the Eulerian method and (2) dynamical grid method are compared in Fig. 3.9, where the velocities of the center grid and boundary grids are shown by broken and solid lines, respectively. Two cases give essentially the same results and the rezoning method adopted here is appropriate for the fixed boundary problem.

Next, calculations with a free boundary condition are carried out for m=0 and m=1 Alfven modes. In both the calculations the shell is located at r=2a. For the m=0 case the initial velocity perturbation is given and for the m=1 case the initial condition is given as rigid displasement of a plasma column instead of the velocity perturbation. Figure 3.10 shows the radial velocity oscillations of the m=0 Alfven mode at r=a and r=a/2. The oscillations of the m=1 mode at r=0 and r=a/2 are shown in Fig. 3.11. Figure 3.12 shows the flow patterns of the velocity field at t=2.5 and 5.5. Frequencies of the oscillations by the free boundary calculations are also in good agreement with those obtained by the code THALIA.

3.5 Summary

We have developed the free boundary nonlinear MHD code, AEOLUS-P for the analysis of the positional instability of a tokamak. Numerical scheme based on the dynamical grid method by Jardin is adopted in combination with a new rezoning algorithm which makes the area of each computational mesh constant.

The computed frequencies of oscillations in a cylindrical model are in good agreement with those obtained by the one-dimensional spectral code THALIA and it is concluded that the new numerical method works satisfactorily for the calculation of the axisymmetric MHD modes.

References

1) S.M. Osovets, Plasma Physics and the Problem of Controlled Thermonuclear Reactions, (Pergamon Press, Oxford, 1959) Vol.2 P.322.
2) S. Yoshikawa, Phys. Fluid 7, (1964) 278.
3) V.S. Mukhovatov and V.D. Shafranov, Nucl. Fusion 11. (1971) 605.
4) J.M. Greene, J.L. Johnson and K.E. Weimer, Phys. Fluids 14, (1971) 671.
5) S. Seki, H. Momota and R. Itatani, J. Phys. Soc. Japan 36, (1974) 1667.
6) A. Fukuyama, S. Seki, H. Momota and R. Itatani, Jap. J. Appl. Phys. 14, (1975) 871.
7) S.C. Jardin, J.L. Johnson, J.M. Greene and R.C. Grimm, J. Comp. Phys. 29, (1978) 101.
8) S.C. Jardin, Phys. Fluids 21, (1978) 1851.
9) A.M.M. Todd, "Passive Stabilization in a Linear MHD Stability Code" Princeton Plasma Physics Laboratory Report, PPPL-1645 (1980).
10) J. Hugill and A. Gibson, Nucl. Fusion 14, (1974) 611.
11) E. Rebhan and A. Salat, Nucl. Fusion 18, (1978) 1431.
12) J.U. Blackbill, Methods in Computational Physics, (Academic Press, New York, 1976) Vol.16 P.1.
13) R. Gruber, J. Comp. Phys. 26, (1978) 999.

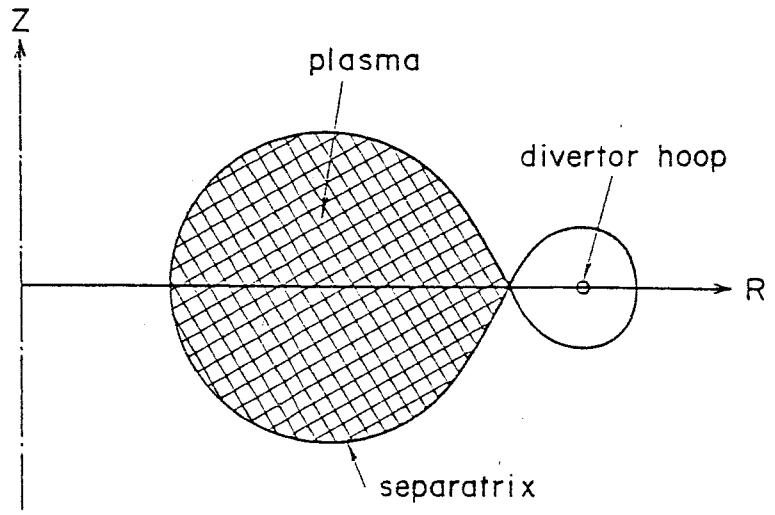

Fig. 3.1 Schematic diagram of a cross section of the JT-60 plasma. A divertor hoop is placed at the outer side of the torus to realize the poloidal magnetic limiter configuration.

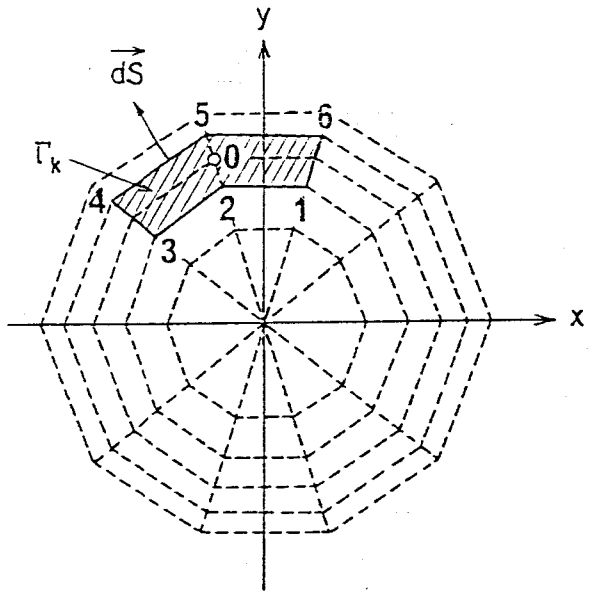

Fig. 3.2 Grid configuration in AEOLUS-P code for the analysis of the n=0 mode in a cylindrical plasma. All the physical quantities are integrated in the region Γ_k.

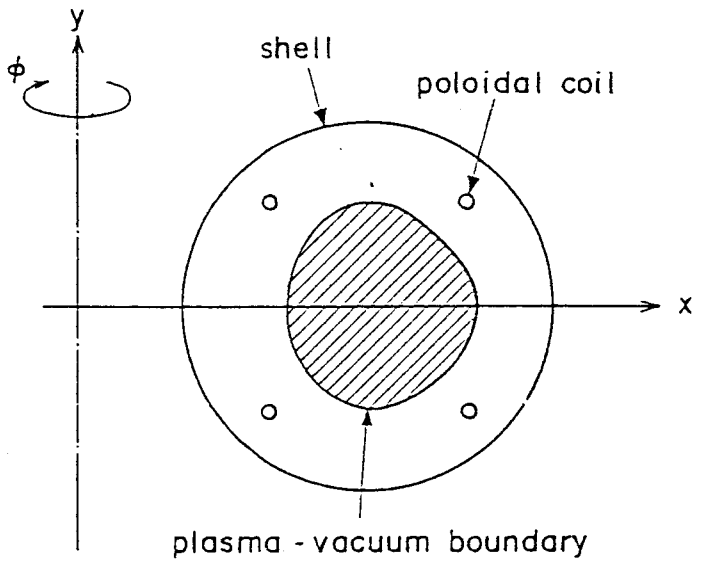

Fig. 3.3 Cross section of an axisymmetric toroidal system. The plasma-vacuum boundary is determined by the poloidal coils and the shell.

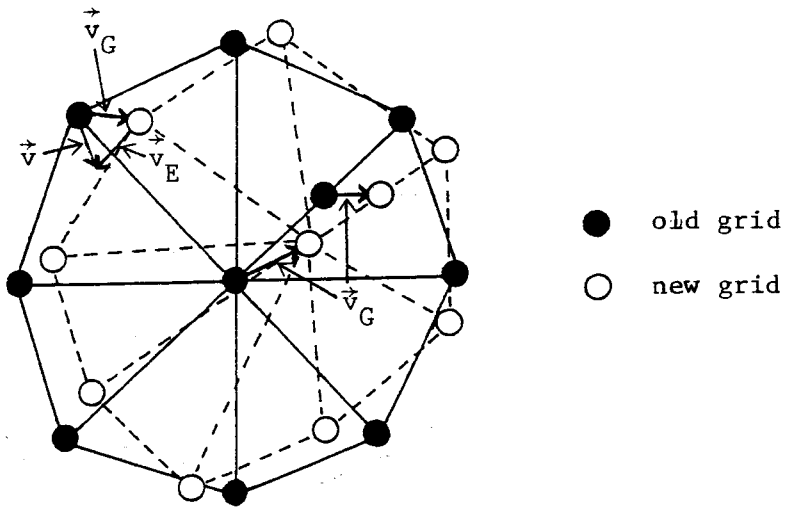

Fig. 3.4 Motion of grids by the rezoning process. The total velocity $\vec{v}$ of each grid is divided into the grid velocity $\vec{v}_G$ and the Euler velocity $\vec{v}_E$, except the center grid which is moved as a Lagrangian grid. The new grid configuration is determined so that all cells have the same area.

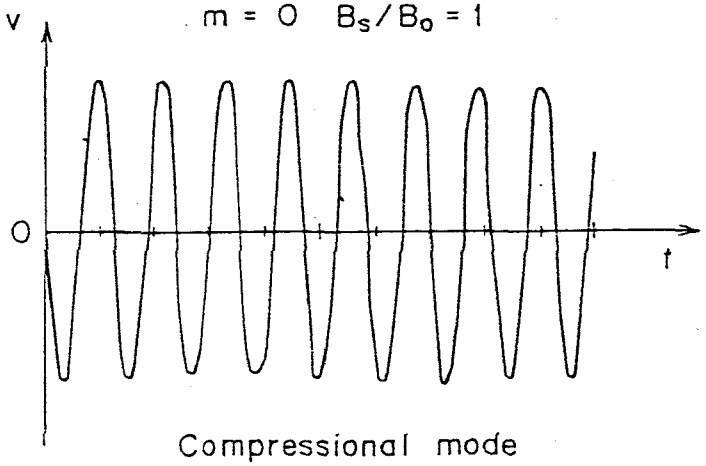

Fig. 3.5 Oscillation of the radial velocity at r=a/2 for the m=0 compressional mode in a fixed-boundary plasma with uniform mass and uniform current distributions (B_s/B_0=1.0).

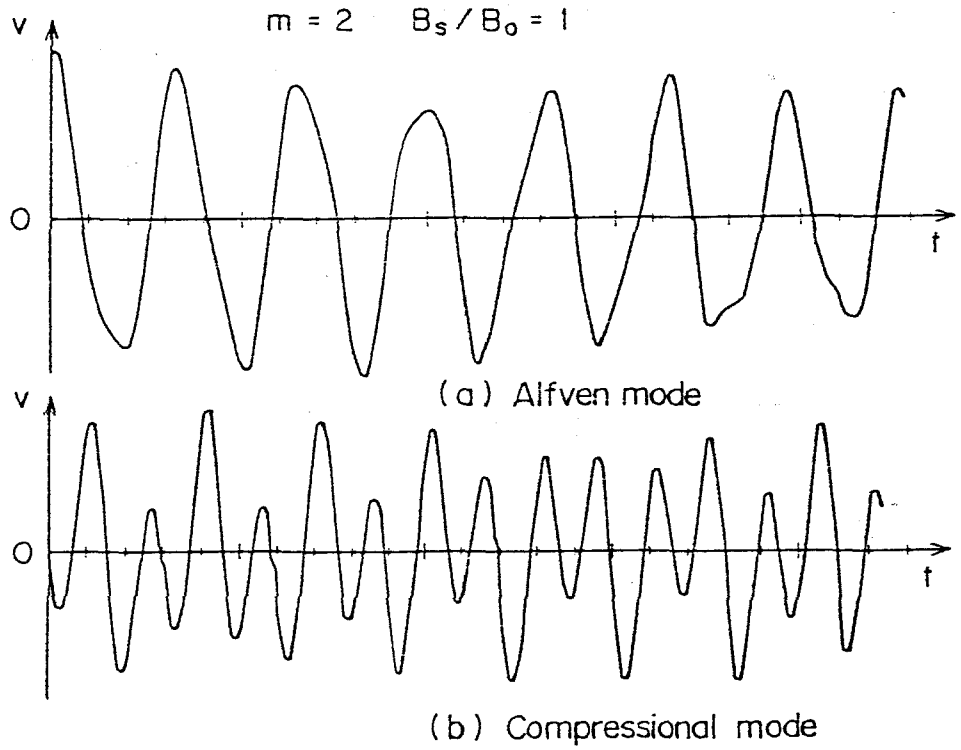

Fig. 3.6 Oscillations of the radial velocity at r=a/2 for (a) the m=2 Alfven mode and (b) the m=2 compressional mode.

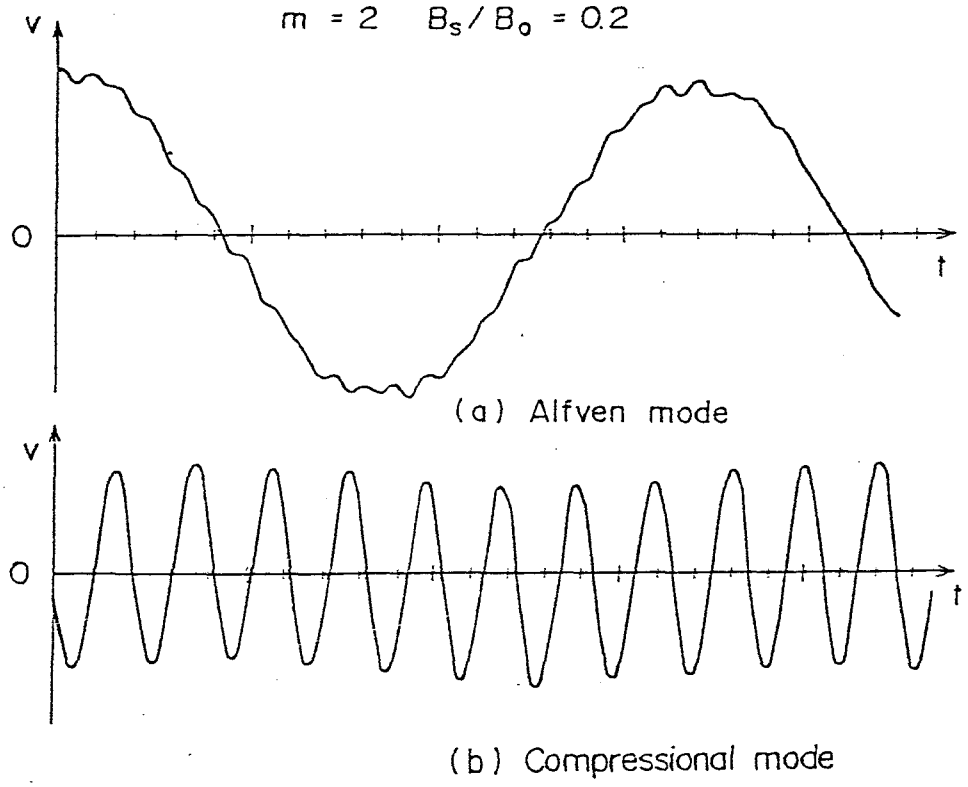

Fig. 3.7 Oscillations of the radial velocity at r=a/2 for (a) the m=2 Alfven mode and (b) the m=2 compressional mode. The poloidal field at the surface is chosen as $B_s/B_0 = 0.2$.

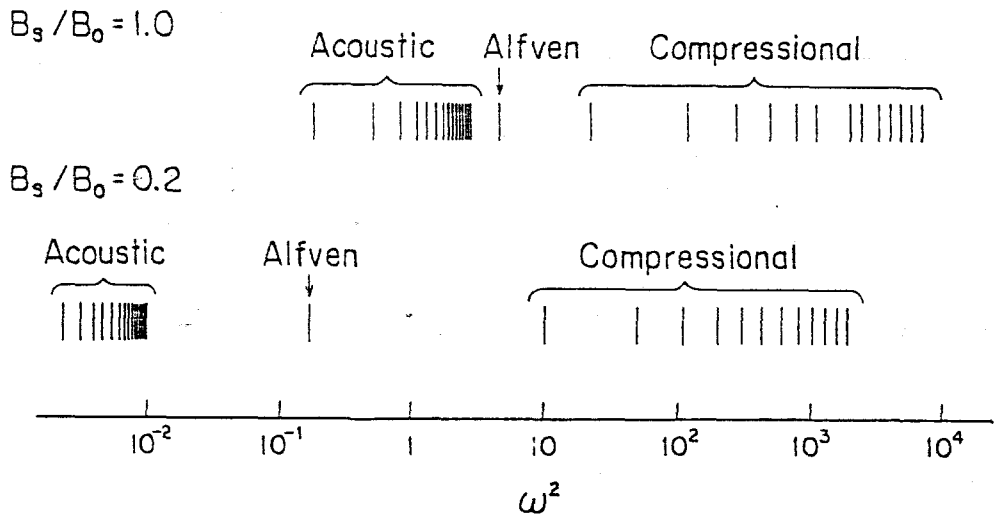

Fig. 3.8 Spectra of the m=2/n=0 fixed boundary modes for the cases of $B_s/B_0=1.0$ and $B_s/B_0=0.2$. These results are obtained by the 1D spectral code THALIA.

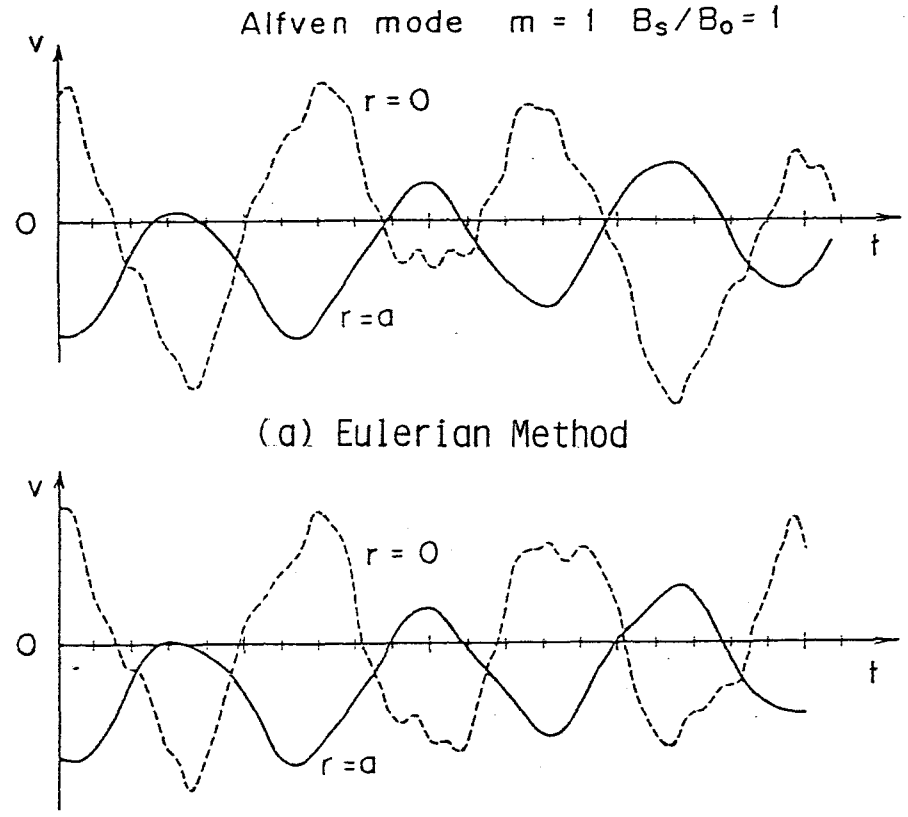

Fig. 3.9 Comparison of the result for the m=1 Alfven mode obtained by (a) the Eulerian method with that by (b) the dynamical grid method. The solid curve corresponds to the total velocity at the plasma surface and the broken one corresponds to the velocity of the center grid.

Table 3.1 Computed frequencies ω

m	B_s/B_0	mode	ω	
			AEOLUS-P	THALIA
0	1.0	Compressional	5.4	5.42 *
1	1.0	Alfven	0.97	1.00
2	1.0	Compressional	4.3	4.42
		Alfven	1.9	2.00
2	0.2	Compressional	3.1	3.09
		Alfven	0.37	0.40

* analytical result

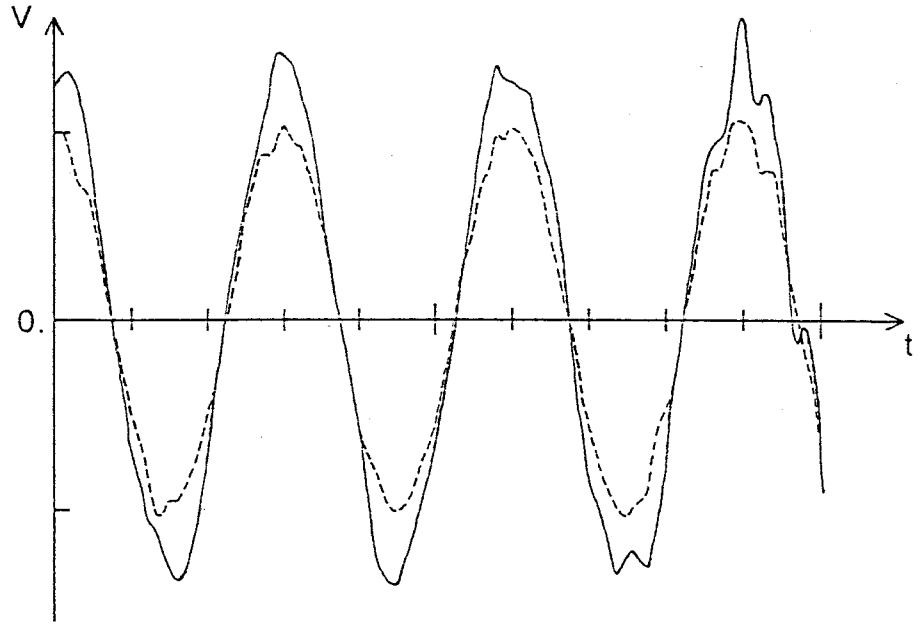

Fig. 3.10 Oscillations of radial velocity of m=0 Alfven mode for B_s/B_0=1.0. The shell is located at r=2a. The solid curve corresponds to the total velocity at the plasma surface and the broken one corresponds to the total velocity at r=a/2.

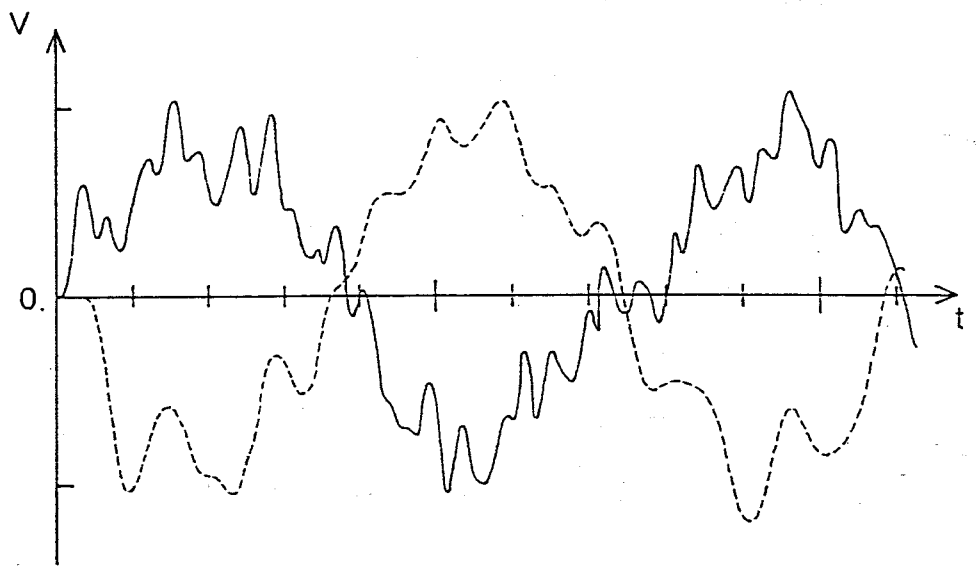

Fig. 3.11 Oscillations of radial velocity of m=1 Alfven mode for B_s/B_0=1.0. The shell is located at r=2a. The solid curve corresponds to the total velocity at r=a/2 and the broken one corresponds to the total velocity at r=0.

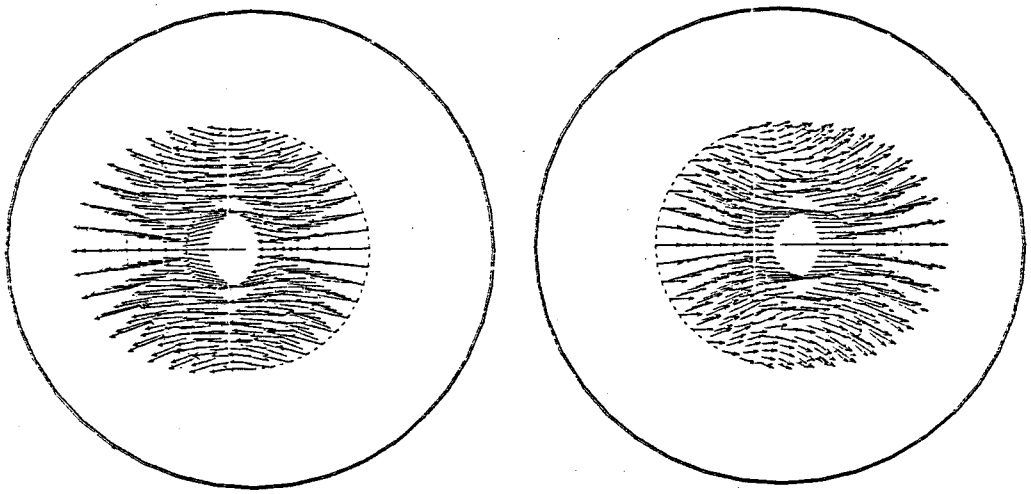

Fig. 3.12 Velocity vectors of m=1 Alfven mode in the case of free boundary at (a) t=2.5 and (b) t=5.5. The outer circles represent the shell.

Chapter IV

Analysis of Major Disruption Process in Tokamak

The major disruption of a tokamak in a cylindrical model is investigated by using a multi-helicity resistive MHD code. A possible mechanism of the instability due to the destabilization of the 3/2 mode by the mode coupling with the 2/1 mode is confirmed. The evolution of the magnetic field topology caused by the major disruption is studied in detail. The effect for the internal disruption on the 2/1 magnetic island width is also studied. The 2/1 magnetic island is not enhanced by the flattening of the q-profile due to the internal disruption.

4.1 Introduction

The major disruption of a tokamak is characterized by rapid release of magnetic and plasma energies within an order of μs followed by reduction of the plasma current with the decay time of several milliseconds, and it is considered to be the main cause of limitation of the plasma current and density. The disruption may bring about a more serious damage to the device as the device becomes larger. It is, therefore, urgently required to clarify the mechanism of the major disruption and to devise methods to control or suppress it.

It is considered that the m=2 tearing mode plays an important role in the major disruption. Experimentally, the growth of the m=2 magnetic field perturbation is observed as precursor of the disruption. When the safety factor at plasma boundary, q_a, is less than 2, the major disruption seems to be suppressed. Waddell et al. proposed that a nonlinear interaction between m/n=2/1 and m/n=3/2 tearing modes causes the major disruption[1~4]. The results of their simulation seem to well recover the experimental data. They presented the scaling law of the major disruption time on the basis of the WKB theory. The WKB method, however, is not always applicable to the nonlinear stage of the mode evolution. It is important to establish the theoretical model reliable in this stage. It is also very important to know the mechanism which makes the current profile unstable against the 2/1 mode and enlarge the 2/1 island width.

In this Chapter, we first recover the results of the ORNL group. We also investigate the initiation process of the 2/1 mode assuming that the current density profile is flattened by the 1/1 mode. The 2/1 island

obtained in the simulation is compared with those calculated by the Δ' code. In the next Section the basic equations of the present analysis are described. In Section 4.3, the results of simulation are presented. Conclusion and discussion are given in Section 4.4.

4.2 Basic Equations

The usual resistive MHD equations are

$$\begin{aligned}
&\frac{\partial \rho}{\partial t} + \vec{\nabla} \cdot (\rho \vec{v}) = 0 \quad , \\
&\rho \left[\frac{\partial \vec{v}}{\partial t} + (\vec{v}\cdot\vec{\nabla})\vec{v}\right] = -\vec{\nabla} p + \vec{J}\times\vec{B} \quad , \\
&\frac{\partial p}{\partial t} + \vec{v}\cdot\vec{\nabla} p + \gamma p \vec{\nabla}\cdot\vec{v} = 0 \quad , \\
&\frac{\partial \vec{B}}{\partial t} = \vec{\nabla} \times (\vec{v}\times\vec{B} - \eta\vec{J}) \quad , \\
&\vec{J} = \vec{\nabla} \times \vec{B} \quad , \\
&\vec{\nabla} \cdot \vec{B} = 0 \quad .
\end{aligned} \tag{4.1}$$

The characteristic time of this system of equations is determined by the compressional magnetosonic wave and the characteristic time scale of MHD phenomena of our interest is determined by the Alfven wave propagating along the magnetic field line. The ratio of these two time scales is about qA, where q and A denote the safety factor and aspect ratio, respectively. For a usual tokamak plasma the ratio is as large as 10, which makes it rather difficult to simulate the nonlinear MHD behavior on the basis of the above full set equations within a reasonable computational time. To overcome this difficulty, we reduce the full set of MHD equations (Eqs. (4.1)) to a set of simplified equations in which the compressional wave is removed analytically by introducing the incompressibility condition and the usual tokamak ordering. The reduced set of resistive MHD equations was first solved by Rosenbluth et al.[5] to analyze the nonlinear kink instability and, since then, many authors solved it numerically to analyze the nonlinear phenomena of internal kink mode[6] and resistive instabilities[1~4].

The reduced set of resistive MHD equations of a low β toroidal plasma in the cylindrical coordinate system (R,ϕ,z) is derived as following,

$$\frac{\partial \Psi}{\partial t} + \vec{v}\cdot\vec{\nabla}_{\perp}\Psi = B_0\frac{\partial \Phi}{\partial \zeta} + \eta J - E_w(t) \quad ,$$

$$\frac{\partial U}{\partial t} + \vec{v}\cdot\vec{\nabla}_{\perp}U = \vec{\nabla}\zeta\cdot\vec{\nabla}P\times\vec{\nabla}_{\perp}\left(\frac{R}{R_0}\right)^2 + \left(\frac{R}{R_0}\right)^2\vec{\nabla}\zeta\cdot\vec{\nabla}_{\perp}\Psi\times\vec{\nabla}_{\perp}J + B_0\frac{\partial J}{\partial \zeta} \quad ,$$

$$\frac{\partial P^*}{\partial t} + \vec{v}\cdot\vec{\nabla}_{\perp}P^* = 0 \quad ,$$

$$\vec{B} = B_0\vec{\nabla}\zeta + \vec{\nabla}\zeta\times\vec{\nabla}_{\perp}\Psi \quad , \qquad (4.2)$$

$$\vec{v} = \left(\frac{R}{R_0}\right)^2\vec{\nabla}\zeta\times\vec{\nabla}_{\perp}\Phi \quad ,$$

$$\vec{J} = \left(R^2\vec{\nabla}_{\perp}\cdot\frac{\vec{\nabla}_{\perp}\Psi}{R^2}\right)\vec{\nabla}\zeta \quad ,$$

$$U = \left(\frac{R}{R_0}\right)^2\vec{\nabla}_{\perp}^2\Phi \quad ,$$

$$P^* = \left(\frac{R}{R_0}\right)^{2\gamma}P \quad ,$$

where R_0 is the major radius, $\zeta=R_0\phi$, $\vec{\nabla}_{\perp}\equiv\frac{\partial}{\partial R}\vec{\nabla}R + \frac{\partial}{\partial z}\vec{\nabla}z$. The quantities U, Ψ and Φ denote the vorticity, poloidal flux and stream function, respectively. The detailed derivations of this reduced set of equations are given in the Appendix of Ref.7.

The energy integral of this reduced set of equations is given by

$$\frac{d}{dt}\int d\tau\left[\left(\frac{R}{R_0}\right)^2|\vec{\nabla}\Phi|^2 + \left(\frac{R_0}{R}\right)^2|\vec{\nabla}\Psi|^2 + \frac{P}{\gamma-1}\right]$$

$$= -\int d\tau\left[\left(\frac{R_0}{R}\right)^2\eta J^2\right] + 2\pi R_0 E_w(t) I_P \quad . \qquad (4.3)$$

The first term in the l.h.s. represents the kinetic energy, the second one the magnetic energy, and the third one the internal energy. The first term in the r.h.s. is the energy dissipation. The electric field at the wall, $E_w(t)$, is obtained from Eq.(4.3) by setting the total plasma current I_P constant.

Now we employ the coordinate system (r,θ,ζ), in which the magnetic lines are straight. The radial coordinate r is defined by

$$r = \left(\frac{R_0}{R}\right)^2\sqrt{g} \quad , \qquad (4.4)$$

where $\sqrt{g}$ is Jacobian. The variables Ψ, J, Φ and P^* are Fourier expanded in θ and ζ directions:

$$\Psi(r,\theta,\zeta) = \sum_{m,n} \Psi_{m/n}(r) \exp i(m\theta - \frac{n}{R_0}\zeta) \quad , \tag{4.5}$$

where m and n denote the mode numbers in θ and ζ directions, respectively. The Fourier expanded equations are written as follows;

$$\frac{\partial \Psi_{m/n}}{\partial t} = [\Psi,\Phi]_{m/n} + \frac{B_0}{R_0} n\Phi_{m/n} + \eta J_{m/n} - E_{m/n} \quad , \tag{4.6}$$

$$\frac{\partial U_{m/n}}{\partial t} = [U,\Phi]_{m/n} + [J,\Psi]_{m/n} - \frac{B_0}{R_0} nJ_{m/n} + [F,P]_{m/n} \quad , \tag{4.7}$$

$$\frac{\partial P^*_{m/n}}{\partial t} = [P^*,\Phi]_{m/n} \quad , \tag{4.8}$$

where $[\Psi,\Phi]_{m/n}$ is defined by

$$[\Psi,\Phi]_{m/n} = \sum_{\substack{m=m'+m'' \\ n=n'+n''}} \frac{m'}{r} (\Psi_{m'/n'} \frac{d}{dr} \Phi_{m''/n''} - \Phi_{m'/n'} \frac{d}{dr} \Psi_{m''/n''}) \quad . \tag{4.9}$$

Variables $J_{m/n}$ and $U_{m/n}$ take the form;

$$J_{m/n} = \frac{1}{r} \sum_{m=m'+m''} [\frac{d}{dr} (G^{rr}_{m'} \frac{d}{dr} \Psi_{m''/n}) - m'' \frac{d}{dr}(G^{r\theta}_{m'} \Psi_{m''/n}) - m G^{r\theta}_{m'} \frac{d}{dr} \Psi_{m''/n} - m m'' G^{\theta\theta}_{m'} \Psi_{m''/n}] \quad , \tag{4.10}$$

$$U_{m/n} = \frac{1}{r} \sum_{m=m'+m''} [\frac{d}{dr}(H^{rr}_{m'} \frac{d}{dr} \Phi_{m''/n}) - m'' \frac{d}{dr}(H^{r\theta}_{m'} \Phi_{m''/n}) - m H^{r\theta}_{m'} \frac{d}{dt} \Phi_{m''/n} - m m'' H^{\theta\theta}_{m'} \Phi_{m''/n}] \quad . \tag{4.11}$$

Quantities F_m, G^{ij}_m and H^{ij}_m are defined by

$$(\frac{R}{R_0})^2 = \sum_m F_m(r) \exp im\theta \quad , \tag{4.12}$$

$$r\, g^{ij} = \sum_m G^{ij}_m(r) \exp im\theta \quad , \tag{4.13}$$

$$r\, (\frac{R}{R_0})^2 g^{ij} = \sum_m H^{ij}_m(r) \exp im\theta \quad . \tag{4.14}$$

In the following calculation Eq.(4.8) for pressure perturbation is neglected because the pressure driven mode is not important in a low β plasma. Moreover we neglect the toroidal effects. Even by this simplification, the essential mechanism of the major disruption can be described. We assume the resistivity is constant in time and set it to be

$$\eta(r) = E_w(t=0)/J(r,t=0) \quad . \tag{4.15}$$

The multi-helicity calculation is carried out with up to 29 Fourier components and 201 equal-spacing radial meshes. The equations are solved by both the full-explicit and implicit-explicit predictor-corrector time integration schemes, and a good agreement between both cases is obtained. The time step for the former scheme, however, is restricted to be much small in comparison with that for the latter scheme.

4.3 Computational Results

(1) Nonlinear Destabilization of 3/2 Mode

We choose the q-profile as in Ref.1, $q(r)=1.38[1+(r/0.6)^8]^{1/4}$ and the magnetic Reynolds number $S=2\times10^4$ at q=2 surface. Almost the same behavior of the plasma as that of the ORNL calculation is recovered, which is presented in Figs.4.1-4.7. Figure 4.1 (a and b) show the time evolution of magnetic island width obtained by the single-helicity and multi-helicity calculations, respectively. The single helicity calculation shows that the 2/1 and 3/2 modes are both unstable and the widths of the saturated islands are about 0.4 and 0.1, respectively. In contrast with the single-helicity calculation, the multi-helicity calculation shows the rapid destabilization of 3/2 mode after the islands of the 2/1 and 3/2 modes touch each other at $t \simeq 300$, due to the nonlinear interaction between modes with different helicities.
The phase of the 5/3 and 7/4 modes are inverted several times at final stage of the disruption. The evolution of the kinetic and magnetic energies are shown in Fig.4.2 (a and b), respectively. Both the energies rapidly increase from the island-overlapping time ($t \simeq 300$). The time evolution of the growth rate of the magnetic energy is shown in Fig.4.3. The growth rate of the 2/1 mode is slowly decreasing function of time when the growth rates of the 3/2 and 5/3 modes begin to increase, which

means that 2/1 mode is in the Rutherford regime even after the time of the island overlapping. Figure 4.4 shows the time evolution of the one turn voltage, $V=[\frac{d}{dt}(E_k + E_M) - Q]/I_p$, where I_p is total plasma current, E_k and E_M are the kinetic and magnetic energies, and Q is the change in the rate of energy dissipation due to Joule heating. In this figure, V is normalized by ηB_t. The negative voltage spike is observed is the figure. The order of magnitude of the voltage spike is in good agreement with experimental value. The helical flux contours for several modes with different helicities at the end of the calculation are shown in Fig.4.5. The magnetic islands of the higher harmonics, such as the 8/5 or 13/7 modes, have also fairly large amplitude. In Fig.4.6, intersections of a single magnetic field line near the separatrix of the 2/1 island at the $\zeta=0$ poloidal plane are plotted. This figure shows that the stochastic region develops during the interval ($t=300 \sim 400$) and covers almost the plasma column at the final stage. The stochasticity can be investigated quantitatively by calculating the K-S entropy[8], which is shown in Fig.4.7. The evolution of the K-S entropy confirms the above result. The stochastic magnetic field in the plasma column enhances the heat loss and causes the rapid cooling of the plasma, which is observed in the soft X ray signals from the plasma center.

(2) Effect of Internal Disruption

Next, we calculate the nonlinear evolution of the 2/1 tearing mode in the presence of the 1/1 mode. The purpose of this calculation is to simulate destabilization of the 2/1 mode by the internal disruption through the flattening of the q-profile inside of the q=1 surface. The initial q-profile in this case is $q(r)=0.9[1+(4/0.5)^{2\lambda}]^{1\lambda}$, where $\lambda=2+2r^2$, and $S=2\times10^4$ at the q=1 surface (solid line in Fig.4.8). In this profile the islands of the 2/1 and 3/2 modes are saturated at relatively narrow width. The saturation width of the 2/1 and 3/2 islands ($W_{2/1}$ and $W_{3/2}$) estimated by using a Δ' code is $W_{2/1}=0.109$ and $W_{3/2}=0.005$ for the initial q-profile, and $W_{2/1}=0.204$, $W_{3/2}=0.062$ for the flattened q-profile (dashed line in Fig.4.8), respectively. There is no island overlapping between the 2/1 and 3/2 modes for the initial q-profile, while the island overlapping is expected for the flattened q-profile after the internal disruption. In order to investigate this possible enhancement of the 2/1 island width by the flattening of the current profile due to the

internal disruption, the calculation is started with only the 2/1 mode, and the 1/1 mode is initiated at t=520 after the 2/1 island is saturated (Fig.4.9). The saturation width of the 2/1 island at t=520 is $W_{2/1}$=0.07 which is a little smaller than the expected value. With the growth of the 1/1 mode, the 3/2 mode is produced by the coupling of the 1/1 and 2/1 modes, and the internal disruption occurs at t≅700. After the internal disruption the q-profile inside of the q=1 surface is flattened and that outside of it is unchanged, (dotted line in Fig.4.8). In spite of the change of the q-profile, however, the island evolution of the 2/1 and 3/2 modes seems unchanged, even a long while after the internal disruption, i.e., $W_{2/1}$=0.07 and $W_{3/2}$=0.014 at t=970. These values are about 1/3-1/4 of those obtained by using the Δ' code and there is no indication of island overlapping even if the calculation continues. There are other possibilities to initiate the major disruption. In Ref.9, we have shown that the size of the 2/1 island is strongly enhanced by the internal disruption due to the toroidal coupling. This result suggests that in a toroidal plasma the major disruption is induced indirectly by the change of the current profile due to the internal disruption. This problem is discussed in more detail in the next Chapter.

4.4 Conclusion and Discussion

We have studied the nonlinear evolution of tearing modes with different helicity in a cylindrical plasma and confirmed the possibility that the major disruption is caused by the nonlinear destabilization of the 3/2 mode through the mode coupling with the 2/1 mode. And the evolution of the magnetic field topology has been minutely investigated. All these results support the mechanism of the major disruption, proposed by Waddell et al.. The details of our results, however, are different from their results. Especially, in our simulation, the 2/1 mode is deeply in the Rutherfored regime and its instantaneous growth rate is not affected even after the 3/2 mode is nonlinearly destabilized. This behavior of the 2/1 mode contradicts with the WKB theory. Therefore, the mechanism of the destabilization of the 3/2 mode remains unsolved.

As for the effect of the internal mode on the major disruption, the flattening of the q-profile due to the internal disruption did not cause the enhancement of the 2/1 island width, in spite of the prediction of

the major disruption by the Δ' calculation. The flattening occurs only inside of the q=1 surface and the q-profile is not affected near the 2/1 and 3/2 surfaces. Therefore, in order to expect the major disruption by the internal disruption, we have to take into account other effects, such as the toroidicity.

References

1) B.V. Waddell, B. Carreras, H.R. Hicks, J.A. Holmes and D.K. Lee, Phys. Rev. Lett. 41, (1978) 1368.
2) B.V. Waddell, B. Carreras, H.R. Hicks and J.A. Holmes, Phys. Fluids 22, (1979) 896.
3) B. Carreras, H.R. Hicks, J.A. Holmes and B.V. Waddell, Phys. Fluids 23, (1980) 1181.
4) B. Carreras, H.R. Hicks and D.K. Lee, Phys. Fluids 24, (1981) 66.
5) M.N. Rosenbluth, D.A. Monticello, H.R. Strauss and R.B. White, Phys. Fluids 19, (1976) 1987.
6) H.R. Strauss, Phys. Fluids 19, (1976) 134.
7) Y. Tanaka, M. Azumi, T. Tsunematsu and T. Takeda, "High-Speed Numerical Code "AEOLUS-R1" for Resistive MHD Instability with Single Helicity", Japan Atomic Energy Research Institute Report JAERI-M 8656 (1980). (in Japanese)
8) B.V. Chirikov, Phys. Reports 52, (1979) 263.
9) M. Azumi, S. Tokuda, G. Kurita, T. Tsunematsu, T. Takizuka, T. Tuda, K. Itoh, Y. Tanaka and T. Takeda, "Internal Disruption in High β_p Tokamak", Japan Atomic Energy Research Institute Report JAERI-M 9787 (1981).

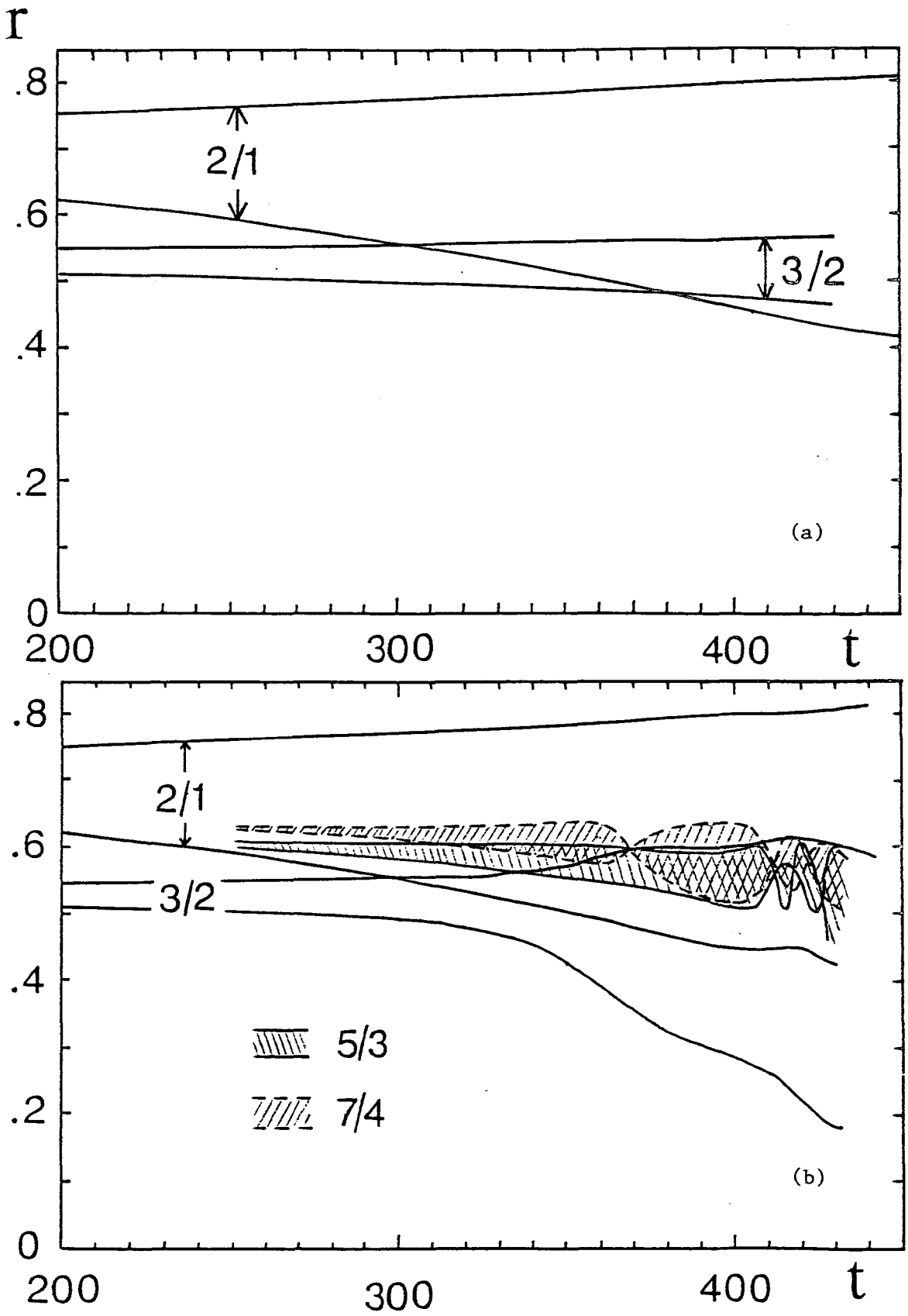

Fig.4.1 Time evolution of the m/n mode magnetic island width for the case of (a) single-helicity calculation and (b) multi-helicity calculation. The widths for both cases are the same before the island-overlapping time (t = 300).

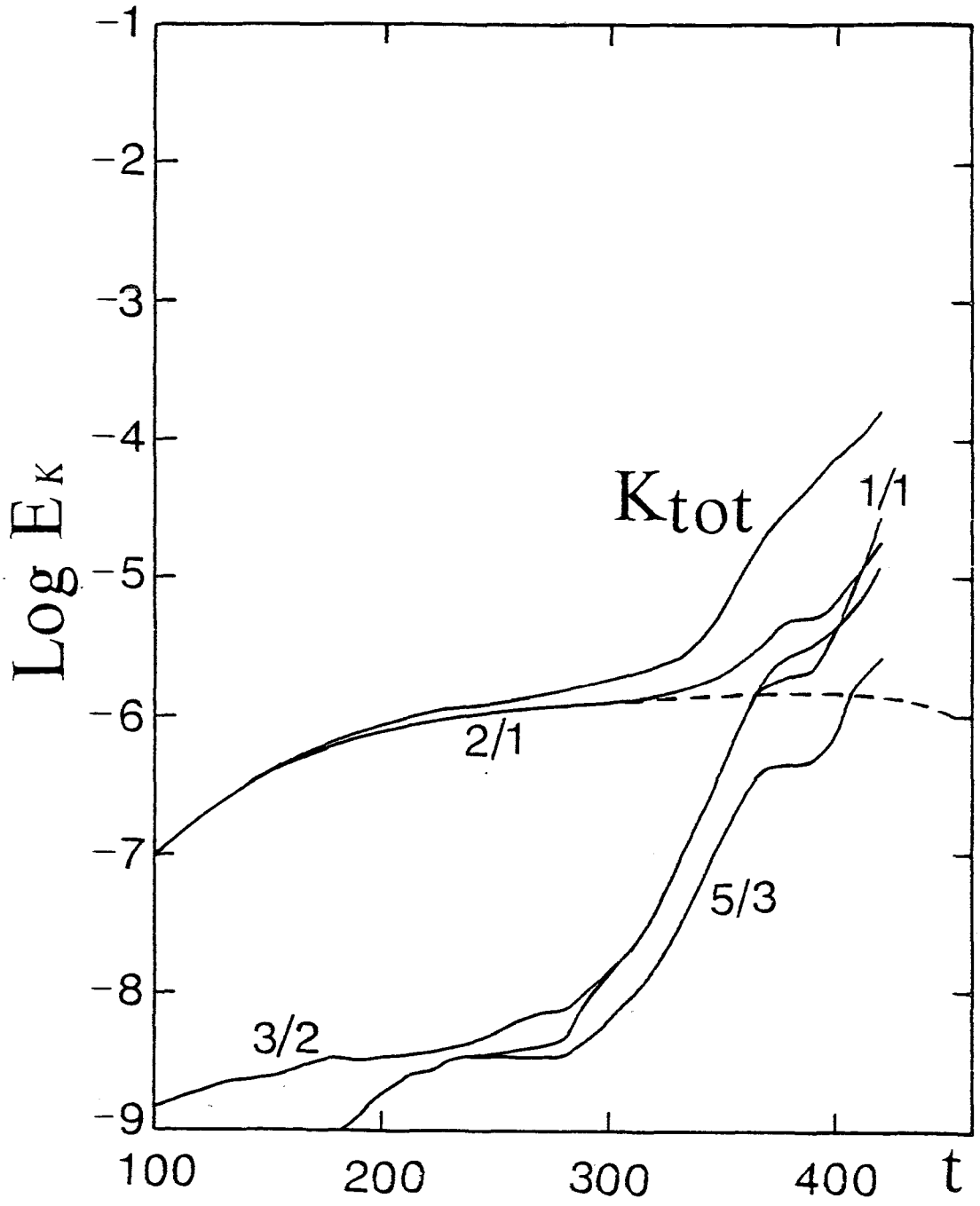

Fig.4.2 (a) Time evolution of the kinetic energy in the case of multi-helicity calculation. Results for the single-helicity calculation is shown by the dotted line.

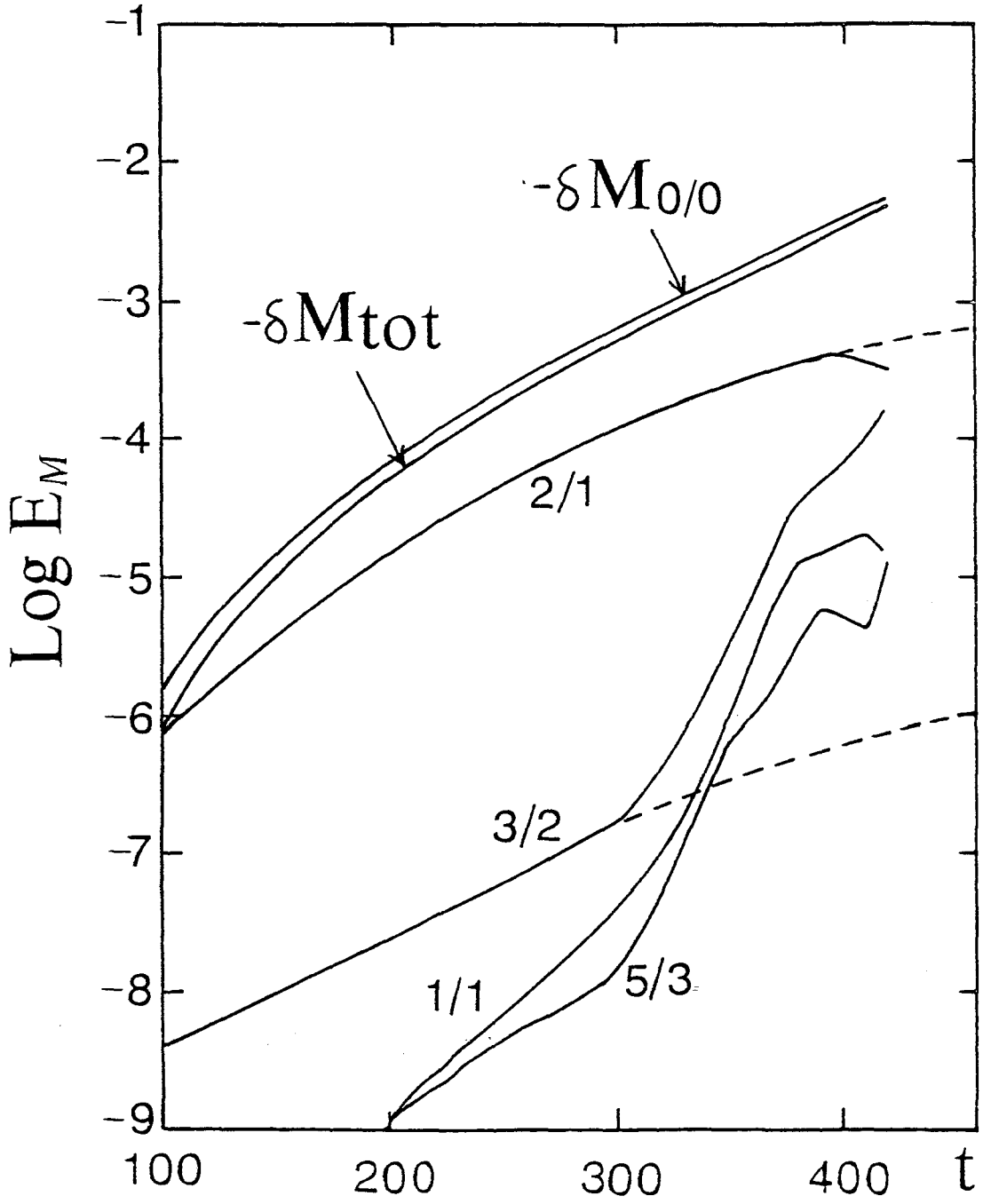

Fig.4.2 (b) Time evolution of the magnetic energy in the case of multi-helicity calculation. Results for the single-helicity calculation is shown by the dotted line.

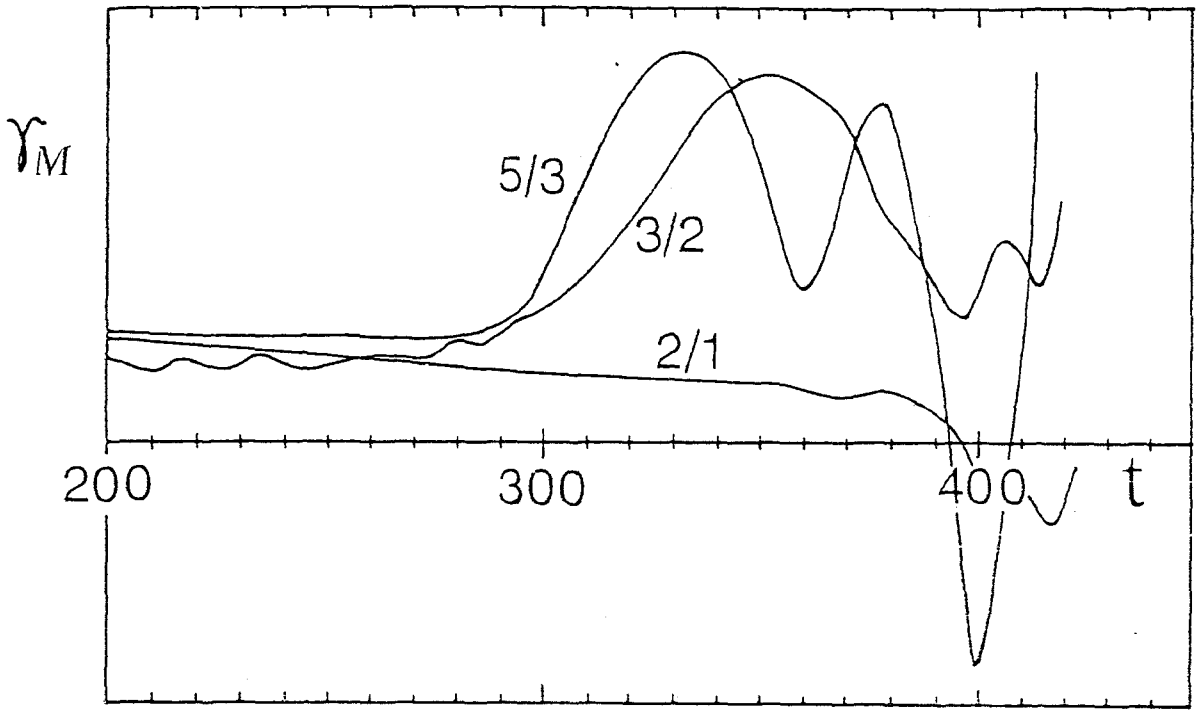

Fig.4.3 Instantaneous growth rates of the m/n magnetic energy. The growth rates of the 3/2 and 5/3 modes start to increase at the island-overlapping time (t = 300), while the 2/1 mode remains in the Rutherford regime.

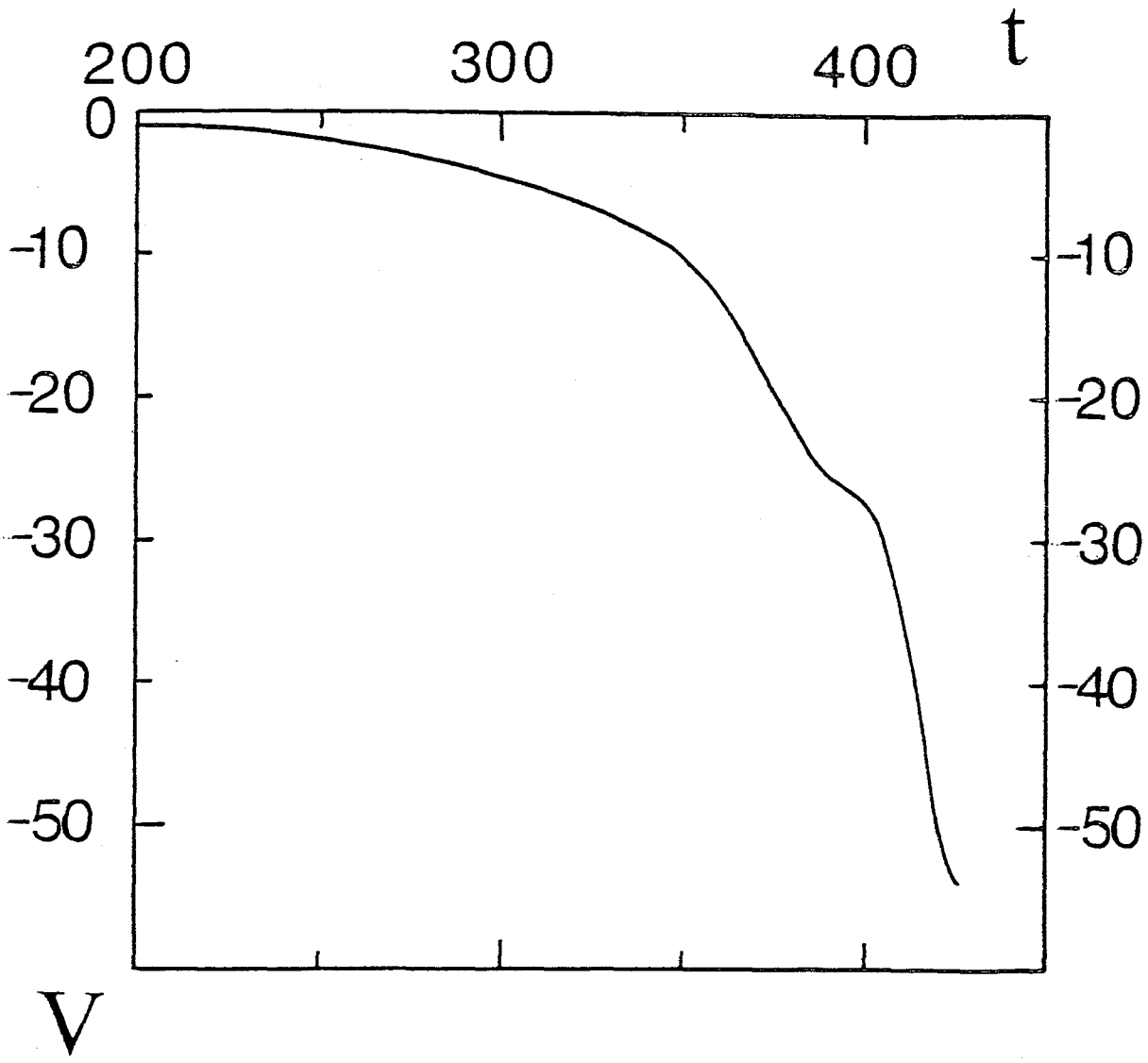

Fig.4.4 Time evolution of the one-turn voltage at the limiter.

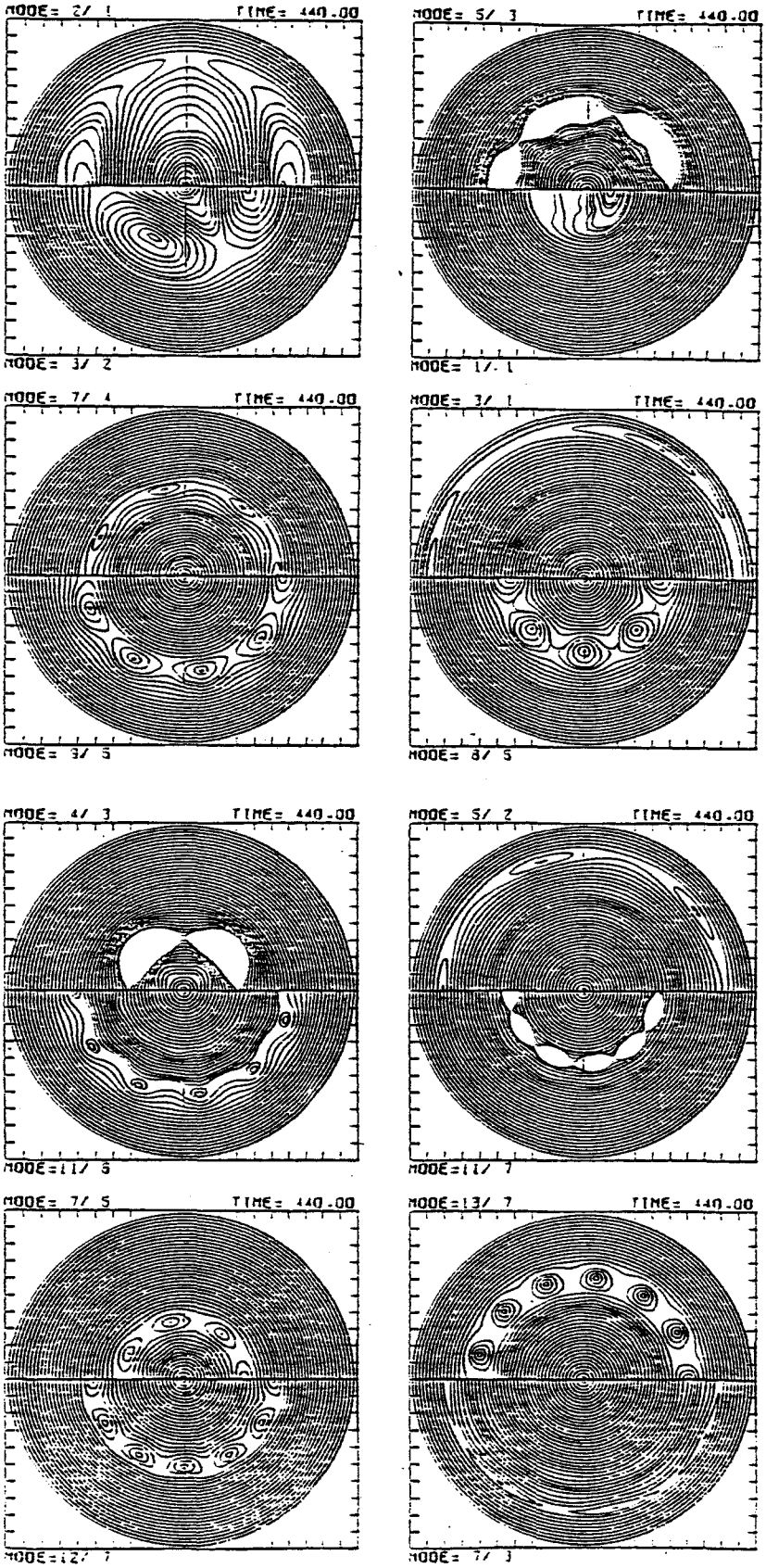

Fig.4.5 Helical flux contours of different helicities at the end of the calculation, t = 440.

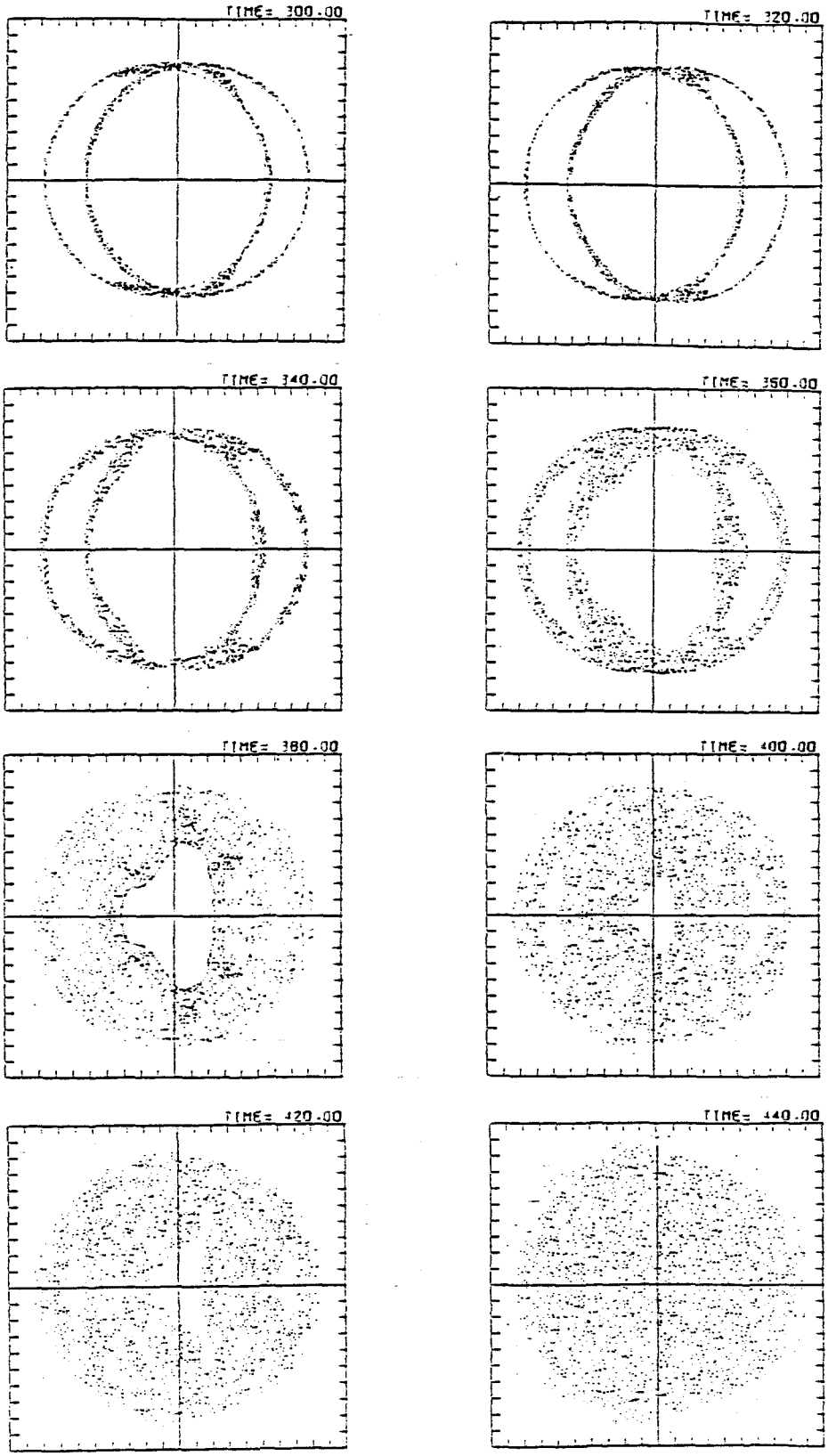

Fig.4.6 Trajectory of a magnetic field line, starting from a point on the separatrix of the 2/1 island. The cross-section at the poloidal plane $\zeta=0$ is shown. Distinct structure of the 2/1 island is seen at the island-overlapping time $t = 300$, while the trajectory is almost stochastic at $t = 440$.

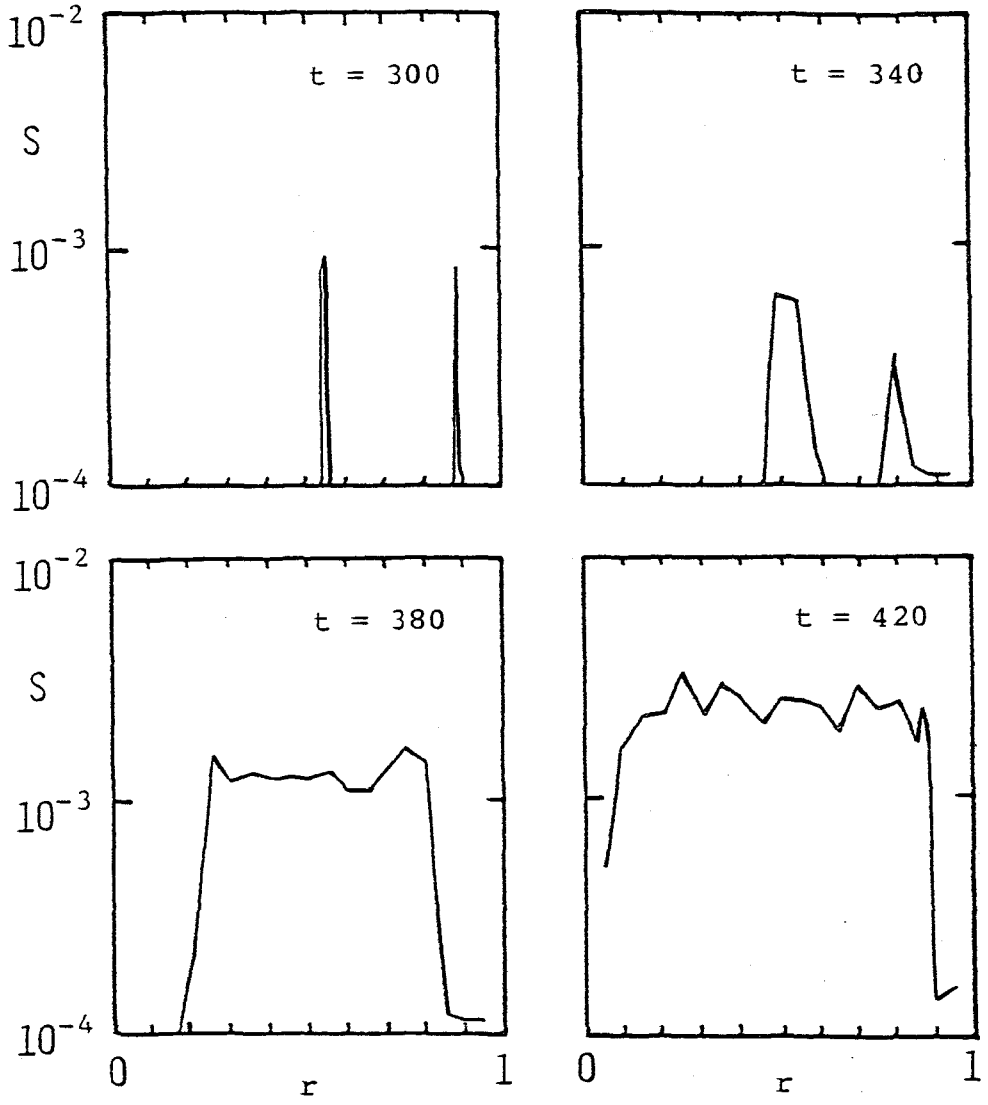

Fig.4.7 Space distribution of the K-S entropy of a magnetic field line at t = 300, 340, 380 and 420. The K-S entropy is defined by

$$S = \lim_{N=\infty} \frac{1}{N} \sum_{n}^{N} \ln \ell_n$$

where n stands for an iteration serial number and ℓ_n is the distance between two field lines starting from neighbouring positions.

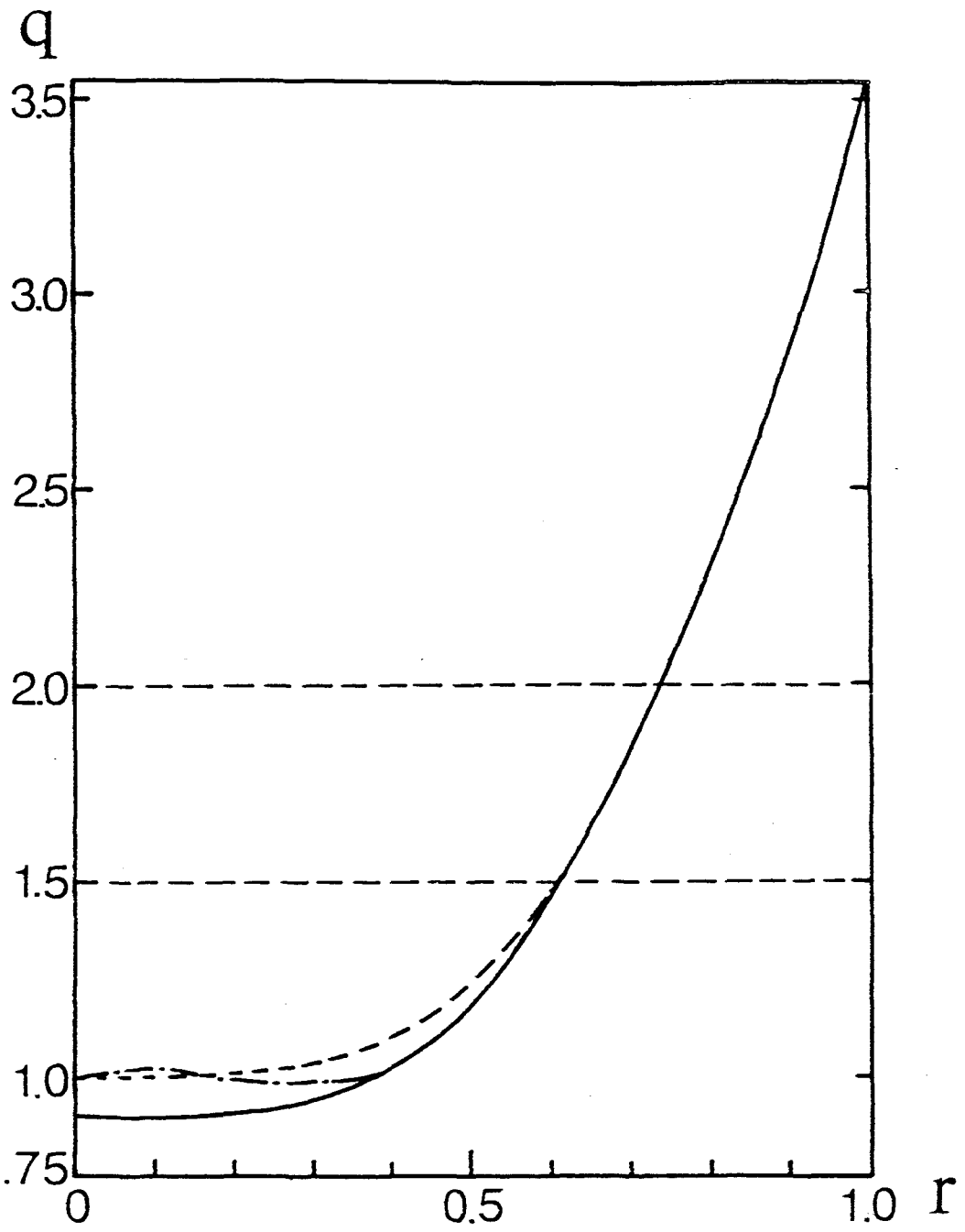

Fig.4.8 Profile of the safety factor q. The solid line denotes the initial q-profile (q_0=0.9 and q_a=3.6). The dotted line is the q-profile changed by the internal disruption. The model q-profile after the internal disruption for the Δ' calculation is shown by the dashed line.

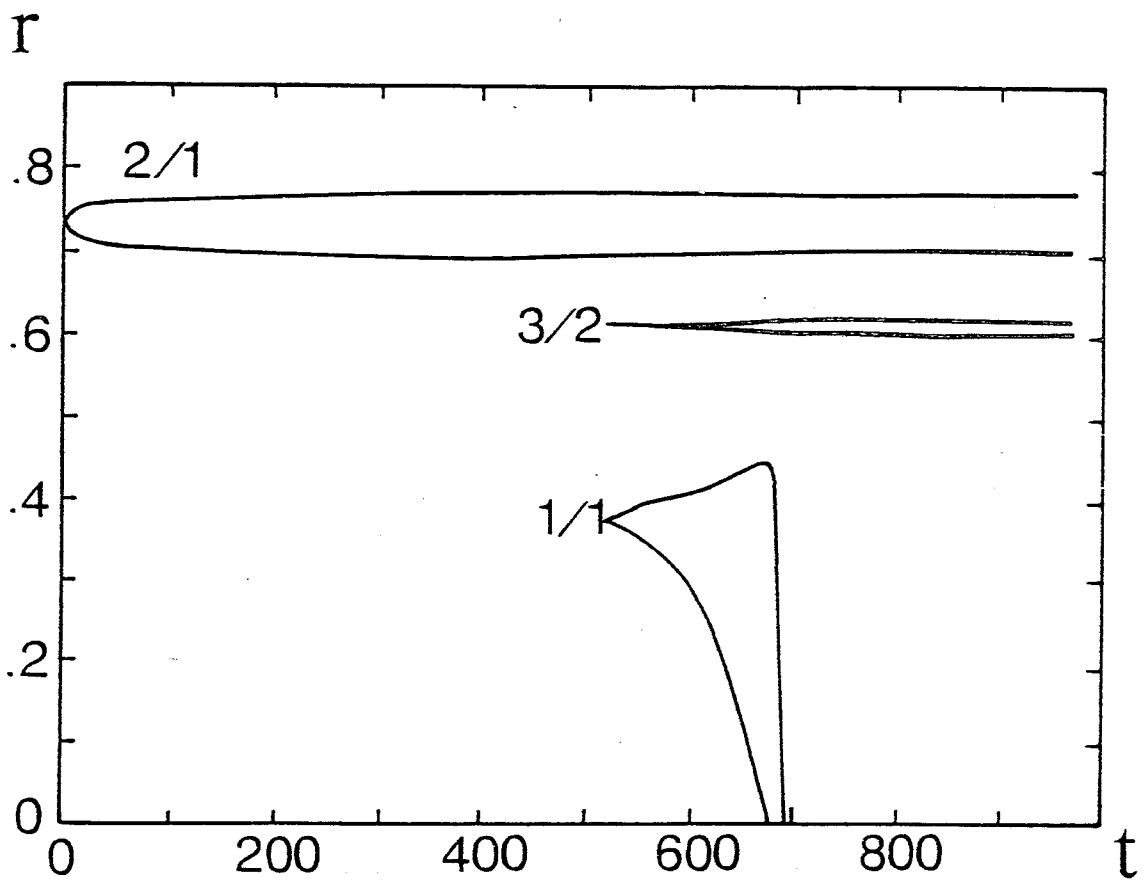

Fig.4.9 Time evolution of the magnetic island width. The result from t = 0 to t = 520 is obtained by the single-helicity calculation of the 2/1 mode. The 1/1 perturbation is added at t = 520, and the evolution is simulated by the multi-helicity code. The internal disruption, which occurs at t = 690, does not influence the 2/1 mode.

Chapter V

Numerical Study of Toroidal Effect on Low-m Resistive Modes

Effects of the toroidicity and finite pressure on low-m ideal and resistive modes are studied numerically on the basis of the reduced set of the MHD equations. Both the linear and nonlinear analyses show that the m=2 mode is strongly destabilized by the above effects. Especially, in a highly resistive plasma with large $\varepsilon\beta_p$, the amplitude of the m=2 and m=3 perturbations are comparable with or larger than that of m=1 perturbation. In spite of this large modification of the modes in the linear phase, the nonlinear evolution of the m=1 mode is essentially the same as in the cylindrical geometry. During the evolution, the toroidicity enhances magnetic islands of m=2 mode and other resonant modes and wide stochastic region is formed in a plasma. The destabilization of the m=2 mode, however, is not directly related to the major disruptions. It is conjectured that the destabilized m=2 mode may change the equilibrium to the one unstable against the major disruption.

5.1 Introduction

As described in the previous Chapter clarification of a mechanism of disruptive instabilities and establishment of controlling or suppressing means are very important problem to be solved urgently in the field of the tokamak research. Internal disruptions, i.e., sawtooth oscillations observed in soft X ray signals and major disruptions are extensively analyzed by many authors on the basis of the reduced set of the resistive MHD equations[1~9]. These analyses have been carried out to investigate behaviours of a rather low beta ohmically heated tokamak plasma and finite poloidal beta effects have not been taken into account. In recent tokamak experiments, however, higher poloidal beta values are realized by an intense additional heating. With increasing poloidal beta value there observed a new phenomenon, i.e., disappearance of the internal disruption and appearance of large amplitude continuous oscillations[10]. The change of the stability property suggests the importance of the finite poloidal beta effect on the disruption process and, for clarification of the disruption mechanism, it seems very important to take into account of the finite poloidal beta effect.

The purpose of this Chapter is to investigate the toroidal coupling of resistive modes enhanced by the effect of the poloidal beta in a tokamak plasma and to get some insights into the driving mechanisms of the disruptive instabilities. Analyses are carried out on the basis of the reduced set of the resistive MHD equations described in the previous Chapter. In Section 5.2 equilibrium used for the calculation and numerical procedure are explained. In Section 5.3 we study the linear stability property minutely with various parameters for the fixed profile of the safety factor. The results of nonlinear calculations with the finite poloidal beta value are given in Section 5.4. Section 5.5 is devoted for conclusions and discussion.

5.2 Equilibrium

In this Section we present an equilibrium used for subsequent stability analyses. A low β tokamak plasma with a circular cross section and large aspect ratio is considered. We employ a coordinate system (r,θ,ϕ), where magnetic field lines are straight and the radial coordinate is defined as $r = \sqrt{g}\ (R_0/R)^2$. In the coordinate system the mapping functions $X(r,\theta)$ and $Z(r,\theta)$ for the equilibrium solution are derived up to the order of ε^2 as

$$\begin{aligned} X(r,\theta) &= R_0 - \varepsilon r\cos\theta - \varepsilon^2\Delta(r) \quad , \\ Z(r,\theta) &= \varepsilon r\sin\theta \quad , \end{aligned} \tag{5.1}$$

where $\Delta(r)$ is the shift of the magnetic surface and given by the following equation,

$$\Delta(r) = \frac{1}{R_0}\int_r^a \frac{dr}{rB_\theta^2}\int_0^r \left(B_\theta^2 - 2r\frac{dP}{dr}\right) rdr \quad . \tag{5.2}$$

For the above equilibrium we obtain the following expressions of the reciprocal metric tensor, assuming that the inverse aspect ratio $\varepsilon(= r/R_0)$ is sufficiently small,

$$g^{rr} = 1 + 2\frac{d\Delta}{dr}\cos\theta \quad ,$$

$$g^{r\theta} = -\left(\frac{d^2\Delta}{dr^2} + \frac{1}{r}\frac{d\Delta}{dr} - \frac{1}{R_0} \right) \sin\theta \quad ,$$

$$g^{\theta\theta} = \frac{1}{r^2}\left\{ 1 - 2\left(\frac{d\Delta}{dr} - \frac{r}{R_0} \right) \cos\theta \right\} \quad , \qquad (5.3)$$

$$g^{\phi\phi} = R_0^2 \left(1 + 2\frac{r}{R_0}\cos\theta\right) .$$

In the following stability analyses we substitute concrete forms of the profiles of pressure $P(r)$ and safety factor $q(r)$ into the equation of $\Delta(r)$, and calculate the metric tensor.

5.3 Linear Stability Analysis by Reduced Set of Equations

Before studying the nonlinear MHD behaviours in the next Section, we investigate the linear stability of the current- and pressure-driven modes in detail on the basis of the reduced set of equations described in Section 4.2. We linearize the equations with respect to Ψ and Φ. Our main concern is the analysis of the n=1 mode which tends to an m/n = 1/1 mode in a cylindrical plasma. Variable parameters in the analyses are the inverse aspect ratio $\varepsilon(= a/R_0)$, poloidal beta β_p, and magnetic Reynolds number $S(= \tau_r/\tau_{pa})$, where a, R_0, τ_r, and τ_{pa} are the minor and major radii of the plasma, resistive diffusion time, and poloidal Alfven time, respectively. The magnetic Reynolds number is measured at the m=1 singular surface and the poloidal beta is defined as $\beta_p = 2\langle P(r)\rangle/B_a^2$, where $\langle\ \rangle$ denotes the average with respect to r, $P(r)$ and B_a are the pressure function and poloidal magnetic field at the plasma surface, respectively. The safety factor and pressure profile are given as

$$q(r) = 0.9\left[1 + \left(\frac{r}{0.5}\right)^{2\lambda}\right]^{1/\lambda} \quad , \qquad (5.4)$$

$$\text{with } \lambda = 2 + 2r^2 \quad ,$$

and

$$P(r) = p_0(1 - r^2)^2 \quad , \qquad (5.5)$$

where p_0 is the pressure at the magnetic axis and it is adjusted so that the poloidal beta has the given value. The maximum number of the Fourier components in the θ direction and radial mesh number are chosen to be 10 and 201, respectively, throughout the linear calculation except the case of $\varepsilon = 0$.

First, we investigate behaviours of the mode by eliminating the pressure term in the basic equations. Features of the mode obtained by the simulation are summarized as follows.

(1) The growth rate of the mode scarecely depends on the poloidal beta and aspect ratio as shown by the broken line in Fig. 5.1(a). This is consistent with the fact that the mode is current-driven one.

(2) The mode depends on the magnetic Reynolds number as $S^{-1/3}$ (a broken line in Fig. 5.1(b)), which is in good agreement with the previous analytical results[11] (a thick straight line in Fig. 5.1(b)).

Secondly, we carry out calculations for the equations with the pressure term. The results of the calculations are summarized as follows.

(3) As the aspect ratio and poloidal beta are increasing, both the internal ($S=\infty$) and resistive ($S<\infty$) modes become destabilized (solid lines in Fig. 5.1(a)). In the ideal case, especially, the growth rate depends on ε and β_p almost quadratically. The destabilization effect is more remarkable for smaller S value (solid lines in Fig. 5.1(b)).

(4) For higher values of $\varepsilon\beta_p$ and S the growth rate depends on S as $S^{-3/5}$ (Fig. 5.1(c)). The dependence suggests that the mode sensitive to ε and β_p are affected not by a pressure-driven mode but by the m=2 current-driven instability through the toroidal coupling. This is supported by the magnetic energy spectrum (Fig. 5.2) which shows that higher m components are more destabilized with increasing β_p. Infact, from Fig. 5.2(a) and (b), it is clear that if the value of S is sufficient low, the high m ($m > 1$) modes are easily destabilized with increasing β_p, and when β_p exceeds 1.5, the magnetic energy of m=2 mode becomes dominant instead of that of m=1 mode. As for the S dependence the magnetic energy of each mode is shown in Figs. 5.2(c) and (d) for the cases with ε=0.1 and β_p=2.0, and with ε=0.1 and β_p=1.0, respectively. Figure 5.2(c) shows that strong destabilization is induced in the case with high β_p and low S values. In Fig. 5.3 we show the β_p and S dependences of the eigenfunction of the θ component of

the plasma velocity, Φ'. From the figure it is seen that the eigenfunction of the m=1 mode is distorted considerably as the magnetic energy of the m=2 mode increases.

From the above observations we can conjecture that the destabliza-tion of the cylindrical m/n = 1/1 mode and change of it to the m=2 dominant mode are explained not by the direct consequence of inclusion of the pressure term but by the toroidal coupling of the mode with the higher m (m>1) modes in a high poloidal beta plasma. In the follow-ing we confirm the conjecture by deriving a growth rate of the mode analytically. We consider only the m=1 and m=2 Fourier components of the mode. The ideal MHD euqations for the m=1 and m=2 components are written as

$$\frac{d}{dr}\left[(\gamma^2+F_1^2)r^3\frac{d\tilde{\xi}_1}{dr}\right] = -\varepsilon\Lambda_{12}\tilde{\xi}_2 \quad , \tag{5.6}$$

$$\left(\frac{d^2}{dr^2}+\frac{1}{r}\frac{d}{dr}-\frac{4}{r^2}\right)\tilde{\psi}_2 - \frac{2}{rF_2}\frac{dJ_0}{dr}\tilde{\psi}_2 = -\frac{\varepsilon\Lambda_{21}\tilde{\xi}_1}{r^2F_2} \quad , \tag{5.7}$$

where

$$\Lambda_{12}\tilde{\xi}_2 = r^2[\gamma^2\Delta_{h1}(r\tilde{\xi}_2) + F_1\Delta_{g1}\tilde{\Psi}_2] - r^2\left[\frac{dp}{d\Psi}\frac{d\tilde{\Psi}_2}{dr} - \frac{2}{r}\frac{d}{dr}\left(r\frac{dP}{d\Psi}\right)\tilde{\Psi}_2\right]$$

$$+ 2r^2\left[\frac{d}{dr}\left(\frac{dP}{dr}\tilde{\xi}_2\right) + \frac{2}{r}\frac{dP}{dr}\tilde{\xi}_2\right] \quad , \tag{5.8}$$

$$\Lambda_{21}\tilde{\xi}_1 = r^2F_2\Delta_{g2}\tilde{\Psi}_1 - r^2\left[\frac{dP}{d\Psi}\frac{d\tilde{\Psi}_1}{dr} - \frac{1}{r}\frac{d}{dr}\left(r\frac{dP}{d\Psi}\right)\tilde{\Psi}_1\right]$$

$$- r^2\left[\frac{d}{dr}\left(\frac{dP}{dr}\tilde{\xi}_1\right) - \frac{1}{r}\frac{dP}{dr}\tilde{\xi}_1\right] \quad , \tag{5.9}$$

$\tilde{}$ denotes the perturbation quantity, γ is growth rate, $F_m = mB_\theta/r-n$, $\tilde{\xi}_m(= -\tilde{\phi}_m/\gamma r)$ is radial displacement of plasma and Δ_{gm} and Δ_{hm} are the operators including the metric tensor G^{ij} and H^{ij}, respectively. Here, we assume that the growth rate is much larger than that of the m=1 resistive mode which is not considered in this analysis.

From Eq.(5.6), the growth rate of ideal m=1 mode is derived as follows,

$$\gamma = \alpha_1 \varepsilon\beta_p \lambda \quad , \tag{5.10}$$

with

$$\lambda = - \tilde{\xi}_{2a}/\tilde{\xi}_{1a} \quad , \tag{5.11}$$

$$\alpha_1 = - \frac{\pi B_a^2}{r_1^4 q'(r_1)} \int_0^{r_1} P' r^2 dr \Big/ \int_0^1 Prdr \quad , \tag{5.12}$$

where r_1 is the singular surface of m=1 mode, $\tilde{\xi}_{ma} = \tilde{\xi}_m(r=r_1)$ and the prime denotes the derivative with respect to r. In this derivation of Eq.(5.10), we assume that $\tilde{\xi}_2 \cong \tilde{\xi}_{2a} r/r_1$ and $q \cong 1$ in the region $0 \leq r \leq r_1$. The signs of λ and α_1 are positive and the effect of $\varepsilon\beta_p$ to the stability is always destabilizing. The expression for λ in Eq.(5.11) is obtained by analyzing the m=2 mode as

$$\lambda = \alpha_2 \varepsilon(\beta_p + \mu) \quad , \tag{5.13}$$

where

$$\alpha_2 = - \frac{B_a^2}{4} \frac{\Psi_*(r_2)}{r_1 \Psi_*'(r_1)} \frac{\Psi_i(r_1)}{\Psi_i(r_2)} P'(r) \Big/ \int_0^1 Prdr \quad , \tag{5.14}$$

$$\mu = \frac{4 r_1 q'(r_1) \Delta'(r_1)}{B_a^2 P'(r_1)} \int_0^1 Prdr \quad , \tag{5.15}$$

r_2 is the singular surface of the m=2 mode, $\Psi_i(r)$ and $\Psi_*(r)$ are general solution and particular solution of Eq.(5.7) in the region $0 \leq r \leq r_2$. Substituting Eq.(5.13) into Eq.(5.10), we get the growth rate of ideal mode γ_I for the reduced set of equations of toroidal plasma as follows,

$$\gamma_I = \alpha_1 \alpha_2 \varepsilon^2 \beta_p (\beta_p + \mu) \quad . \tag{5.16}$$

The quadratic dependence of the growth rate on ε and β_p shown in Fig. 5.1(a) is well reproduced by Eq.(5.16). In the figure the black and open circles denote the cases for the fixed β_p and fixed ε, respectively.

Next, we consider the mode which is connected to the m=2 tearing mode in a cylindrical geometry. The growth rate of m=2 tearing mode in cylindrical geometry is given in Ref. 12 as

$$\gamma = c\eta^{3/5}(\Delta_0')^{4/5} \quad , \tag{5.17}$$

where

$$c = \frac{1}{2}\left(\frac{2q'}{q^2}\right)^{2/5}_{r=r_2} \quad , \tag{5.18}$$

$$\Delta_0 = \frac{\Psi_e'}{\Psi_e} - \frac{\Psi_i'}{\Psi_i}\bigg|_{r=r_2} \quad . \tag{5.19}$$

Ψ_i and Ψ_e are the general solutions of Eq.(5.7) for $0 \leq r < r_2$ and for $r_2 \leq r < a$, respectively. For comparison, this growth rate is shown as the straight solid line in Fig. 5.1(c). In the toroidal geometry, the value of Δ' is changed from Δ_0' due to the toroidal mode coupling and becomes

$$\Delta' = \Delta_0' + \frac{\alpha_2\varepsilon(\beta_p+\mu)}{\lambda-\alpha_2\varepsilon(\beta_p+\mu)}\Delta_*' \tag{5.20}$$

where

$$\Delta_*' = \frac{\Psi_*'}{\Psi_*} - \frac{\Psi_i'}{\Psi_i} \quad . \tag{5.21}$$

Using this Δ', we obtain the growth rate of the mode in toroidal plasma as

$$\gamma = \frac{1}{2}\left[\gamma_I + \sqrt{\gamma_I(\gamma_I + 4\gamma_*)}\right] \quad , \tag{5.22}$$

where

$$\gamma_* = c\eta^{3/5}(\Delta_*)^{4/5} \quad , \tag{5.23}$$

and γ_I is the ideal growth rate given by Eq.(5.16). This growth rate is approximately reduced to $\gamma \cong \gamma_I + \gamma_*$ for $\gamma_I >> \gamma_*$ and $\gamma \cong \sqrt{\gamma_I\gamma_*} \cong \varepsilon\beta_p\eta^{3/10}$ for $\gamma_I << \gamma_*$. Figure 5.1(c) shows that for the cases of $\varepsilon\beta_p = 0.225$ and 0.2 $\gamma - \gamma_I$ is proportional to $S^{-3/5}$ in the region of sufficiently high S value ($\gamma_I >> \gamma_*$) but for the case of $\varepsilon\beta_p = 0.1$ the S dependence of $\gamma - \gamma_I$ is different because of the dominant m=1 mode

(Fig. 5.1(b)). Furthermore, the S dependence of the growth rate in the low S region ($\gamma_I << \gamma_*$) is approximately given as $S^{-3/10}$, which seems reasonable from the above numerical treatment.

5.4 Nonlinear Calculations of Resistive Modes with the Toroidal Effect

In this Section we study the nonlinear evolution of the resistive instabilities in a toroidal plasma. As the m/n = 3/1 mode (according to the common usage we call a perturbation with m/n helicity a "m/n mode") is strongly destabilized by the toroidal coupling incorporated with the finite poloidal beta effect, emphasis of the investigation is placed on the possibility of initiation of the disruptive instability by the toroidal coupling. The equilibrium in the previous Section is used for the simulation. This equilibrium is stable against the disruptive instability in the sense that the m/n = 2/1 and m/n = 3/2 modes do not overlap each other during the nonlinear simulation in which the toroidal coupling and pressure perturbation are not taken into account.

First, we calculate the effect of the toroidal coupling without considering the pressure perturbation and finite poloidal beta effect. Figure 5.4 shows the temporal evolution of the magnetic islands with different helicities for the inverse aspect ratio ε=0.1, the poloidal beta β_p=0.0, and the magnetic Reynolds number $S = 2 \times 10^4$. The phase of the initial perturbation of m/n = 2/1 mode is chosen to be the same as that of the m/n = 1/1 mode for one case (Fig. 5.4(a)) and to be opposite for the other (Fig. 5.4(b)). For comparison, a cylindrical case (ε=0.0) is shown by a broken line in each figure. Until $t \sim 50$ behaviour of the modes in a toroidal plasma is essentially the same as in the cylindrical case. After $t \sim 50$, however, the modes evolve differently for the toroidal cases with different initial phases, which seems to be attributed to the effect of the toroidicity. For the in-phase case, the m=2 island shrinks. On the other hand, the island width for the opposite phase case increases. This can be seen more clearly in the evolution of the magnetic energies of each mode (Fig. 5.5),

$$E_{m/n} = \frac{\pi}{2} \int_0^a \left[\left(\frac{\partial \Psi_{m/n}}{\partial r} \right)^2 + \left(\frac{m}{r} \Psi_{m/n} \right)^2 \right] r dr \quad . \tag{5.24}$$

The energy of the m=2 mode with the initially opposite phase grows exponentially with the growth rate of about half of the m=1 mode growth rate (Fig. 5.5(b)), while the energy of the m=2 mode for the in-phase case decreases (Fig. 5.5(a)). The different behaviour of the modes for the different initial phases is explained qualitatively as follows. The total energy of the reduced set of the resistive MHD equations in a toroidal plasma is given by

$$E = \frac{1}{2}\int_0^a \left[\left(\frac{R}{R_0}\right)^2 |\vec{\nabla}\Phi|^2 + \left(\frac{R_0}{R}\right)^2 |\vec{\nabla}\Psi|^2\right] d\tau \quad . \tag{5.25}$$

This energy can be divided into two parts; the cylindrical energy E_{cyl}, and toroidal one E_{tor}. By using the cylindrical part ($\bar{g}^{ij}$) and toroidal part ($\tilde{g}^{ij}(\theta)$) of the reciprocal metric g^{ij}, we can rewrite the toroidal energy E_{tor}, up to the first order of ε, as

$$E_{tor} = \int_0^a \left[\{\tilde{g}^{ij}(\theta) + \tilde{g}^{ij}(-\theta)\}\left(\frac{\partial\Phi_1}{\partial x^i}\frac{\partial\Phi_2}{\partial x^j} + \frac{\partial\Psi_1}{\partial x^i}\frac{\partial\Psi_2}{\partial x^j}\right)\right.$$

$$\left. - \frac{4r}{R_0} g^{-ii}\frac{\partial\Phi_1}{\partial x^i}\frac{\partial\Phi_2}{\partial x^i}\right] d\tau \quad , \tag{5.26}$$

where we take into account only the toroidal coupling between the m=1 and m=2 modes. We assume that Φ_1 and Φ_2 are approximately expressed as $\Phi_1 \cong \hat{\Phi}_1\, r/r_s|_{m=1}$ and $\Phi_2 \cong \hat{\Phi}_2\{r/r_s|_{m=1}\}^2$ in the region $r \leq r_s|_{m=1}$. Then using the relation $\Psi_m = -F_m\Phi_m/\gamma_m$, we have

$$E_{tor} \cong \frac{4}{R_0}\int_0^{r_s|_{m=1}} dr(\Psi_1\Psi_2 - 3\Phi_1\Phi_2) \cong \frac{4}{R_0}\int_0^{r_s|_{m=1}} dr\ \Psi_1\Psi_2, \tag{5.27}$$

where γ_m is the growth rate of each mode and $F_m = mB_\theta/r - nB_z/R_0$. This expression shows that the sign of the toroidal coupling energy E_{tor} depends on the phase between the m=1 and m=2 modes. Because of the small dissipation, the total energy of the system is almost conserved, and E_{cyl} is larger (smaller) than that in the cylindrical plasma for $\Psi_1\Psi_2 < 0$ ($\Psi_1\Psi_2 > 0$). Since the m=1 mode has the larger growth rate and larger amplitude than those of the m=2 mode, the effect of the toroidal coupling on the m=1 mode can be neglected. Therefore, the energy of the m=2 mode increases due to the toroidal coupling for

$\Psi_1\Psi_2 < 0$ and vice versa, which also explain the phase locking observed in the experiments.

Next, we investigate the finite poloidal beta effect for an equilibrium of ε=0.1, β_p=1.0, and $S = 2 \times 10^4$ with and without considering the pressure perturbation. The initial phase of the m=2 mode is chosen to be opposite to that of the m=1 mode. Figure 5.6 shows the evolutions of the magnetic islands (Fig. 5.6(a)) and magnetic energy (Fig. 5.6(b)). It is seen that there is no remarkable finite poloidal beta effect in the case without the pressure perturbation (broken lines in Fig. 5.6). On the other hand, for the case with the pressure perturbation the finite poloidal beta effect brings out a remarkable difference in the evolutions of the magnetic islands and magnetic energy. In this case the m/n=2/1 and m/n=3/1 modes are strongly destabilized and they grow rapidly with the linear growth rate of the m/n=1/1 mode even after the internal disruption occurs and the m/n=1/1 mode disappears. With the strong destabilization of the modes the m/n=2/1 island becomes large and contacts with the m/n=3/2 and m/n=3/1 islands. This island overlapping makes the magnetic lines stochastic and finally destroy the magnetic surface (Fig. 5.7), but it is not followed by the destablization of the m/n=3/2 mode and does not lead to the major disruption, i.e., the rapid release of the magnetic energy, as shown in the simulations by the ORNL group. A negative voltage spike is observed in the simulation (Fig. 5.8), but it is caused by the internal disruption and the amplitude is only about a few percent of the major disruption.

5.5 Discussion and Conclusions

We have studied the linear and nonlinear MHD phenomena of a tokamak plasma by using the reduced set of the resistive MHD equations, especially, to clarify the finite poloidal beta effect and toroidal coupling. From the linear analysis of the equilibrium accurate up to the order ε it is found that the m=2 tearing mode is strongly destabilized by the toroidal coupling with the m=1 internal mode if the pressure perturbation is taken into account. The numerically obtained dependence of the growth rate on the aspect ratio and poloidal beta is in good agreement with analytical result. In the present tokamak plasmas the magnetic

Reynolds number is in the range of $10^5 \sim 10^6$ and the m=2 mode is destabilized strongly for large values of $\varepsilon\beta_p$.

Nonlinear calculations are also carried out. Even in the nonlinear regime it is found that the finite β_p effect is small for the case without the pressure perturbation. For the case with the pressure perturbation, however, the computational result shows that the m/n=2/1 and m/n=3/1 modes are strongly destabilized by the m/n=1/1 mode through the toroidal coupling, leading to destroy the magnetic surfaces by the island overlapping which does not lead to the rapid release of the magnetic energy.

As for the major disruption the finite poloidal beta effect and toroidal coupling are not directly responsible to the instability. However, the above-described island overlapping leads to the magnetic field stochastization. And the stochastization leads to the flattening of the electron temperature profile and high plasma resistivity, by which the current profile is flattened. Combination of the above effect and the flattening of electron temperature due to the internal disruption may change the current profile to the similar one of the major disruption calculations in Ref. 6 and cause the major disruption.

References

1) M. Azumi, (1976) unpublished.
2) A.F. Danilov, Yu.N. Dnestrovskii, D.P. Kostomarov and A.M. Popov, Fiz. Plasmy 2, (1976) 167.
3) B.V. Waddell, M.N. Rosenbluth, D.A. Monticello and R.B. White, Nucl. Fusion 16, (1976) 528.
4) R.B. White, D.A. Monticello and M.N. Rosenbluth, Phys. Rev. Lett. 39, (1977) 1618.
5) B.V. Waddell, B. Carreras, H.R. Hicks, J.A. Holmes and D.K. Lee, Phys. Rev. Lett. 41, (1978) 1368.
6) B.V. Waddell, B. Carreras, H.R. Hicks and J.A. Holmes, Phys. Fluids 22, (1979) 896.
7) B. Carreras, H.R. Hicks, J.A. Holmes and B.V. Waddell, Phys. Fluids 23, (1980) 1181.
8) B. Carreras, H.R. Hicks and D.K. Lee, Phys. Fluids 24, (1981) 66.
9) G. Kurita, M. Azumi, T. Tuda, T. Takizuka, T. Tsunematsu, S. Tokuda, K. Itoh and T. Takeda, "Major Disruption Process in Tokamak", Japan Atomic Energy Research Institute Report JAERI-M 9788 (1981).
10) S. Yamamoto et al., Nucl. Fusion 21, (1981) 993.
11) B. Coppi, R. Galvão, R. Pellat, M.N. Rosenbluth and P.H. Rutherford, Fiz. Plasmy 2, (1976) 961.
12) H.P. Furth, P.H. Rutherford and H. Selberg, Phys. Fluids 16, (1973) 1054.

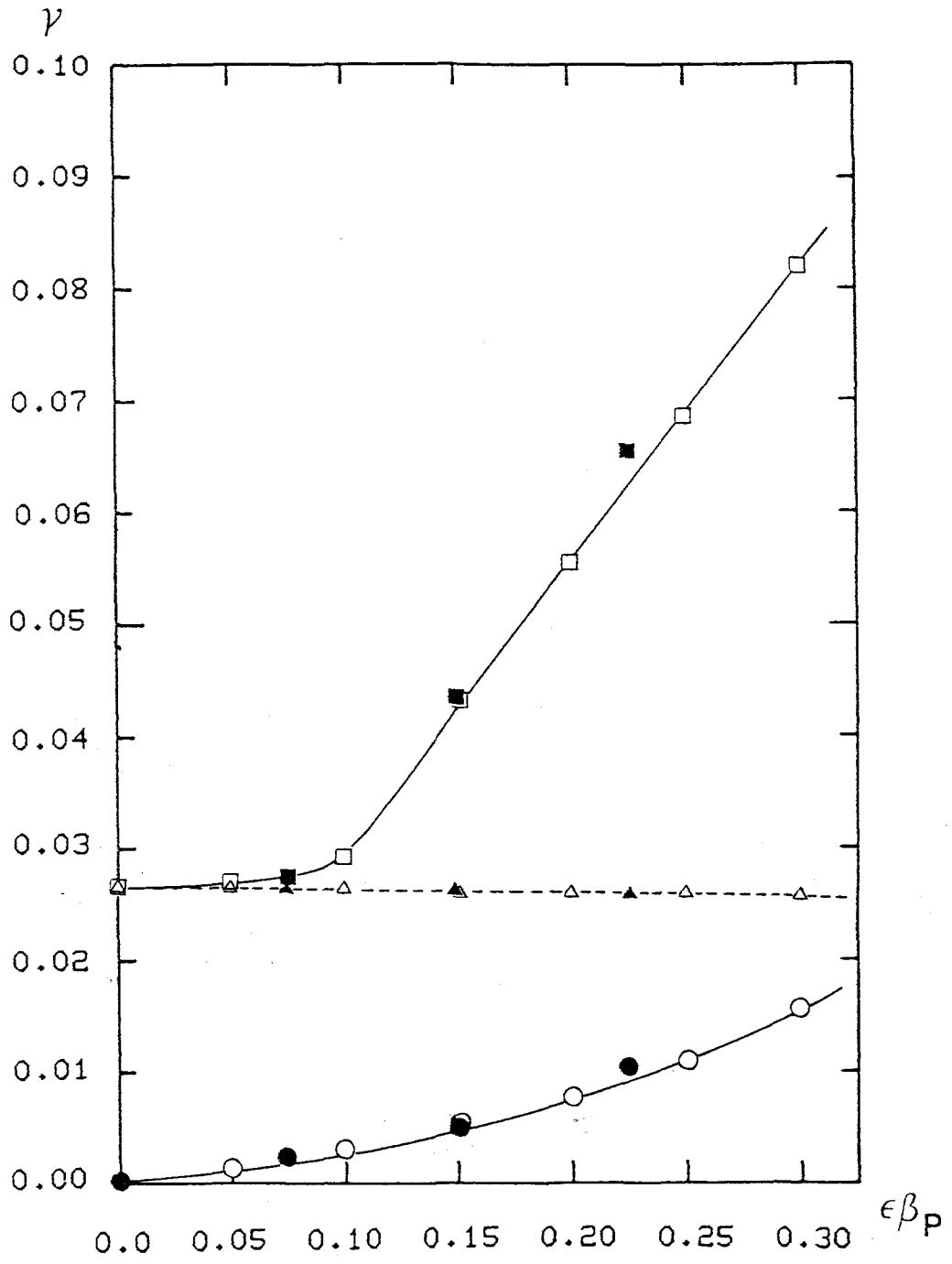

Fig. 5.1(a) Linear growth rate of n=1 mode versus $\varepsilon\beta_p$. The open symbols represent the case with changing β_p for fixed ε(=0.1), and the black symbols represent the case with changing ε for fixed β_p(=1.5). △ and ▲ with a broken line is the result of calculation without pressure perturbation. The values of S are 2×10^4 for △ ▲ □ ■ and ∞ for ○ and ●.

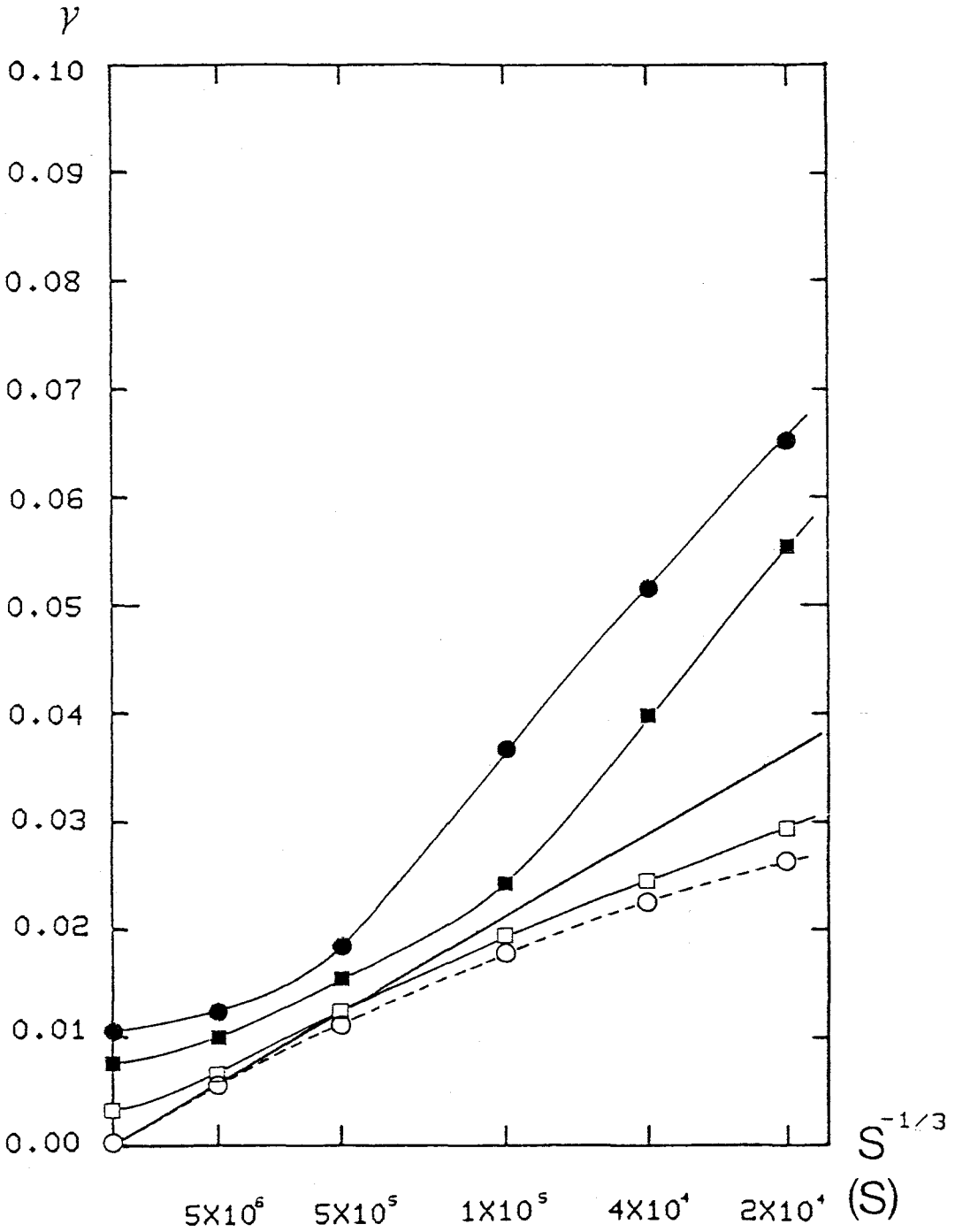

Fig. 5.1(b) Linear growth rate of n=1 mode versus $S^{-1/3}$. ○ is for the case without pressure perturbation ($\varepsilon\beta_p=0$). □ and ■ denote the case of $\beta_p=1.0$ and $\beta_p=2.0$ for $\varepsilon=0.1$ and ● denotes the case of $\beta_p=1.5$ and $\varepsilon=0.15$. The straight solid line is analytical growth rate of m=1 resistive mode[11].

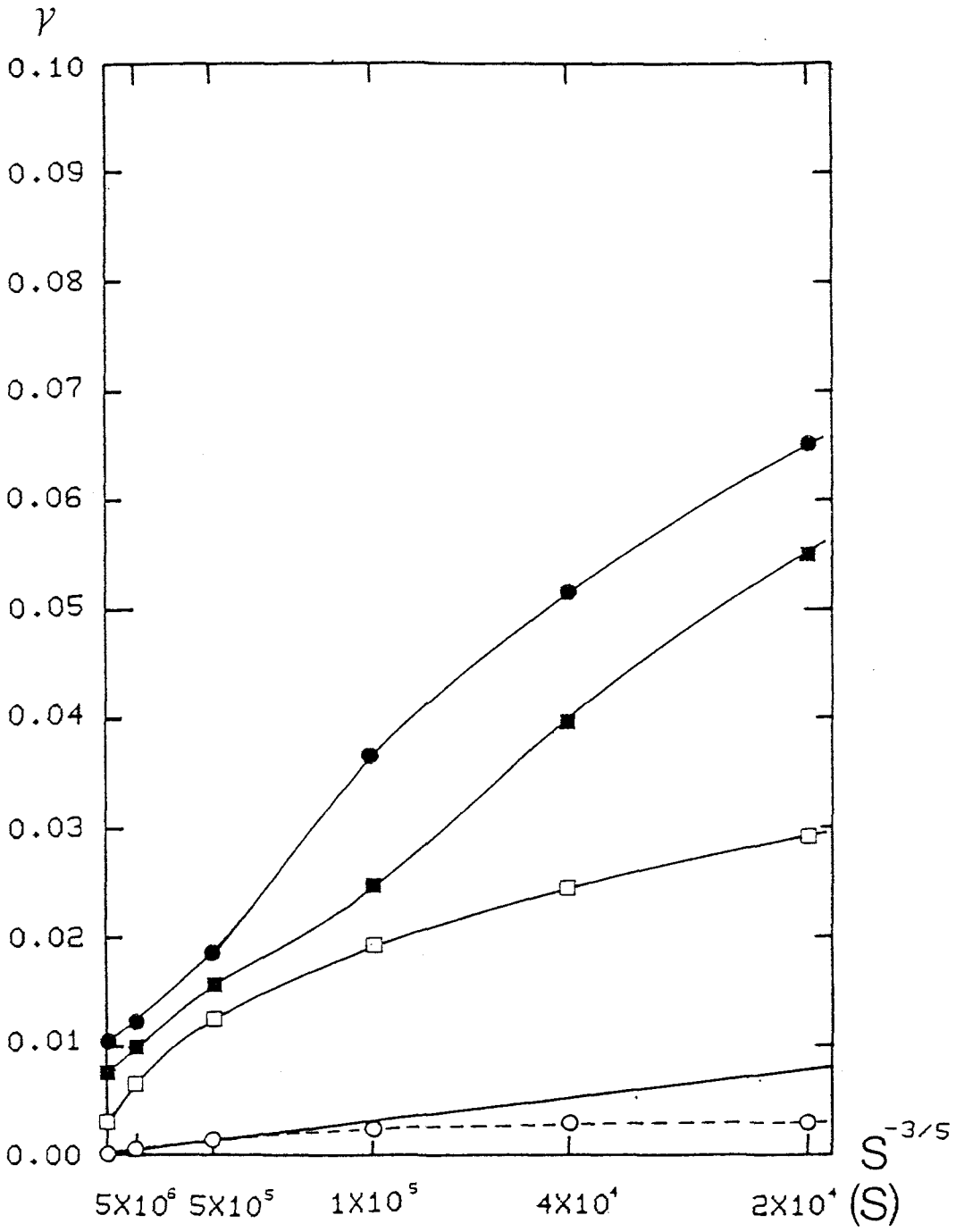

Fig. 5.1(c) Linear growth rate of n=1 mode versus $S^{-3/5}$. The meaning of symbols is the same as in Fig. 5.1(b), except the open circles, which are the numerically obtained growth rate of cylindrical m=2 tearing mode. The straight solid line is analytical growth rate of m/n=2/1 tearing mode[12].

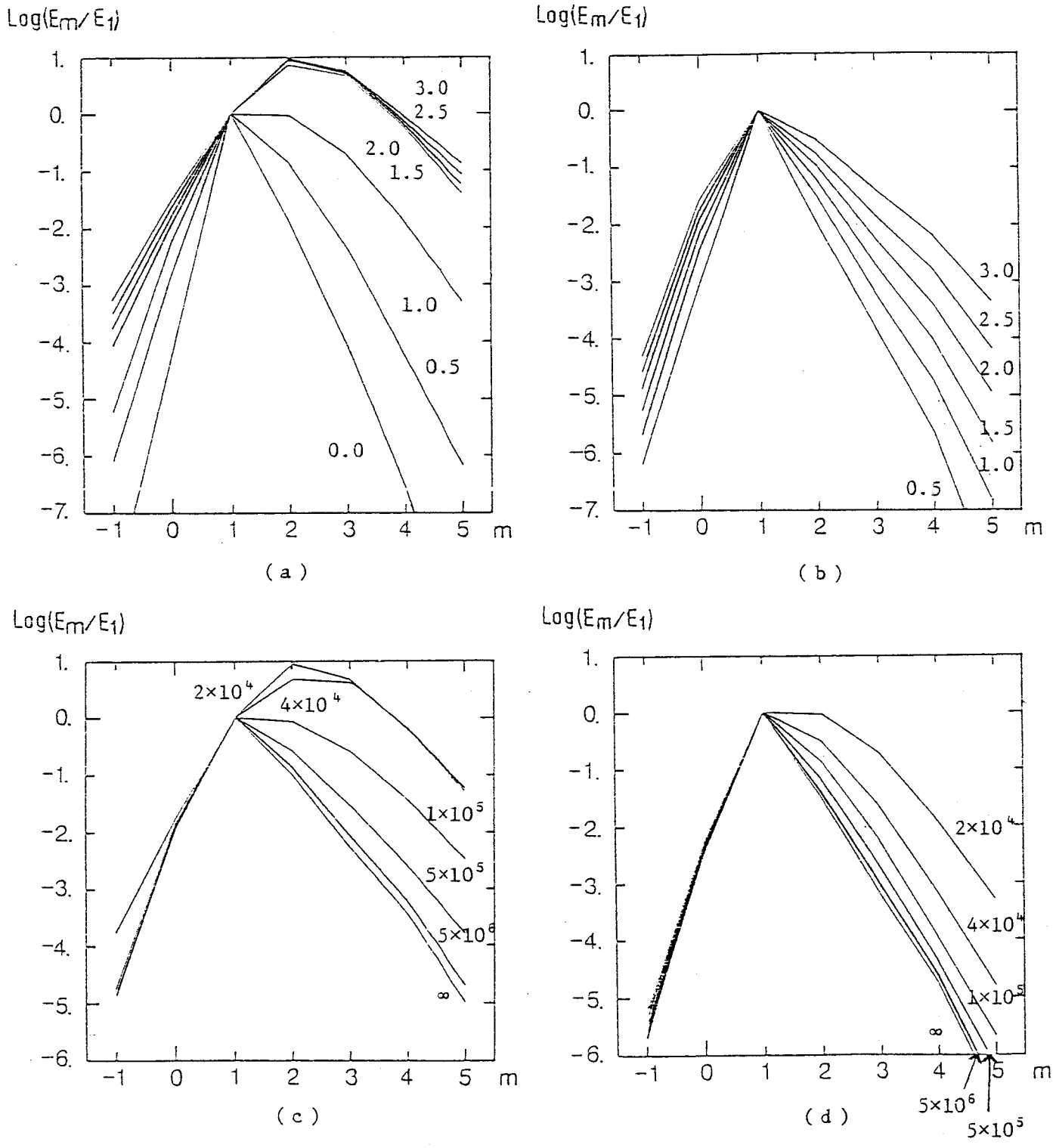

Fig. 5.2 Magnetic energy of the n=1 mode versus the Fourier mode number: (a) β_p dependence for fixed $\varepsilon(=0.1)$ and $S(=2\times10^4)$, (b) β_p dependence for fixed $\varepsilon(=0.1)$ and $S(=\infty)$, (c) S dependence for fixed $\varepsilon(=0.1)$ and $\beta_p(=2.0)$ and (d) S dependence for fixed $\varepsilon(=0.1)$ and $\beta_p(=1.0)$.

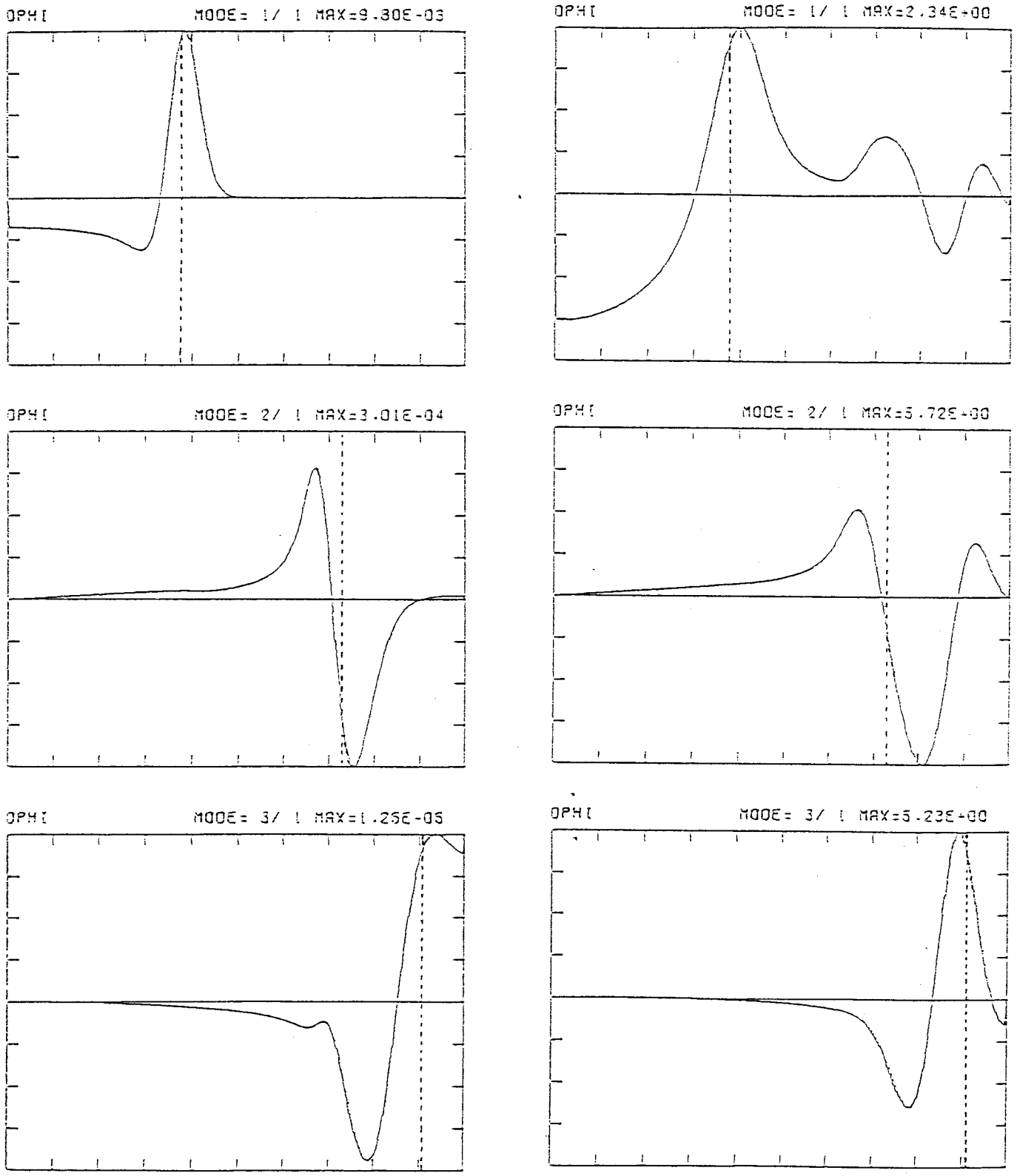

(a) (b)

Fig. 5.3 Eigenfunctions of v^{θ} of n=1 mode for (a) β_p=0 and (b) β_p=3 for fixed ε(=0.1) and S(=2×10^4). The poloidal mode numbers are m=1, m=2, and m=3 from the top to bottom. In each sub-figure, the dotted line denotes the position of the singular surface of the mode.

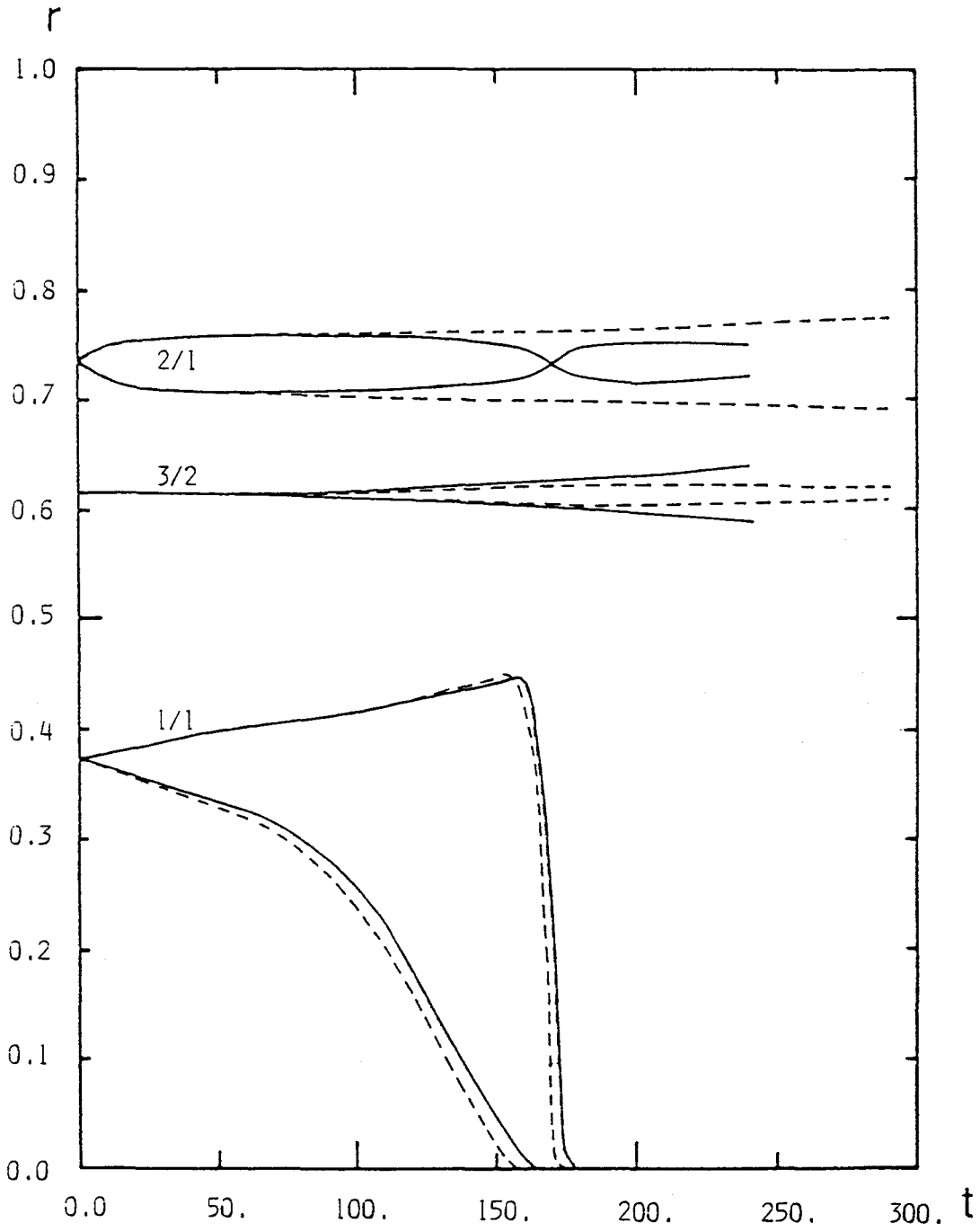

Fig. 5.4(a) Evolution of the magnetic island with different helicity m/n for the case that the initial phase of the m=2 mode is the same as that of m=1 mode. The results of the cylindrical calculation are shown by broken lines. The calculation is carried out for the case with $\varepsilon=0.1$, $\beta_p=0.$ and $S=2\times10^4$.

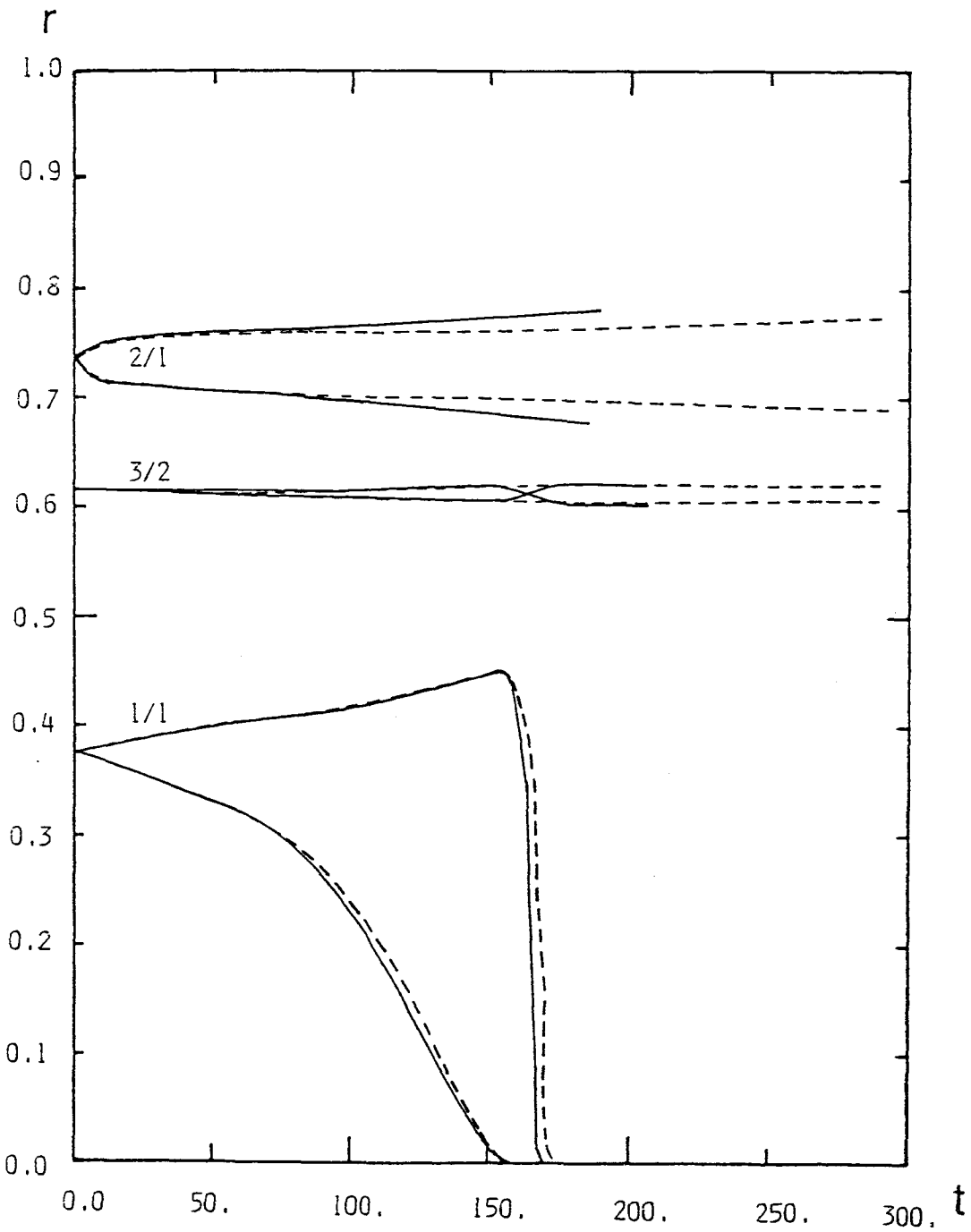

Fig. 5.4(b) Evolution of the magnetic island with different helicity m/n for the case that the initial phase of the m=2 mode is opposite to that of m=1 mode. Broken lines show the results of cylindrical calculation.

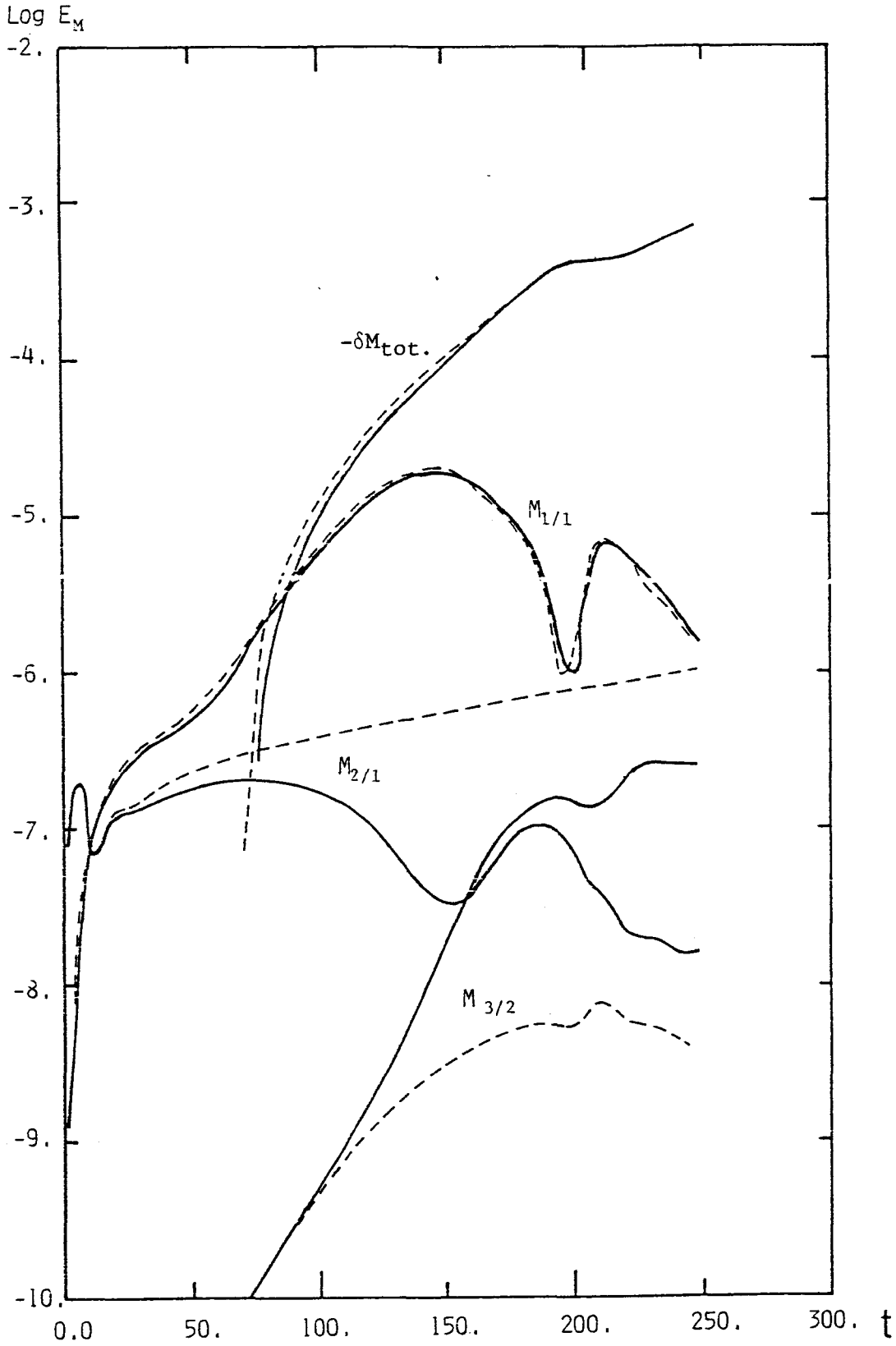

Fig. 5.5(a) Evolution of the magnetic energy of each mode for the same case as Fig. 5.4(a). The results of the cylindrical calculation are also shown by the broken lines.

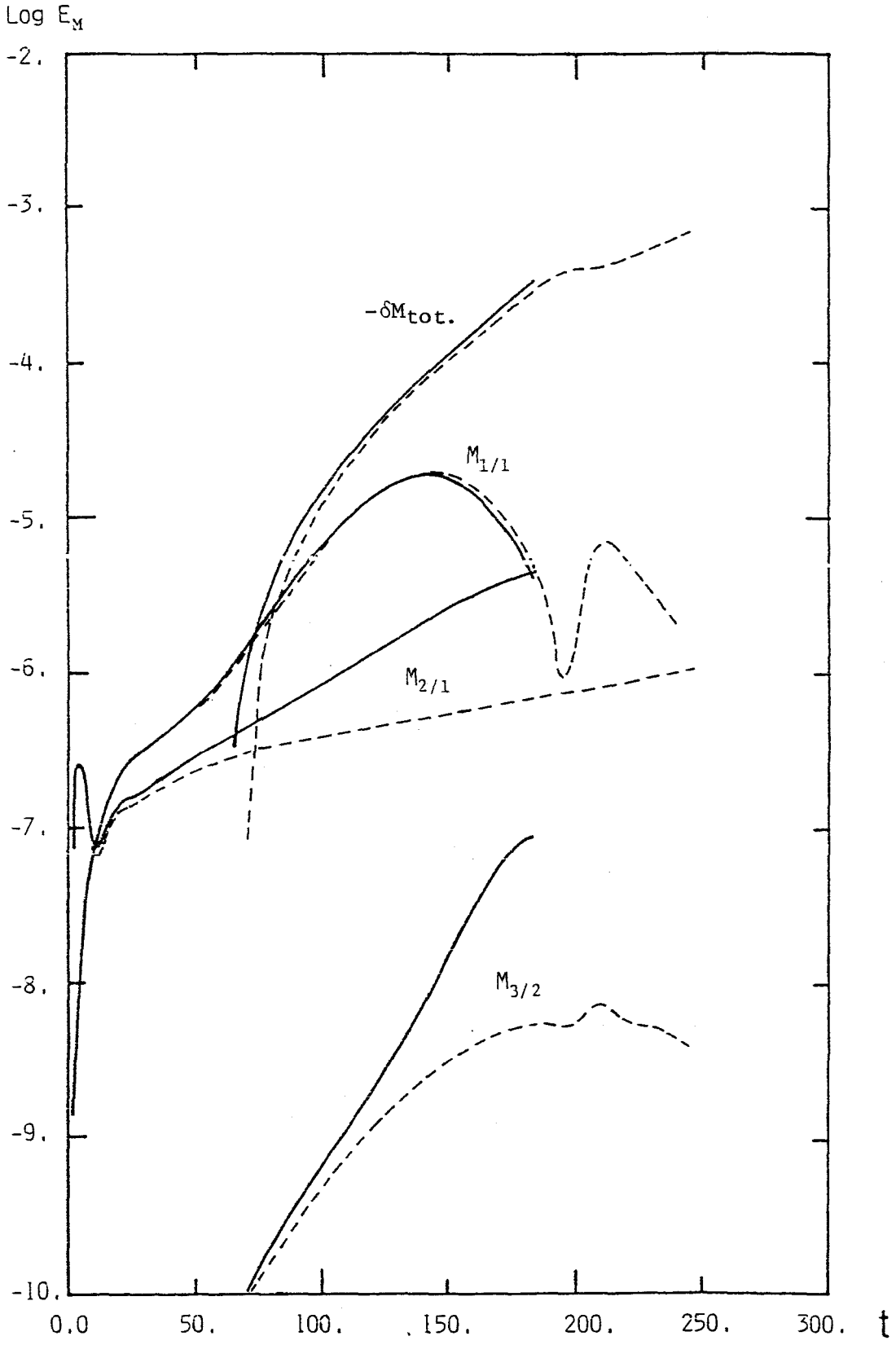

Fig. 5.5(b) Evolution of the magnetic energy of each mode for the same case as Fig. 5.4(b). Broken lines are the results of cylindrical calculation.

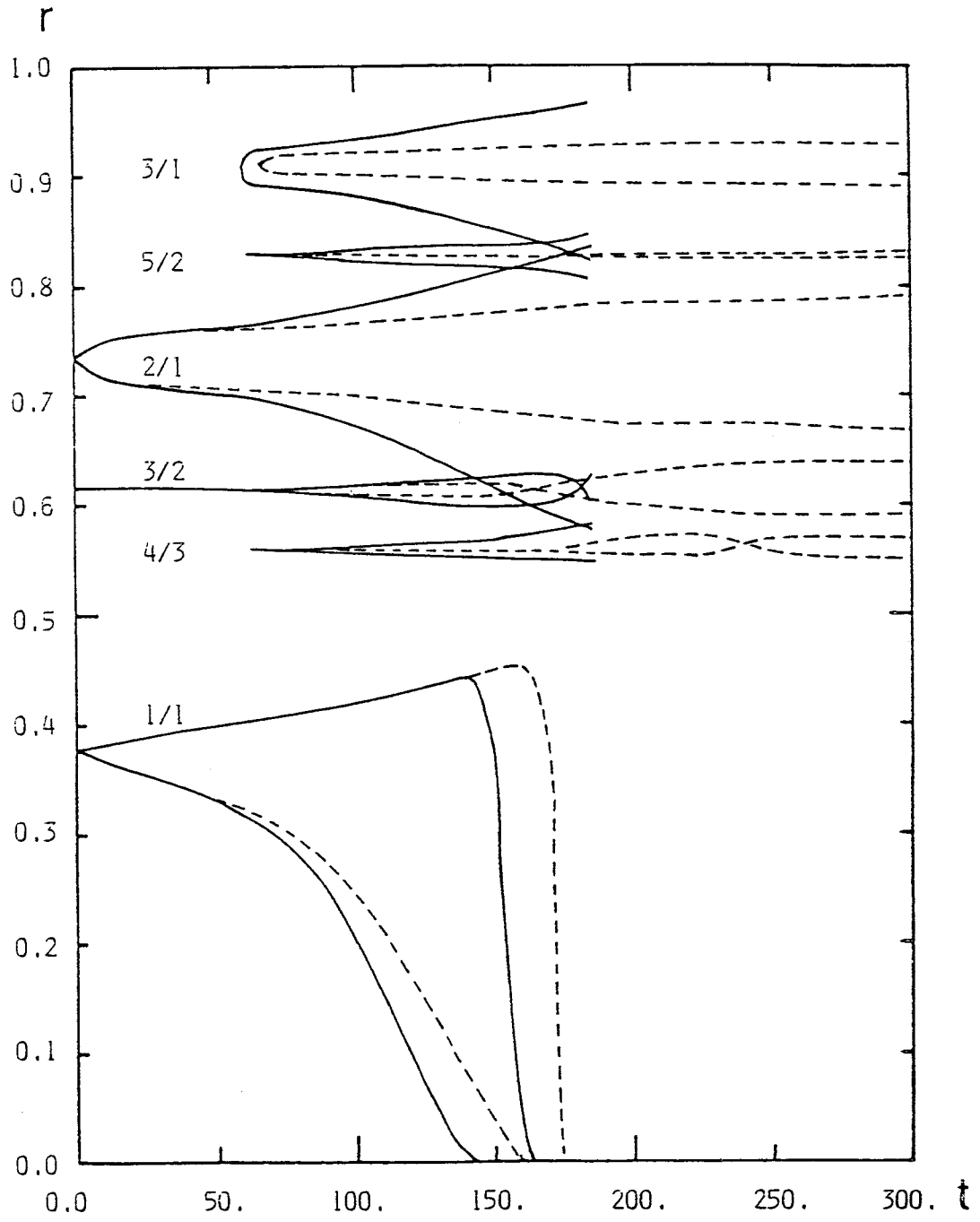

Fig. 5.6(a) Evolution of the magnetic island with different helicity m/n. Solid and broken lines show the case with and without the pressure perturbation, respectively. The calculation is carried out for the case with $\varepsilon=0.1$, $\beta_p=1.0$ and $S=2\times10^4$.

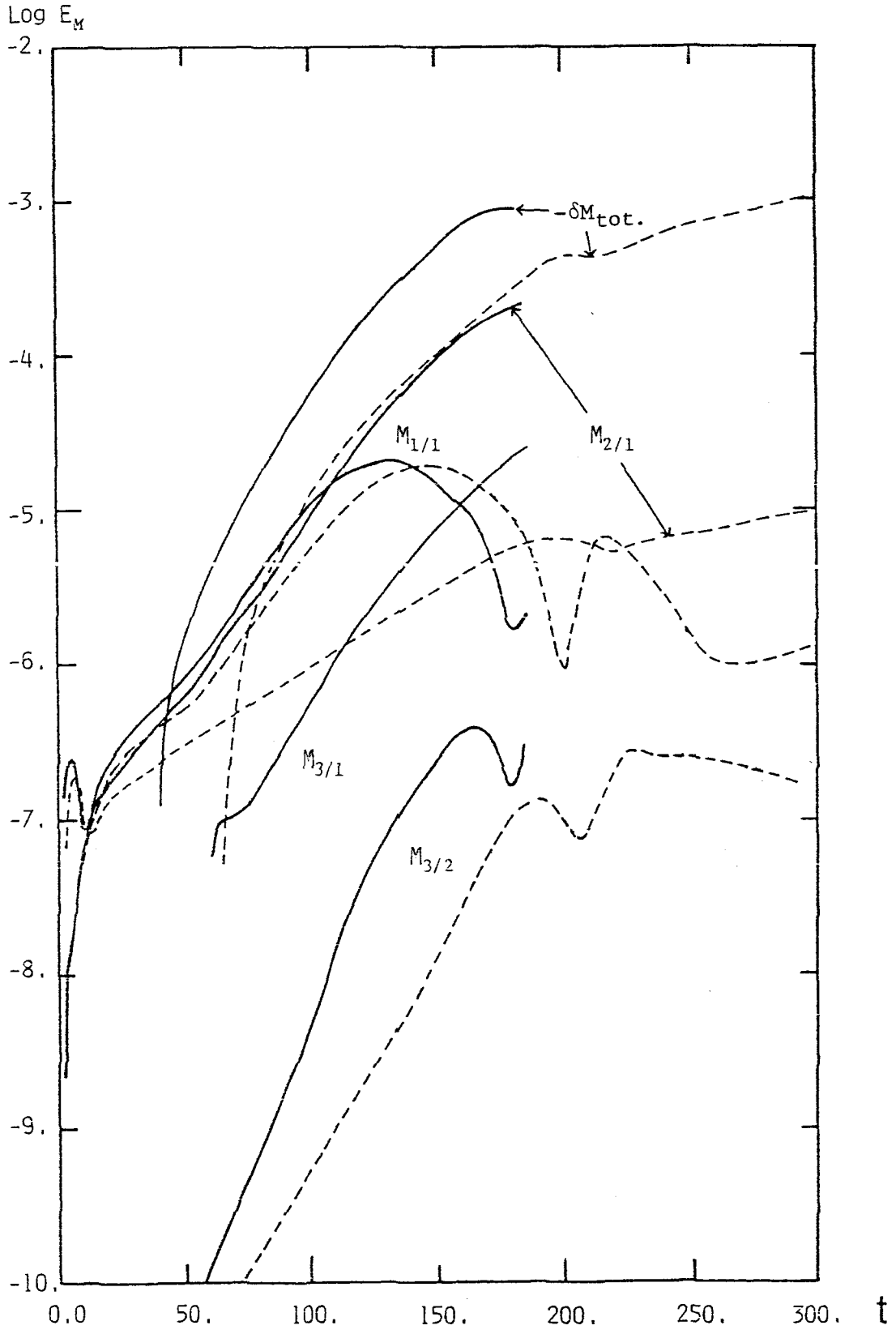

Fig. 5.6(b) Evolution of the magnetic energy of each mode for the same case as Fig. 5.6(a). Solid and broken lines show the cases with and without pressure perturbation, respectively.

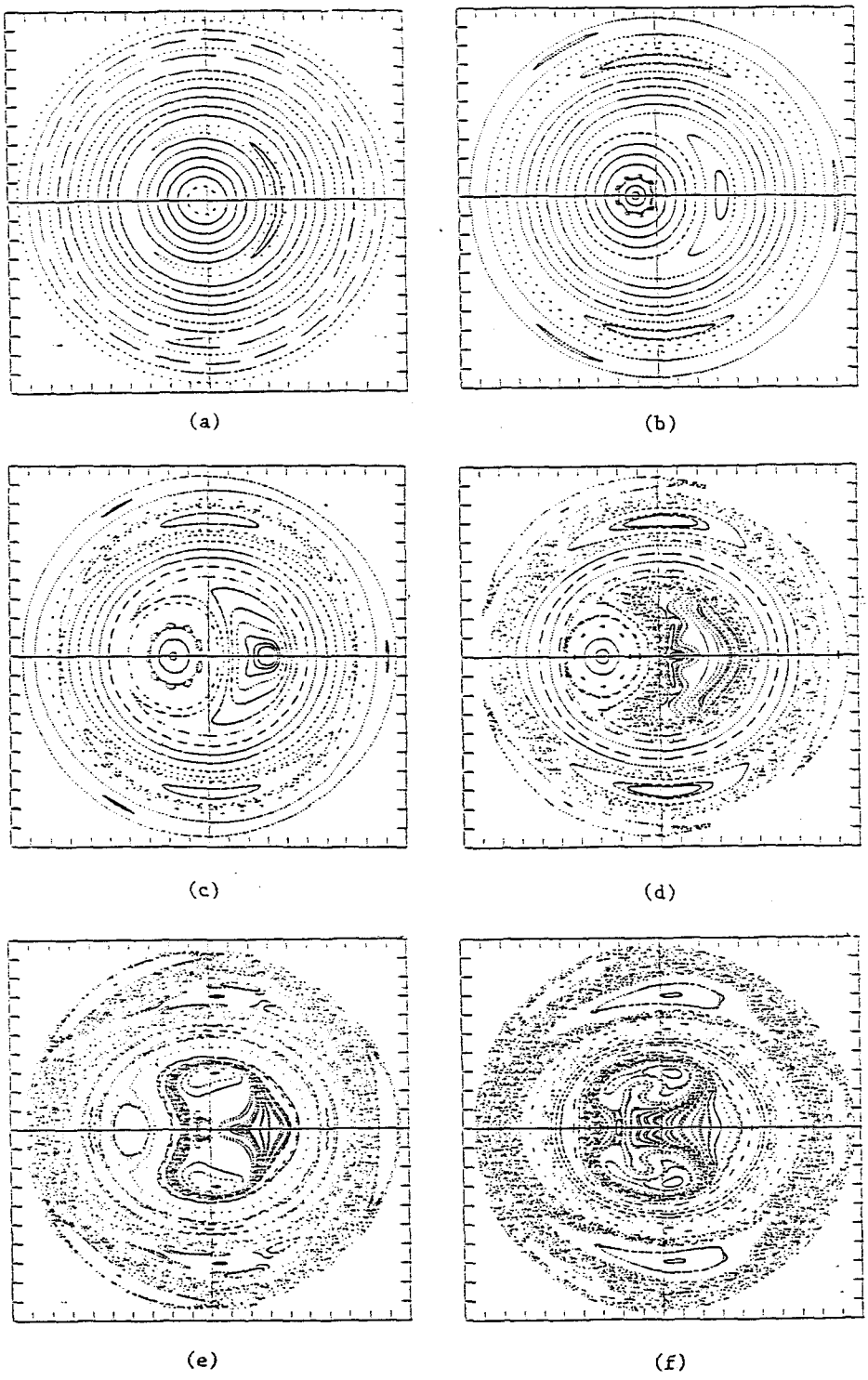

Fig. 5.7 Intersections of the trajectories of the magnetic field lines at the poloidal plane, ζ=0, for (a) t=50, (b) t=100, (c) t=125, (d) t=150, (e) t=165, and (f) t=180. In each subfigure several tens of trajectories with different starting points are demonstrated. Internal disruption occurs at t ≅ 160.

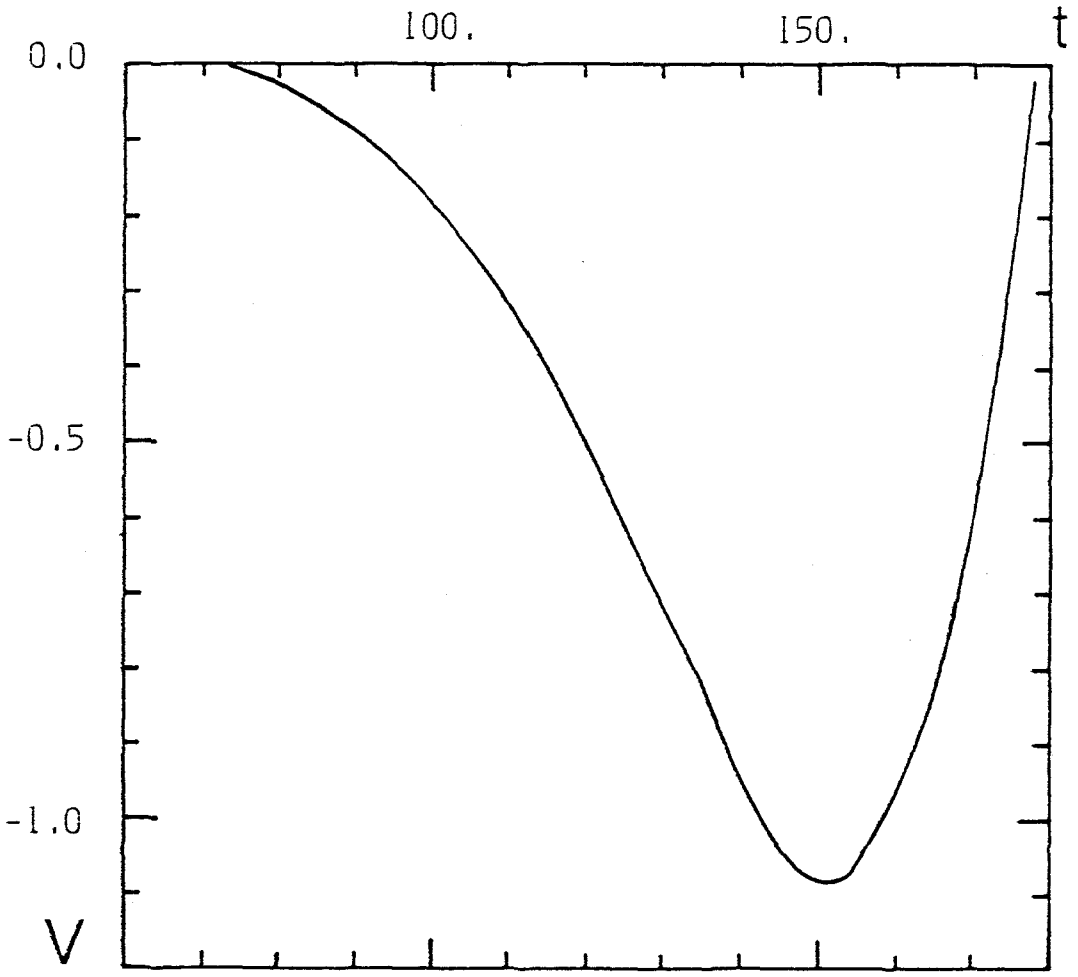

Fig. 5.8 Time evolution of the one-turn voltage at the limiter for the case $\varepsilon=0.1$, $\beta_p=1.0$ and $S=2\times10^4$ with pressure perturbation.

Chapter VI

Conclusions and Discussion

The MHD phenomena in a tokamak plasma have been analyzed extensively. These are the external kink and nonlinear positional instabilities, the major disruption process and related problems concerning the effects of toroidicity and finite poloidal beta on the low n resistive modes. The former two problems are analyzed on the basis of the ideal MHD model and the latter two problems are analyzed on the basis of the reduced set of the resistive MHD equations. In the following brief conclusions and discussion are given in the order of the Chapters of the text.

In Chapter II the ideal MHD stabilities of a toroidal plasma with a free boundary are investigated, and it is shown that, when a conducting shell is placed far from the plasma surface, toroidicity scarcely affects the external kink mode for a slender tokamak but it reduces the growth rate of a fat tokamak. When the shell is placed close to the plasma surface, however, the toroidal effect is notable in comparison with the previous case. For these analyses we have developed a two-dimensional linear evolutional code ZEPHYrus. The results by the code are compared critically with an analytical and numerical results and the code has been found to be accurate for the low m mode analyses but for the higher m modes the effect of the finite azimuthal mesh size prevents accurate calculation of the growth rate.

In Chapter III we described the numerical method of the nonlinear ideal MHD code AEOLUS-P developed for analyses of the positional instabilities of a tokamak plasma. The basic equations are given in the complete conservative form. To solve the equations the dynamical grid method in combination with a new rezoning algorithm is successfully applied. For test of the accuracy of the code MHD oscillations in a cylindrical model are computed and the frequencies of the plasma velocity oscillations are in good agreement with those obtained by the one-dimensional spectral code THALIA.

In Chapter IV we have studied the nonlinear evolution of a multi-helicity tearing mode in a cylindrical geometry and demonstrated that a major disruption is caused by nonlinear destabilization of the m/n=3/2 mode through the nonlinear coupling with the m/n=2/1 mode. As for initiation of the major disruption the flattening of the q profile due to the internal disruption is one of candidates but the numerical result shows that it does not cause the major disruption contrary to the simple expectation. The flattening occurs only inside of the q=1 magnetic surface and the q profile is not affected near the m/n=2/1 and m/n=3/2 surfaces. Therefore, in order to explain the initiation process of the major disruption we have to take into account another effect such as the toroidal effect.

In Chapter V we have studied the effects of the toroidicity and finite poloidal beta on the low n resistive modes in relation to the disruptive instabilities. By the linear calculation it is found that in a highly resistive plasma with large value of $\varepsilon\beta_p$. The m=2 tearing mode is strongly destabilized by the m=1 internal mode through the toroidal coupling. Nonlinear calculation shows that linearly destabilized m/n=2/1 and m/n=3/1 modes have large magnetic islands and lead to destruction of magnetic surfaces by the island overlapping. In spite of the island overlapping the major disruption or rapid release of the magnetic energy does not occur. However, there remains another possibility of the major disruption. The stochastization of the magnetic field lines due to the above island overlapping leads to flattening of the electron temperature profile in this region. Consequently the plasma resistivity becomes high and the plasma current profile is made flattened. With the effect of the internal disruption this flattening of the plasma current profile around the q=2 surface may change the q profile similar to the one used for the disruption calculation by Waddell et al., and the major disruption occurs.

Acknowledgements

The author would like to express his sincere thanks to Prof. H. Itô of Osaka University who introduced him to the field of thermonuclear fusion research and has been encouraging him continuously. He also wishes to express his appreciation to Prof. T. Amano of Nagoya University who directed him to the computational study of the MHD phenomena in a tokamak. His appreciation also goes to Prof. T. Ishimura and Prof. K. Watanabe of Osaka University for the encouragements and advices. He also would like to acknowledge the kindly guidance and encouragements of Prof. H. Oshiyama of Kyoto University of Industrial Arts and Textile Fibers at the beginning of his study of thermonuclear fusion research.

The author expresses his sincere gratitude to Dr. Y. Obata, Head, Division of Thermonuclear Fusion Research in JAERI for his continuing encouragement during the course of the work. He also wishes to express his appreciation to Dr. M. Tanaka, Deputy Head, Division of Thermonuclear Fusion Research in JAERI for his continuing encouragement and advice.

He would like to express his especial thanks to Drs. M. Azumi, T. Tsunematsu and T. Takeda for the excellent guidance and helpful discussion through the course of the work. Especially he owed to Dr. T. Takeda for the critical reading and helpful advice in preparation of the final manuscript. He also wishes to thank Drs. T. Tuda and T. Takizuka for their valuable discussion. He is much grateful to Prof. M. Okamoto of Nagoya University and Prof. M. Wakatani of Kyoto University for their fruitful discussion and encouragements.

Mr. Y. Tanaka of Fujitsu Ltd. is acknowledged for the computational support. The whole work is carried out by using the computer system at the JAERI computer center and the author would like to thank the staff of the computer center for the kind support in using the computer system.

Appendix

Basic Equations for AEOLUS-P in Toroidal Geometry

In this Appendix, we rewrite the basic equations (Eqs.3.3) so that the equations include the effect of toroidal curvature. The change is needed for the terms which contain ϕ components of $\vec{v}$ and $\vec{B}$. By adding the terms we have following equations for the toroidal calculation,

$$\frac{\partial}{\partial t}(\rho v_x) = -\vec{\nabla}\cdot(\rho v_x \vec{v}) - \frac{\partial P}{\partial x} + \vec{\nabla}\cdot(B_x \vec{B}) + x(\rho \hat{v}_\phi^2 - \hat{B}_\phi^2) \quad , \tag{A.1}$$

$$\frac{\partial}{\partial t}(x^2 \rho \hat{v}_\phi) = -\vec{\nabla}\cdot(x^2 \rho \hat{v}_\phi \vec{v}) + \vec{\nabla}\cdot(x^2 \hat{B}_\phi \vec{B}) \quad , \tag{A.2}$$

$$\frac{\partial}{\partial t}(\rho v_y) = -\vec{\nabla}\cdot(\rho v_y \vec{v}) - \frac{\partial P}{\partial y} + \vec{\nabla}\cdot(B_y \vec{B}) \quad , \tag{A.3}$$

$$\frac{\partial B_x}{\partial t} = -\vec{\nabla}\cdot(B_x \vec{v}) + \vec{\nabla}\cdot(v_x \vec{B}) \quad , \tag{A.4}$$

$$\frac{\partial \hat{B}_\phi}{\partial t} = -\vec{\nabla}\cdot(\hat{B}_\phi \vec{v}) + \vec{\nabla}\cdot(\hat{v}_\phi \vec{B}) \quad , \tag{A.5}$$

$$\frac{\partial B_y}{\partial t} = -\vec{\nabla}\cdot(B_y \vec{v}) + \vec{\nabla}\cdot(v_y \vec{B}) \quad , \tag{A.6}$$

where

$$\hat{v}_\phi = \frac{v_\phi}{x} \quad , \qquad \hat{B}_\phi = \frac{B_\phi}{x} \quad . \tag{A.7}$$

By the spatial integration of the above equations we obtain the basic equations for a toroidal plasma corresponding to second and fourth equations of Eqs.(3.3) in the text, as

$$\frac{D}{Dt}\int^{\Gamma_K} \rho v_x d\tau = -\int^{\Gamma_K} [\rho v_x \vec{v}_E + P \overleftrightarrow{e}_x - B_x \vec{B}] \cdot \vec{ds} + \int^{\Gamma_K} x[\rho \hat{v}_\phi^2 - \hat{B}_\phi^2]\, d\tau \quad , \tag{A.8}$$

$$\frac{D}{Dt}\int^{\Gamma_K} \rho x^2 \hat{v}_\phi d\tau = -\int^{\Gamma_K} [\rho x^2 \hat{v}_\phi \vec{v}_E - x^2 \hat{B}_\phi \vec{B}\ ] \cdot \vec{ds} \quad , \tag{A.9}$$

$$\frac{D}{Dt}\int^{\Gamma_K} \rho v_y d\tau = -\int^{\Gamma_K} [\rho v_y \vec{v}_E + P^{*}\vec{e}_y - B_y \vec{B}] \cdot \vec{ds} \quad , \tag{A.10}$$

$$\frac{D}{Dt}\int^{\Gamma_K} B_x d\tau = -\int^{\Gamma_K} [B_x \vec{v}_E - v_x \vec{B}] \cdot \vec{ds} \quad , \tag{A.11}$$

$$\frac{D}{Dt}\int^{\Gamma_K} \hat{B}_\phi d\tau = -\int^{\Gamma_K} [\hat{B}_\phi \vec{v}_E - \hat{v}_\phi \vec{B}] \cdot \vec{ds} \quad , \tag{A.12}$$

$$\frac{D}{Dt}\int^{\Gamma_K} B_y d\tau = -\int^{\Gamma_K} [B_y \vec{v}_E - v_y \vec{B}] \cdot \vec{ds} \quad . \tag{A.13}$$

It should be noted the second term in r.h.s. of Eq.(A.8) is only the additional term appearing in the equations for the toroidal plasma.

List of Publications

(1) Y. Fukutani, G. Kurita and H. Oshiyama, "Stabilization of m=1 Helical Instability by Means of Feedback Field", J. Phys. Soc. Japan 37, (1974) 1103.

(2) G. Kurita and T. Amano, "Two-Dimensional Simulation of the MHD Stability (I)", JAERI-M 6437 (1976).

(3) T. Tsunematsu, G. Kurita, H. Ninomiya and T. Takeda, "Application of Reduce-2 to the Computation in CTR", JAERI-M 7176 (1977) (in Japanese).

(4) G. Kurita and T. Amano, "Two-Dimensional Simulation of the MHD Stability (II)", JAERI-M 7310 (1977).

(5) T. Tsunematsu, T. Takeda, T. Matsuura, M. Azumi, G. Kurita and T. Takizuka, "Stability Analysis by ERATO Code", JAERI-M 8616 (1979).

(6) T. Takeda, G. Kurita, T. Matsuura, H. Ninomiya, T. Tsunematsu, R. Shimada, K. Shinya and Y. Shimomura, "IAEA INTOR Workshop Report, Group II-Stability Control-", JAERI-M 8624 (1980).

(7) M. Azumi, G. Kurita, T. Matsuura, T. Takeda, Y. Tanaka and T. Tsunematsu, "A Fluid Model Numerical Code System for Tokamak Fusion Research", in Computing Method in Applied Science and Engineering, (Proc. 4th Int. Symp. Versailles, 1979), North-Holland (1980) P.335.

(8) T. Tsunematsu, T. Takeda, T. Matsuura, G. Kurita and M. Azumi, "Convergence of Solutions of the MHD Stability Code ERATO", Comput. Phys. Commun. 19, (1980) 179.

(9) M. Azumi, T. Tsunematsu, K. Itoh, T. Tuda, G. Kurita, T. Takeda, T. Takizuka, S. Tokuda, T. Matsuura, Y. Tanaka, S. Inoue and M. Tanaka, "Evolution of Stable High-Beta Tokamak Equilibria", in Plasma Physics and Controlled Nuclear Fusion Research, (Proc. 8th Int. Conf. Brussels, 1980), CN-38/k-1-1.

(10) T. Takizuka, T. Tsunematsu, S. Tokuda, M. Azumi, G. Kurita, T. Tuda, K. Itoh, Y. Tanaka, T. Matsuura and T. Takeda, "Computational Studies of Tokamak Plasmas", JAERI-M 9354 (1981).

(11) T. Takeda, K. Itoh, M. Azumi, G. Kurita, T. Takizuka, S. Tokuda, T. Tsunematsu, T. Tuda, S-I. Itoh, T. Matsuura and Y. Tanaka, "Stability Analysis of INTOR (IAEA INTOR Workshop Report Phase I, Physics (I))", JAERI-M 9466 (1981).

(12) T. Tuda, M. Azumi, G. Kurita, T. Takizuka and T. Takeda, "Ballooning Stable High Beta Tokamak Equilibria", JAERI-M 9472 (1981).

(13) M. Azumi, S. Tokuda, G. Kurita, T. Tsunematsu, T. Takizuka, T. Tuda, K. Itoh, Y. Tanaka and T. Takeda, "Internal Disruption in High β_p Tokamak", JAERI-M 9787 (1981).

(14) G. Kurita, M. Azumi, T. Tuda, T. Takizuka, T. Tsunematsu, S. Tokuda, K. Itoh and T. Takeda, "Major Disruption Process in Tokamak", JAERI-M 9788 (1981).

(15) T. Tuda, M. Azumi and G. Kurita, "Does Ballooning Mode Limit the Tokamak β?", in Annual Controlled Fusion Theory Conference, 1981 1c6.

(16) T. Tsunematsu, T. Takeda, G. Kurita, M. Azumi, T. Matsuura, R. Gruber and F. Troyon, "Beta-Limit of a Large Tokamak with a Circular Cross-Section", JAERI-M 9890 (1981).

(17) S. Yamamoto, M. Maeno, N. Suzuki, M. Azumi, S. Tokuda, M. Katagiri, S. Sengoku, T. Yamauchi, K. Kumagai, H. Takeuchi, T. Sugie, T. Kawakami, K. Ohasa, T. Matsuda, H. Kimura, H. Matsumoto, K. Odajima, K. Hoshino, T. Yamamoto, S. Konoshima, G. Kurita, T. Amano, M. Okamoto, K. Shimizu and Y. Shimomura, "Magnetohydrodynamic Activity in JFT-2 Tokamak with High-Power Neutral-Beam Injection Heating", Nucl. Fusion 8, (1981) 993.

(18) G. Kurita, M. Azumi, T. Tsunematsu and T. Takeda, "Numerical Studies of Toroidal Effect on Low-m Resistive Modes", in preparation.